

# Ly $\alpha$ escape during cosmological hydrogen recombination: the 3d-1s and 3s-1s two-photon processes

J. Chluba<sup>1,2</sup> and R. A. Sunyaev<sup>1,3</sup>

<sup>1</sup> Max-Planck-Institut für Astrophysik, Karl-Schwarzschild-Str. 1, 85741 Garching bei München, Germany

<sup>2</sup> Canadian Institute for Theoretical Astrophysics, 60 St. George Street, Toronto, ON M5S 3H8, Canada  
e-mail: jchluba@cita.utoronto.ca

<sup>3</sup> Space Research Institute, Russian Academy of Sciences, Profsoyuznaya 84/32, 117997 Moscow, Russia

Received 2 April 2009 / Accepted 27 August 2009

## ABSTRACT

We give a formulation of the radiative transfer equation for Lyman  $\alpha$  photons, which allows us to include the two-photon corrections for the 3s-1s and 3d-1s decay channels during cosmological hydrogen recombination. We use this equation to compute the corrections to the Sobolev escape probability for Lyman  $\alpha$  photons during hydrogen recombination, which then allow us to calculate the changes in the free electron fraction and CMB temperature and polarization power spectra. We show that the effective escape probability changes by  $\Delta P/P \sim +11\%$  at  $z \sim 1400$  in comparison with the one obtained using the Sobolev approximation. This accelerates hydrogen recombination by  $\Delta N_e/N_e \sim -1.6\%$  at  $z \sim 1190$ , implying that  $|\Delta C_l/C_l| \sim 1-3\%$  at  $l \gtrsim 1500$  with shifts in the positions of the maxima and minima in the CMB power spectra. These corrections will be important to the analysis of future CMB data. The total correction is the result of the superposition of three independent processes, related to (i) *time-dependent* aspects of the problem; (ii) corrections due to quantum mechanical deviations in the *shape* of the emission and absorption profiles in the vicinity of the Lyman  $\alpha$  line, from the normal Lorentzian; and (iii) a *thermodynamic* correction factor, which is found to be very important. All of these corrections are neglected in the Sobolev-approximation, but they are important in the context of future CMB observations. All three can be naturally obtained in the two-photon formulation of the Lyman  $\alpha$  absorption process. However, the corrections (i) and (iii) can also be deduced in the normal “1 + 1” photon language, without necessarily going to the two-photon picture. Therefore, only (ii) is really related to the quantum mechanical aspects of the two-photon process. We show here that (i) and (iii) represent the largest individual contributions to the result, although they partially cancel each other close to  $z \sim 1100$ . At  $z \sim 1100$ , the modification due to the shape of the line profile contributes about  $\Delta N_e/N_e \sim -0.4\%$ , while the sum of the other two contributions gives  $\Delta N_e/N_e \sim -0.9\%$ .

**Key words.** cosmic microwave background – cosmological parameters – atomic processes – cosmology: theory

## 1. Introduction

After the seminal works of Zeldovich et al. (1968) and Peebles (1968) on cosmological recombination, and the later improvements to the theoretical modeling of this epoch (e.g., Jones & Wyse 1985; Seager et al. 2000), leading to the widely used standard recombination code RECFAST (Seager et al. 1999), over the past few years the detailed physics of cosmological recombination has again been reconsidered by several independent groups (e.g., Dubrovich & Grachev 2005; Chluba & Sunyaev 2006b; Kholupenko & Ivanchik 2006; Rubiño-Martín et al. 2006; Switzer & Hirata 2008; Wong & Scott 2007). It is clear that understanding the cosmological ionization history at the level of  $\sim 0.1\%$  (e.g., see Sunyaev & Chluba 2008; Fendt et al. 2009, for a more detailed overview of the different previously neglected physical processes that are important at this level of accuracy) will be very important to accurate theoretical predictions of the cosmic microwave background (CMB) temperature and polarization angular fluctuations (e.g., see Hu et al. 1995; Seljak et al. 2003) to be measured by the PLANCK Surveyor<sup>1</sup>, which will be launched later this year.

Also for a precise calibration of the *acoustic horizon* at recombination and the possibility of constraining dark energy using baryonic acoustic oscillation (e.g., Eisenstein 2005), it is crucial to understand the physics of cosmological recombination at a high level of accuracy. Ignoring percent-level corrections to the ionization history at last scattering ( $z \sim 1100$ ) may therefore also result in significant biases to the cosmological parameters deduced using large catalogs of galaxies (e.g., Eisenstein et al. 2005; Hütsi 2006), as for example demonstrated for more speculative additions to the cosmological recombination scenario (de Bernardis et al. 2009) related to the possibility of *delayed recombination* (Peebles et al. 2000).

Among all the additional physical mechanisms during cosmological recombination that have been addressed so far, the problems connected with the *radiative transfer* of H I Lyman  $\alpha$  photons, including *partial frequency redistribution* and *atomic recoil* caused by multiple resonance scattering, *electron scattering*, and corrections due to *two-photon processes* during H I recombination ( $z \sim 800-1600$ ), have still not been solved in full depth. Here we focus on the inclusion of two-photon corrections to the 3s-1s and 3d-1s emission and absorption process.

The potential importance of two-photon transitions from highly excited levels in hydrogen and helium was first pointed

<sup>1</sup> www.rssd.esa.int/Planck

out by [Dubrovich & Grachev \(2005\)](#). They predicted a  $\sim 5\%$  decrease in the free electron fraction at  $z \sim 1200$ . However, in their computations of the effective two-photon decay rates for the  $ns$  and  $nd$ -levels, they only included the first non-resonant term (i.e. due to the dipole matrix element connecting  $ns/nd \rightarrow np$ ) into the infinite sum over intermediate states. They also neglected any possible transfer or reabsorption of photons in the vicinity of the Lyman  $\alpha$  resonance, but simply assumed that *all* the photons accounted for by the inferred effective two-photon decay rate can directly escape.

Using rate coefficients for the vacuum two-photon decays of the  $3s$  and  $3d$ -levels in hydrogen, as computed by [Cresser et al. \(1986\)](#), [Wong & Scott \(2007\)](#) concluded that [Dubrovich & Grachev \(2005\)](#) overestimated the impact of two-photon transitions on the ionization history by about one order of magnitude. However, the calculation of [Cresser et al. \(1986\)](#) was incomplete, since in their attempt to separate the “ $1 + 1$ ” photon contributions to the two-photon formula<sup>2</sup> from the “pure” two-photon decay terms, without clear justification they neglected the first non-resonant term ([Chluba & Sunyaev 2008](#)). Physically, it seems very difficult to *separate* the “pure” two-photon decay rate from the “ $1 + 1$ ” resonant contributions (see discussions in [Chluba & Sunyaev 2008](#); [Hirata 2008](#); [Karshenboim & Ivanov 2008](#); [Labzowsky et al. 2009](#); [Jentschura 2009](#)), e.g., because of non-classical interference effects. In a complete analysis, these contributions should be taken into account. In addition, [Wong & Scott \(2007\)](#) also neglected radiative transfer aspects of the problem.

Slightly later, this problem was reinvestigated in more detail ([Chluba & Sunyaev 2008](#)), showing that due to two-photon decays during hydrogen recombination, a decrease of more than  $\sim 0.3\text{--}0.5\%$  in the free electron fraction at  $z \sim 1150$  can still be expected. This estimate was obtained by taking into account departures of the full  $ns$ - $1s$  and  $nd$ - $1s$  two-photon line profiles from the Lorentzian shape in the very distant, *optically thin* part of the red wing of the Lyman  $\alpha$  line. In these regions, it can be assumed that *all* released photons can directly escape, and hence lead to a successful settling of the electron in the ground state. No radiative transfer formulation is needed to estimate this fraction of transitions, although as mentioned in their work the corrections coming from regions with significant radiative transfer can still be important. According to their computations, the two-photon decays from  $s$ -states seem to decelerate hydrogen recombination, while those from  $d$ -states speed it up. In addition, it was shown that the slight net acceleration of hydrogen recombination seems to be dominated by the  $3s$  and  $3d$  contribution ([Chluba & Sunyaev 2008](#)).

Another investigation of the two-photon aspects of the recombination problem was performed by [Hirata \(2008\)](#). He gave a formulation of the photon transfer problem simultaneously including *all* two-photon corrections during hydrogen recombination related to  $ns$ - $1s$ ,  $nd$ - $1s$ , and  $c$ - $1s$  transitions and *Raman scattering* processes, also taking into account stimulated processes in the ambient CMB blackbody radiation field. To solve this complicated problem, two approaches were used. In the first, the two-photon continuum was discretized and turned into an effective multilevel-atom with virtual states related to the energy of the photons. In the second approach, the corrections were analytically modeled as effective modifications of the Lyman  $\alpha$  and Lyman  $\beta$  decay rates. In addition, in both approaches a *distinction* between regions with “ $1 + 1$ ” photon contributions and those with pure two-photon contributions was introduced to avoid the

*double-counting* problem (see Sect. III.C of [Hirata 2008](#)) for the decay rates. As pointed out, this distinction is not unique, but the results were shown to be independent of the chosen parameters ([Hirata 2008](#)), in total yielding  $\Delta N_e/N_e \sim +1.3\%$  at  $z \sim 900$  and  $\Delta N_e/N_e \sim -1.3\%$  at  $z \sim 1300$ .

Given the delicate complexity of the two-photon transfer problem, it is very important to *independently* cross-validate the results obtained by different groups. In this paper, we offer another approach to this problem in which we take into account the two-photon nature of the  $3s$ - $1s$  and  $3d$ - $1s$  decay channels, without introducing any criterion distinguishing between “pure” two-photon decays and “ $1 + 1$ ” resonant contributions. We provide a formulation of modified rate equations for the different hydrogen levels and the photon transfer equation, which we then use to compute the effective HI Lyman  $\alpha$  photon escape probability including these corrections.

Although it is clear that in particular the atomic recoil effect accelerates hydrogen recombination at the percent-level ([Grachev & Dubrovich 2008](#); [Chluba & Sunyaev 2009c](#)) and that also partial frequency redistribution will lead to some additional modifications<sup>3</sup>, here, as in [Hirata \(2008\)](#), we neglect the frequency redistribution of photons caused by resonance scattering and work in the *no line-scattering* approximation. As explained in several previous studies ([Chluba & Sunyaev 2009c](#); [Switzer & Hirata 2008](#); [Rubiño-Martín et al. 2008](#); [Hirata 2008](#)) for the conditions in our Universe (practically no collisions), this is a much better description than the assumption of *complete redistribution*, which is used in deriving of the Sobolev escape probability. We also take into account stimulated  $3s$ - $1s$  and  $3d$ - $1s$  two-photon emission, finding this process to be subdominant. However, until now we have not included the effects connected with Raman scattering in this paper.

Instead of solving the obtained coupled system of equations simultaneously, we assume that the corrections will be small, so that each of them can be considered as a *perturbation* of the normal “ $1 + 1$ ” photon result. Therefore, we can use precomputed solutions<sup>4</sup> for the populations of the different hydrogen levels as a function of time to obtain the time-dependent photon emission rate for the different decay channels. This approach allows us to solve the HI Lyman  $\alpha$  radiative transfer equation *semi-analytically*, also including the  $3s$ - $1s$  and  $3d$ - $1s$  two-photon corrections. Using the obtained solution for the spectral distortion at different redshifts, one can then compute the *effective Lyman  $\alpha$  escape probability* as a function of time. This value can be directly compared to the normal Sobolev escape probability, which then also allows us to deduce the expected modification in the cosmological ionization history and CMB temperature and polarization power spectra.

Here we show that the effective escape probability changes by  $\Delta P/P \sim +11\%$  at  $z \sim 1400$  in comparison with the value derived in the Sobolev approximation (see Fig. 17). As we explain in detail, this total correction is the result of the superposition of three independent processes, related to (i) *time-dependent* aspects of the problem; (ii) corrections due to deviations in the

<sup>3</sup> As already mentioned in [Chluba & Sunyaev \(2009c\)](#), our current version of the code already contains the corrections due to line diffusion on thermal atoms, atomic recoil, and electron scattering. In good agreement with [Grachev & Dubrovich \(2008\)](#), we found that atomic recoil is most important, but partial frequency redistribution only leads to an additional small modification. In [Chluba & Sunyaev \(2009a\)](#), we present the results of these computations, also taking the  $3d$ - $1s$  and  $3s$ - $1d$  two-photon corrections into account.

<sup>4</sup> We used the output of the latest version of our multilevel code ([Rubiño-Martín et al. 2006](#); [Chluba et al. 2007](#)).

<sup>2</sup> This expression was first derived by [Göppert-Mayer \(1931\)](#).

shape of the emission and absorption profiles in the vicinity of the Lyman  $\alpha$  line from the normal Lorentzian; and (iii) a *thermodynamic correction factor*. All of these corrections are neglected in the cosmological recombination problem, but when analyzing future CMB data they should be taken into account.

In the “1 + 1” photon picture, the *purely time-dependent* correction was already discussed earlier (Chluba & Sunyaev 2009c), showing that changes in the state of the medium (e.g., number densities and Hubble expansion rate) cannot be neglected in the computation of the Lyman  $\alpha$  escape probability. This is because only a very small fraction ( $\sim 10^{-4}$ – $10^{-3}$ ) of all interactions with the Lyman  $\alpha$  resonance lead to a *complete redistribution* of photons over the entire line profile. As a consequence, only the region inside the Doppler core reaches full equilibrium with the photon occupation number at the line center and can be considered using *quasi-stationary* conditions. However, outside the Doppler core time-dependent aspects of the problem have to be taken into account (Chluba & Sunyaev 2009c).

The second correction is related to *quantum mechanical* modifications to the shape of the line profiles describing the  $ns$ - $1s$  and  $nd$ - $1s$  two-photon decay channels. As we explain here, this is the only correction that can only be obtained when using the two-photon picture. As already discussed earlier (e.g., Chluba & Sunyaev 2008), this leads to deviations of the corresponding profiles from the normal Lorentzian. One consequence of this is that, depending on the considered process, *more* (for  $nd$ - $1s$  transitions) or *fewer* (for  $ns$ - $1s$  transitions) photons will directly reach the very distant red wing ( $x_D \lesssim -1000$  Doppler width), where they can immediately escape. This correction was already estimated earlier (Chluba & Sunyaev 2008), but here it will now be possible to refine these computations, also extending to regions closer to the line center, where radiative transfer effects are important. Similarly, modifications to the blue wing emission can be taken into account using the approach presented here. Most importantly, because of the correct inclusion of energy conservation, the two-photon profiles will not extend to arbitrarily high frequencies. This will avoid the low redshift *self-feedback* that was seen in a time-dependent formulation of the Lyman  $\alpha$  escape problem (Chluba & Sunyaev 2009c), and can here be modeled more consistently.

The last and also most important correction discussed in this paper is related to a *frequency-dependent asymmetry* between the line emission and absorption process, which is normally neglected in the derivation of the Sobolev escape probability. As pointed out earlier (Chluba & Sunyaev 2009c) within the normal “1 + 1” photon formulation for the line emission and absorption process especially in the damping wings of the Lyman  $\alpha$  line, a blackbody spectrum is *not exactly* conserved in full thermodynamic equilibrium. This leads to the requirement of an additional factor,  $f_\nu$ , inside the absorption coefficient, which in the “1 + 1” photon picture can be deduced using the detailed balance principle (see Appendix B). However, within the two-photon formulation this correction *naturally* appears in connection with the two-photon absorption process, where one photon is taken from close to the Lyman  $\alpha$  resonance and the other is drawn from the ambient CMB blackbody photon field at a frequency inferred from energy conservation<sup>5</sup> (see Sect. 2.1.1, and in particular Sect. 3.3.2).

<sup>5</sup> For the  $1s$ - $3d$  two-photon absorption, this will be  $\nu' = \nu_{31} - \nu$ , where  $\nu_{31}$  is the corresponding  $1s$ - $3d$  transition frequency and  $\nu$  denotes the frequency of the photon that is absorbed in the vicinity of the Lyman  $\alpha$  resonance.

We henceforth refer to  $f_\nu$  as the *thermodynamic correction factor*. It results in a *suppression* of the line absorption probability in the red, and an *enhancement* in the blue wing of the Lyman  $\alpha$  resonance. This asymmetry becomes *exponentially* strong at large distances from the resonance. In most astrophysical applications, one is not interested in the photon distribution very far away from the Lyman  $\alpha$  line center, so that this correction can usually be neglected. However, for the cosmological recombination problem, even details at distances of  $\sim 10^3$ – $10^4$  Doppler width do matter (Chluba & Sunyaev 2009c), so that this inconsistency in the formulation of the transfer problem has to be resolved. As we show here, the associated correction is very important, leading to a significant acceleration of H I recombination.

We also demonstrate that including all three modifications to the escape probability, the number density of free electrons is expected to change by  $\Delta N_e/N_e \sim -1.3\%$  (see Fig. 18) close to the maximum of the Thomson visibility function (Sunyaev & Zeldovich 1970) at  $z \sim 1100$ , which matters most in connection with the CMB power spectra. The  $3s$ - $1s$  and  $3d$ - $1s$  two-photon corrections (related to the shape of the profiles and the thermodynamic factor alone) yield  $\Delta N_e/N_e \sim -2.4\%$  at  $z \sim 1110$ . A large part ( $\sim 1.1\%$  at  $z = 1100$ ) of this correction is canceled by the contributions from the time-dependent aspect of the problem (see Fig. 18 for details). Our results seem to be rather similar to those of Hirata (2008) for the contributions from high level two-photon decays alone<sup>6</sup>.

We also compute the final changes to the CMB temperature and polarization power spectra when simultaneously including all processes under discussion here (see Fig. 19). The corrections in the E-mode power spectrum are particularly impressive, reaching a peak-to-peak amplitude of  $\sim 2$ – $3\%$  at  $l \gtrsim 1500$ , and significant shifts in the positions of the maxima in the CMB power spectra. Taking these corrections into account will be important to the future analysis of CMB data.

The paper is structured as follows: in Sect. 2, we provide the equation for the modified Lyman  $\alpha$  transfer problem. There we *infer* the equations by generalizing the normal “1 + 1” photon transfer equation to account for the mentioned processes. In the Appendix A, we give a more rigorous derivation using the two-photon formulae, also generalizing the rate equations for the different hydrogen levels. We then provide the solution to the transfer equation in Sect. 2.2 and show how it can be used to compute the effective Lyman  $\alpha$  escape probability (Sect. 2.3). We explain the main physical differences and expectations of the corrections in comparison with the “1 + 1” photon formulation in Sect. 3. We then include “step by step” the different correction terms and explain the changes to the results for the spectral distortion around the Lyman  $\alpha$  line (Sect. 4) and the effective escape probability (Sect. 5). In Sect. 6, we then give the results for the ionization history and the CMB temperature and polarization power spectra. We conclude in Sect. 7.

## 2. Two-photon corrections to the Lyman $\alpha$ emission and absorption process

We derive the line emission and absorption terms describing the evolution of the photon field in the vicinity of the Lyman  $\alpha$  resonance including the  $3s$ - $1s$  and  $3d$ - $1s$  two-photon corrections. Here we attempt to motivate the form of this equation in terms of the additional physical aspects of the problem that should be

<sup>6</sup> Note that this is only part of the total correction which was presented in Hirata (2008).

incorporated. We refer the interested reader to Appendix A in which we provide the actual derivation of this equation using a two-photon formulation. There the central ingredient is that the photon distribution around the Balmer  $\alpha$  line is given by the CMB blackbody. This makes it possible to rewrite the two-photon transfer equation as an effective equation for one photon, as presented here.

We also provide the solution of the modified transfer equation (Sect. 2.2) and explain how one can use it to compute the effective escape probability for the Lyman  $\alpha$  photons (Sect. 2.3).

### 2.1. Modified equation describing the emission and death of Lyman $\alpha$ photons

Within the semi-classical formulation of the Lyman  $\alpha$  transfer equation every relevant physical process is envisioned as a single-step process involving one photon of the photon field. This leads to the introduction of photon *death* and *scattering* probabilities that depend *only* on redshift (e.g., see Chluba & Sunyaev 2009c). In the single photon picture, the line profiles for the different Lyman  $\alpha$  emission and absorption channels are also all identical under the assumption of *complete redistribution*. For example, it will make no difference if the electron reaches the 2p-state and then goes to the 3s, 3d, or continuum. In all three cases, the absorption profile will be given by the usual Voigt profile. As explained earlier (Chluba & Sunyaev 2009c), in the normal “1 + 1” photon language the Lyman  $\alpha$  line-emission and absorption terms can be cast into the form

$$\frac{1}{c} \frac{dN_\nu}{dt} \Big|_{\text{Ly-}\alpha}^{1\gamma} = \frac{\phi_V(\nu)}{4\pi \Delta\nu_D} \times \left[ p_{\text{em}}^{1\gamma} R_{2p}^+ - p_{\text{d}}^{1\gamma} h\nu_{21} B_{12} N_{1s} N_\nu \right]. \quad (1)$$

Here  $\phi_V(\nu)$  is the usual Voigt profile (see Appendix D for definition), with normalization  $\int_0^\infty \frac{\phi(\nu)}{4\pi \Delta\nu_D} d\nu d\Omega \equiv 1$ , where  $\Delta\nu_D$  is the Doppler width of the Lyman  $\alpha$  line. Furthermore,  $p_{\text{em}}^{1\gamma}$  is the Lyman  $\alpha$  emission probability in the “1 + 1” photon picture<sup>7</sup>, as given by Eq. (A.7), and  $p_{\text{d}}^{1\gamma} = 1 - p_{\text{em}}^{1\gamma}$  the corresponding death probability. The variable  $R_{2p}^+$  describes the rate at which fresh electrons are added to the 2p-state, and is defined by Eq. (A.9b).

#### 2.1.1. Introducing the thermodynamic correction factor

As mentioned in the introduction, in the form of Eq. (1), this equation does *not exactly* conserve a blackbody spectrum in the case of full thermodynamic equilibrium. Knowing the “1 + 1” photon line emission term and using the detailed balance principle one can obtain the *thermodynamic correction factor*<sup>8</sup>

$$f_\nu(z) = \frac{v_{21}^2}{\nu^2} e^{h[\nu - \nu_{21}]/kT_\nu(z)}, \quad (2)$$

which is necessary to avoid this problem.

This factor was already introduced in Chluba & Sunyaev (2009c). Inserting it into Eq. (1), we then have

$$\frac{1}{c} \frac{dN_\nu}{dt} \Big|_{\text{Ly-}\alpha}^{1\gamma} = \frac{\phi_V(\nu)}{4\pi \Delta\nu_D} \left[ p_{\text{em}}^{1\gamma} R_{2p}^+ - p_{\text{d}}^{1\gamma} h\nu_{21} B_{12} N_{1s} f_\nu N_\nu \right]. \quad (3)$$

In the standard “1 + 1” photon formulation,  $f_\nu$  has no direct physical interpretation. It is simply a consequence of thermodynamic

<sup>7</sup> For formal consistency, we included the factors  $1 + n_{\text{pl}}(\nu_{21})$  due to stimulated emission in the ambient CMB blackbody field in the definition of  $p_{\text{em}}^{1\gamma}$ , although during recombination  $n_{\text{pl}}(\nu_{21}) \ll 1$ .

<sup>8</sup> We added a short derivation for  $f_\nu$  in Appendix B.

requirements on the form of the equations. However, as shown in Appendix A, the same factor  $f_\nu$  naturally appears in a two-photon formulation of the problem. It is related to the shape of the photon distribution in the vicinity of the second photon that is involved in the Lyman  $\alpha$  absorption process (Sect. 3.3.2). This is because the photon that enables the 2p-electron to reach the 3s, 3d, or continuum is drawn from the ambient radiation field, which in the cosmological recombination problem is given by the CMB blackbody.

#### 2.1.2. Including the corrections due to the profiles of the different decay channels

As a next step, we take the differences between the line profiles of the different absorption and emission channels into account. In Eq. (3), one can see that there is *no distinction* between the different routes the electron took before or after entering the  $1s \leftrightarrow 2p$  transition. However, as mentioned in the introduction, the line-emission profiles depend on how the fresh electron reached the 2p-state via channels other than the Lyman  $\alpha$  transition.

To distinguish between the different possibilities (e.g.,  $1s \leftrightarrow 2p \leftrightarrow 3s/3d/c$ ), one should allow for profiles,  $\phi_i(\nu)$ , that depend on the channel  $i$ . The partial rate at which electrons enter the 2p-state will also depend on  $i$ , leading to the replacement  $R_{2p}^+ \rightarrow R_{2p}^{i,+}$  with  $R_{2p}^+ = \sum_i R_{2p}^{i,+}$ , where the sum runs over all possible “1 + 1” photon channels by means of which the number of Lyman  $\alpha$  photons can be affected. Furthermore, the probability of electrons being absorbed will become channel-dependent, so that  $p_{\text{d}}^{1\gamma} \rightarrow p_{\text{d}}^i$  with  $p_{\text{d}}^{1\gamma} = \sum_i p_{\text{d}}^i$ .

Here it is important that  $R_{2p}^{i,+}$  and  $p_{\text{d}}^i$  both depend only on time but not on frequency. This is because microscopically it is assumed that the absorption process leads to a complete redistribution over the profile  $\phi_i(\nu)$ . Then it is also clear that the factor  $f_\nu$  should be independent of the channel, since otherwise detailed balance for each process cannot be achieved.

With this in mind, it is clear that the more general form of Eq. (3) should read

$$\frac{1}{c} \frac{dN_\nu}{dt} \Big|_{\text{Ly}} = \sum_i \frac{\phi_i(\nu)}{4\pi \Delta\nu_D} \left[ p_{\text{em}}^{1\gamma} R_{2p}^{i,+} - p_{\text{d}}^i h\nu_{21} B_{12} N_{1s} f_\nu N_\nu \right]. \quad (4)$$

In Appendix A, we argue that both  $R_{2p}^{i,+}$  and  $p_{\text{d}}^i$  can be given using the normal “1 + 1” photon values for the different rates. We also specify how to compute the profiles,  $\phi_i(\nu)$ , including stimulated two-photon emission (Sect. C). However, in what follows it is only important that none of these processes depends on the solution of the problem for the photon field. This is because we assume that the readjustments to the populations of the different level or number density of free electrons is small and hence can be neglected to lowest order. Numerically, one can include the correction to the correction iteratively, but we leave this to a future paper.

We note that because in two-photon transitions  $ns/d \rightarrow 1s$  from  $n > 3$  also photons connected with the other Lyman series are emitted, Eq. (4) can in principle be used to describe the simultaneous evolution of all Lyman series photons. Similarly, one can account for the two-photon corrections due to transitions from the continuum  $c \rightarrow 1s$ , by simultaneously including the Lyman continuum and all other continua. However, in this case one can no longer clearly distinguish between the different Lyman series. The equation will also simultaneously describe the process of Ly- $n$  feedback (Chluba & Sunyaev 2007), and in addition account for its exact time-dependence. To avoid these

complications, below we first take into account only the two-photon corrections for the 3s-1s and 3d-1s channel, but leave the others unchanged. In this case, it is possible to directly compare the results with those of the normal Lyman  $\alpha$  problem. In Sect. 7, we briefly discuss the expected effect of this approximation, but leave a detailed analysis to another paper.

## 2.2. Solution of the transfer equation

For a given ionization history, the solution of Eq. (4) in the expanding Universe can be readily found, using the procedure described in Chluba & Sunyaev (2009c). If we introduce the effective absorption optical depth as

$$\tau_{\text{abs}}(\nu, z', z) = \int_z^{z'} p_d^{1\gamma} \frac{c \sigma_r N_{1s}}{H(1+z)} \phi_{\text{abs}}(x[1+\tilde{z}], \tilde{z}) d\tilde{z} \quad (5a)$$

$$\phi_{\text{abs}}(\nu, z) = f_\nu(z) \sum_i \frac{p_d^i}{p_d^{1\gamma}} \phi_i(\nu, z) = f_\nu(z) \phi_{\text{abs}}^*(\nu, z) \quad (5b)$$

with  $p_d^{1\gamma} = 1 - p_{\text{em}}^{1\gamma}$ ,  $\sigma_r = \frac{h\nu_{21}}{4\pi} \frac{B_{12}}{\Delta\nu_D}$  and the dimensionless frequency  $x = \nu/(1+z)$ , and define the effective emission profile

$$\phi_{\text{em}}(\nu, z) = \sum_i \frac{R_{2p}^{i,+}}{R_{2p}^+} \phi_i(\nu, z), \quad (6)$$

then Eq. (4) takes the simple form

$$\frac{1}{c} \frac{dN_\nu}{dt} \Big|_{\text{Ly}} = p_d^{1\gamma} \sigma_r N_{1s} \phi_{\text{abs}}(\nu, z) \{N_\nu^{\text{em}} - N_\nu\} \quad (7a)$$

$$N_\nu^{\text{em}} = \frac{2\nu_{21}^2 g_{1s}}{c^2 g_{2p}} \frac{R_{2p}^+}{R_{2p}^- N_{1s}} \times \frac{\phi_{\text{em}}(\nu, z)}{\phi_{\text{abs}}(\nu, z)} \equiv N_{\text{em}} \frac{\phi_{\text{em}}(\nu, z)}{\phi_{\text{abs}}(\nu, z)}, \quad (7b)$$

where  $N_{\text{em}}$  is only redshift-dependent.

The solution of this equation in the expanding Universe can be directly given (see Chluba & Sunyaev 2009c)

$$\Delta N_\nu^{\text{asym}}(z) = [N_{\text{em}}(z) - N_{\nu_{21}}^{\text{pl}}] \times F(\nu, z). \quad (8a)$$

Here the function  $F_\nu$  represents the frequency-dependent part of the solution for the spectral distortion, which is defined by

$$F(\nu, z) = \int_{z_s}^z \Theta^a(z, z') \partial_{z'} e^{-\tau_{\text{abs}}(\nu, z', z)} dz' \quad (8b)$$

$$\Theta^a(z, z') = \frac{\tilde{N}_{\text{em}}(z') \times \frac{\phi_{\text{em}}(\nu', z')}{\phi_{\text{abs}}(\nu', z')} - \tilde{N}_x^{\text{pl}}}{\tilde{N}_{\text{em}}(z) - \tilde{N}_{x_{21}}^{\text{pl}}} \quad (8c)$$

$$\equiv \frac{1}{f_{\nu'}} \frac{\tilde{N}_{\text{em}}(z') \times \frac{\phi_{\text{em}}(\nu', z')}{\phi_{\text{abs}}(\nu', z')} - \tilde{N}_{x_{21}}^{\text{pl}}}{\tilde{N}_{\text{em}}(z) - \tilde{N}_{x_{21}}^{\text{pl}}}, \quad (8d)$$

where  $\Delta N_\nu = N_\nu - N_\nu^{\text{pl}}$ ,  $\nu' = x[1+z']$ , and at  $z > z_s$  the CMB spectrum is assumed to be given by a pure blackbody spectrum  $N_\nu^{\text{pl}}$ . Furthermore,  $\tilde{N}_{\text{em}}(z) = N_{\text{em}}(z)/[1+z]^2$ ,  $x_{21} = \nu_{21}/[1+z]$ ,  $x'_{21} = \nu_{21}/[1+z']$ , and  $\tilde{N}_x^{\text{pl}} = \frac{2}{c^2} \frac{x^2}{e^{hx/kT_0} - 1}$ , with  $T_0 = 2.725$  K. We note that  $\tilde{N}_x^{\text{pl}}$  does not explicitly depend on redshift. We also assumed that  $f_{\nu'}(z') \tilde{N}_x^{\text{pl}} \equiv \tilde{N}_{x_{21}}^{\text{pl}}$ .

## 2.3. Number of absorbed photons and the effective Lyman $\alpha$ escape probability

With the solution given in Eq. (8), one can directly compute the number of absorbed photons. For this, we define the mean of  $N_\nu = I_\nu/h\nu$  over the absorption profile

$$\begin{aligned} \bar{N}_{\text{abs}}(z) &= \int \frac{\phi_{\text{abs}}(\nu, z)}{4\pi \Delta\nu_D} N_\nu d\nu d\Omega = \int \frac{\phi_{\text{abs}}^*(\nu, z)}{4\pi \Delta\nu_D} f_\nu N_\nu d\nu d\Omega \\ &= N_{\nu_{21}}^{\text{pl}} \bar{\varphi}_{\text{abs}}^* + \int \varphi_{\text{abs}}^*(\nu, z) f_\nu(z) \Delta N_\nu d\nu, \end{aligned} \quad (9)$$

where we have set  $\varphi_{\text{abs}}^*(\nu, z) = \phi_{\text{abs}}^*(\nu, z)/\Delta\nu_D$  and defined the normalization of  $\varphi_{\text{abs}}^*$  as  $\bar{\varphi}_{\text{abs}}^* = \int \varphi_{\text{abs}}^*(\nu, z) d\nu$ . If we now insert Eq. (8) into this expression, we can write

$$\Delta \bar{N}_{\text{abs}}^{\text{asym}}(z) = [N_{\text{em}}(z) - N_{\nu_{21}}^{\text{pl}}] [1 - P] \quad (10a)$$

$$P = 1 - \int \varphi_{\text{abs}}^*(\nu) f_\nu(z) F_\nu d\nu. \quad (10b)$$

Here  $P$  will later be interpreted as the main part of the effective escape probability (see Sects. 2.3.2 and 5).

As for  $\bar{N}_{\text{abs}}(z)$ , one can also define

$$\begin{aligned} \bar{N}_{\text{em}}(z) &= \int \frac{\phi_{\text{em}}(\nu, z)}{4\pi \Delta\nu_D} N_\nu^{\text{em}} d\nu d\Omega \stackrel{!}{=} \int \frac{\phi_{\text{em}}(\nu, z)}{4\pi \Delta\nu_D} N_{\text{em}}(z) d\nu d\Omega \\ &= N_{\text{em}} \bar{\varphi}_{\text{em}}, \end{aligned} \quad (11)$$

so that with the transfer equation given in Eq. (7), it follows that

$$\begin{aligned} \frac{dN_\nu}{dt} \Big|_{\text{Ly}} &= \frac{1}{c} \int \frac{dN_\nu}{dt} \Big|_{\text{Ly}} d\nu d\Omega \\ &= p_d^{1\gamma} h\nu_{21} B_{12} N_{1s} \{N_{\text{em}} \bar{\varphi}_{\text{em}} - N_{\nu_{21}}^{\text{pl}} \bar{\varphi}_{\text{abs}}^* \\ &\quad - [N_{\text{em}} - N_{\nu_{21}}^{\text{pl}}] [1 - P]\} \\ &= p_d^{1\gamma} h\nu_{21} B_{12} N_{1s} \{P_{\text{eff}} [N_{\text{em}} - N_{\nu_{21}}^{\text{pl}}]\}, \end{aligned} \quad (12a)$$

where

$$P_{\text{eff}} = P + \Delta P_{\text{ind}} \quad (12b)$$

$$\Delta P_{\text{ind}} = \frac{N_{\text{em}} \Delta \bar{\varphi}_{\text{em}} - N_{\nu_{21}}^{\text{pl}} \Delta \bar{\varphi}_{\text{abs}}^*}{N_{\text{em}} - N_{\nu_{21}}^{\text{pl}}}, \quad (12c)$$

where  $\Delta \bar{\varphi}_{\text{em}} = \bar{\varphi}_{\text{em}} - 1$  and  $\Delta \bar{\varphi}_{\text{abs}}^* = \bar{\varphi}_{\text{abs}}^* - 1$ . As we explain below, with these definitions the effective escape probability,  $P_{\text{eff}}$ , can now be directly compared with the value in the normal “1 + 1” photon formulation and the Sobolev escape probability.

### 2.3.1. Range of integration over the profiles

In the above derivation, we have not specified the range of integration. Since the 3s and 3d two-photon profile include both the Balmer  $\alpha$  and Lyman  $\alpha$  photons, by carrying out the integrals over the frequency interval  $(0, \infty)$ , one would count  $2\gamma$  per transition. To avoid this problem, we can simply restrict the range of integration to  $\nu \geq \nu_{31}/2$ , but leave all the other definitions unaltered. Since  $\nu_{31}/2$  is far away from the Lyman  $\alpha$  resonance, this does not lead to any significant problem regarding the normalization of the normal Voigt function<sup>9</sup>. In addition, for the

<sup>9</sup>  $\nu_{31}/2$  corresponds to  $x_D \approx -1.7 \times 10^4 \left[ \frac{1+z}{1100} \right]^{-1/2}$  Doppler width, so that the absolute error in the normalization of  $\phi_\nu$  is  $\sim 1.6 \times 10^{-8}$ .

quasi-stationary approximation the contribution to the value of the escape probability from this region are completely negligible. Therefore, this restriction does not lead to any bias in the result, but does simplify the numerical integration significantly.

### 2.3.2. Relating the corrections to the spectral distortion, to the corrections in the effective escape probability

We now want to understand how differences in  $F_\nu$  and  $\frac{dN_\nu}{dt}$  relate to corrections in the effective escape probability. We first wish to emphasize that in the normal “1 + 1” photon picture, based on the assumption of quasi-stationarity and the no line-scattering approximation, following the derivation of the previous section one would find (Chluba & Sunyaev 2009c)

$$\left. \frac{dN_\nu^d}{dt} \right|_{L_\nu} = p_d^{1\gamma} h\nu_{21} B_{12} N_{1s} P_d [N_{em} - N_{\nu_{21}}^{p1}], \quad (13)$$

where  $P_d = \frac{1-e^{-\tau_d}}{\tau_d}$  and  $\tau_d = p_d^{1\gamma} \tau_S$ .

It is clear that  $\frac{dN_\nu^d}{dt} \Delta t$  represents the effective change in the total number density of photons involved in the Lyman  $\alpha$  evolution over a short time interval  $\Delta t$ , and hence is directly related to the change in the total number of electrons that settle into the ground state by means of the Lyman  $\alpha$  channel. By comparing  $P_d$  with  $P_{eff}$ , as defined by Eq. (12b), one can therefore deduce the required effective correction to the Sobolev escape probability that is normally used in the formulation of the recombination problem. Following the arguments of Chluba & Sunyaev (2009c), this correction should be given by

$$\Delta P_S = \frac{p_d^{1\gamma} P_{eff}}{1 - p_{em}^{1\gamma} P_{eff}} - P_S, \quad (14)$$

where  $P_S = \frac{1-e^{-\tau_S}}{\tau_S}$  is the standard Sobolev escape probability, with the usual Sobolev optical depth,  $\tau_S$ .

## 3. Main sources of corrections to the Lyman $\alpha$ spectral distortion

Using the solution given in Eq. (8) one can already identify the main sources of corrections to the photon distribution in comparison with the quasi-stationary approximation. These can be divided into those acting as a time and frequency-dependent *emissivity*, which is characterized by  $\Theta^a$ , and those just affecting the *absorption optical depth*,  $\tau_{abs}$ . Below we explain how the two-photon aspect of the problem enters here, and which effects are expected. In Sects. 4 and 5, we discuss the corrections to the Lyman  $\alpha$  spectral distortion and the effective escape probability in comparison with the standard “1 + 1” photon formulation, in more detail.

### 3.1. Relative importance of the different Lyman $\alpha$ absorption channels

Before studying at the solution of the transfer equation in more detail, it is important to understand which channels on average contribute the most to the absorption of Lyman  $\alpha$  photons. In Fig. 1, we present the partial death probabilities for different channels, as defined in Appendix A. At all considered redshifts, more than  $\sim 90\%$  of the absorbed Lyman  $\alpha$  photons disappear from the photon distribution in 1s-3d two-photon transitions. In contrast, only about 2% of all transitions end in the 3s-state.

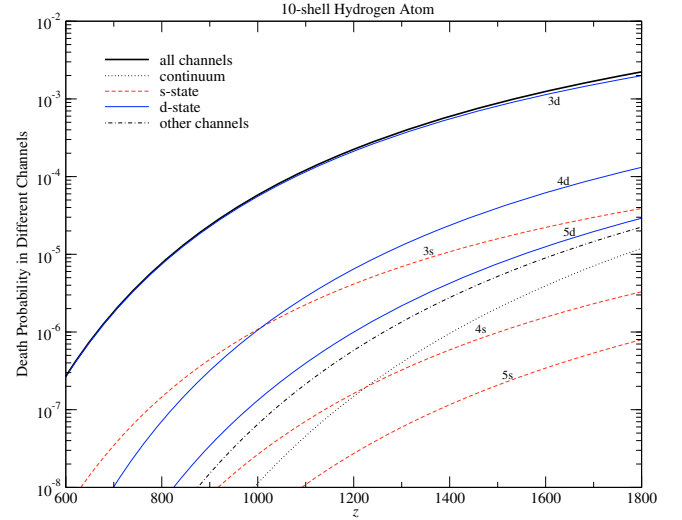


**Fig. 1.** The death probabilities for different Lyman  $\alpha$  absorption channels. We used a 10-shell hydrogen atom. The thick solid line shows the total death probability,  $p_d$  (for definition see Appendix A).

This is because the ratio of the 2p-3s to 2p-3d transition rates is about  $g_{3s}A_{3s2p}/g_{3d}A_{3s2p} \sim 1/50$ . In general, one can also see that the 1s-nd channels are more important than the 1s-n<sub>s</sub> channels, and that the contributions of 1s-3s and 1s-4d two-photon channels are comparable, whereas at high redshift the 1s-4d channels contributes slightly more ( $\sim 2\%$  versus  $\sim 7\%$ ). However, fewer than  $\sim 0.5\%$  of photons are directly absorbed by the continuum.

Assuming that the final modification to the ionization history is  $\Delta N_e/N_e \sim 1\%$ , when *only* including the two-photon aspects for the 3d-1s channel, then the above numbers suggest that: (i) the additional correction is expected to be similar to  $\Delta N_e/N_e \sim 0.1\%$ , when taking also the two-photon character of the 1s-3s, 1s-4d, and 1s-5d channels into account; (ii) neglecting the two-photon character of the transition to the continuum should lead to an uncertainty of  $\Delta N_e/N_e \lesssim 0.1\%$ . These simple conclusions seem to be in good agreement with the computations of Hirata (2008). This also justifies why here as a first step we consider only the two-photon corrections to the 3s-1s and 3d-1s channel. However, we plan to take the other two-photon corrections into account in a future paper.

### 3.2. Effective Lyman $\alpha$ emission and absorption profile

As we have seen in the previous section, the main channel for Lyman  $\alpha$  absorption is related to the 1s-3d two-photon transition. This implies that the effective absorption profile,  $\phi_{abs}^*$ , is very close to that following from the 3d-1s channel alone. In Fig. 2, we illustrate the spectral dependence of different line profiles in the vicinity of the Lyman  $\alpha$  resonance at redshift  $z = 1300$ . For comparison, we also show the Voigt profile,  $\phi_\nu$  (see Appendix D). One can clearly see the asymmetry of the two-photon profiles around the Lyman  $\alpha$  line center and the deviations from the Lorentzian shape in the distant damping wings.

In the right panel, we also show the effective emission profile,  $\phi_{em}$ , for the 3-shell atom, as defined by Eq. (6). In the computations, we included only the 3s and 3d two-photon profiles, but assumed that in the continuum channel (1s  $\leftrightarrow$  2p  $\leftrightarrow$  c) photons are emitted according to the normal Voigt profile. As one can see, the effective emission profile is indeed very close to the 3d-1s two-photon profile, including stimulated emission. Only at  $\nu \geq \nu_{31}$  can one see the small Lorentzian contribution from

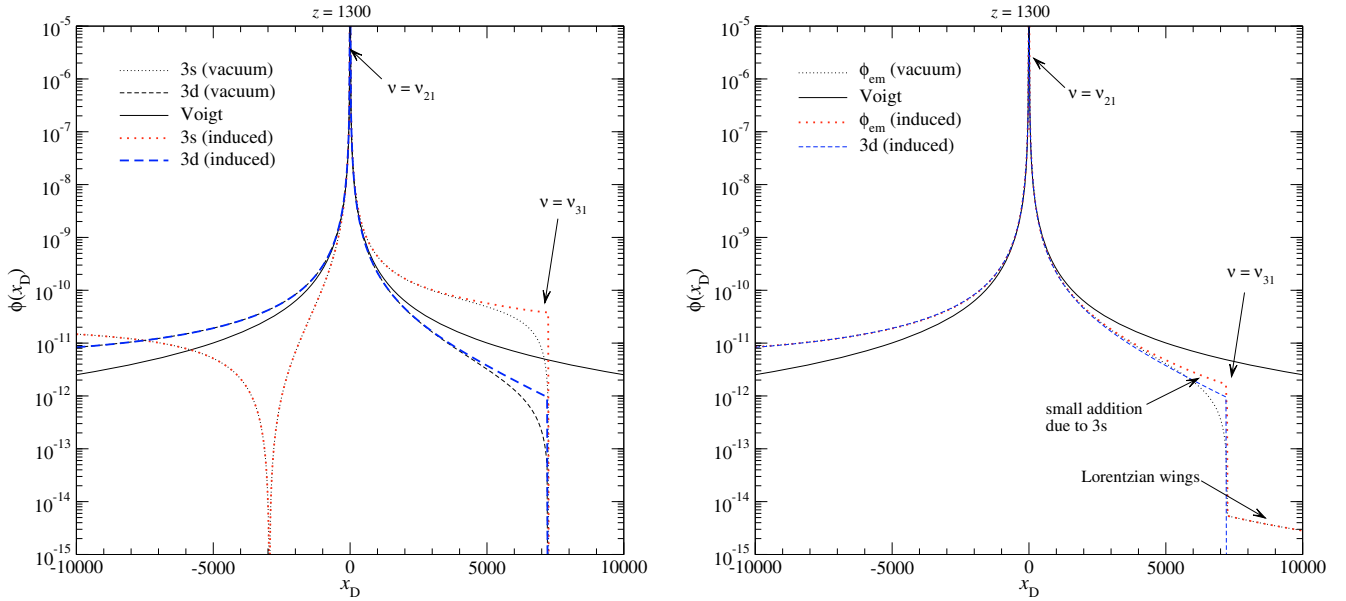


**Fig. 2.** Different line profiles in the vicinity of the Lyman  $\alpha$  resonance at redshift  $z = 1300$ . The left panel shows the 3s and 3d emission profiles in comparison with the normal Voigt profile. In the right panel, we show the effective emission profile for a 3-shell hydrogen atom, as defined by Eq. (6), in comparison with the 3d emission profile and the Voigt profile. The curves labeled “induced” include the effect of stimulated two-photon emission due to enhancement connected with the second photon released at low frequencies. This process is only important close to  $\nu \sim \nu_{31}$  and eventually leads to a subdominant correction of  $\Delta N_e/N_e \lesssim 0.1\%$  in the ionization history. On the other hand, the overall asymmetry in the effective emission profile (red wing stronger than blue wing) has important implications for the hydrogen recombination problem.

the continuum channel. Close to  $\nu_{31}$ , one can also see the small admixture of the 3s-1s two-photon profile. As can be deduced from the left panel in Fig. 2, at  $\nu \sim \nu_{31}$  the stimulated 3s-1s two-photon profile is about  $\sim 40$  times larger than the 3d-1s two-photon profile. With appropriate renormalization, one can also obtain this factor using the approximation given by Eq. (C.3). Although  $R_{2p}^{3s,+} \sim R_{2p}^{3d,+}/50$ , because of this factor at  $\nu \sim \nu_{31}$  the 3s channel adds about  $\frac{4}{5} \phi_{3d}$ , or  $\sim 44\%$  to the effective emission profile.

### 3.3. Time and frequency dependence of the absorption optical depth

In the definition of  $F(\nu, z)$ , i.e., Eq. (8b), the function  $\Theta^3$  accounts for the frequency and time dependence of the emission process. For  $\Theta^3 = 1$ , the shape of the solution for the spectral distortion depends only on the absorption optical depth,  $\tau_{\text{abs}}$ , as defined by Eq. (5a). In this case, one can write directly

$$F_0(\nu, z) = 1 - e^{-\tau_{\text{abs}}(\nu, z, z)}. \quad (15)$$

Separating this part of the solution is very useful for numerical purposes. However, as we see in Sect. 3.4.2,  $F_0$  does not describe the main behavior of the spectral distortion when including the thermodynamic correction factor  $f_\nu$ .

#### 3.3.1. Purely time-dependent correction to $\tau_{\text{abs}}$

If we neglect the two-photon corrections to the 3s and 3d profiles ( $\phi_i = \phi_\nu$ ) and define  $f_\nu \equiv 1$  then we can look at the purely time-dependent correction to  $\tau_{\text{abs}}$ . As explained earlier (Chluba & Sunyaev 2009c), the dependencies of  $p_d$ ,  $N_{1s}$ , and  $H$  on redshift lead to deviations in the solution for the spectral distortion from the quasi-stationary case. Here the most important aspects are that, depending on the emission redshift, the total absorption optical depth until the time of observation (here  $z$ ), is effectively

lower (for  $z_{\text{em}} > z \gtrsim 1400$ ), or greater (for  $z < z_{\text{em}} \lesssim 1400$ ) than in the quasi-stationary case. In addition, the deviation from the quasi-stationary case depends on the initial frequency of the considered photon, since close to the line center photons travel a much shorter distance before becoming absorbed than in the very distant wings, implying that time-dependent corrections are only important to photons that are emitted outside the Doppler core (for more details see Chluba & Sunyaev 2009c).

In Fig. 3, we illustrate these effects on  $\tau_{\text{abs}}$  for emission redshift  $z = 1100$ . We show the optical depth as a function of the initial frequency for different  $\Delta z$ . In the upper panel, we give the results for the case under discussion here (solid line). For comparison, we show the values of the optical depth using the normal quasi-stationary optical depth (dashed lines) for which one has

$$\tau_d^{\text{qs}}(\nu, z, z') \approx \tau_d(z) \int_{\nu'}^{\nu} \phi_\nu(\tilde{\nu}) \frac{d\tilde{\nu}}{\Delta\nu_D}, \quad (16)$$

where  $\tau_d(z) = p_d^{1\gamma} \tau_S$ ,  $\tau_S$  is the normal Sobolev optical depth,  $\nu' = \nu \frac{1+z'}{1+z}$ , and  $z' = z - \Delta z$ .

For very small  $\Delta z/z$ , one expects no significant difference between the full numerical result for  $\tau_{\text{abs}}$  and this approximation. However, looking at the cases  $\Delta z/z = 10^{-5}$ ,  $10^{-4}$ , and  $10^{-3}$  one can see that even then there is a small difference in the distant red and blue wings of the line. This is not because of time-dependent corrections but because, as usual, in Eq. (16) we neglected the factor  $\nu_{21}/\nu$ , which appears in the definition of  $\tau_{\text{abs}}$ , leading to  $\tau_{\text{abs}}/\tau_d^{\text{qs}} \sim \nu_{21}/\nu \gtrsim 1$  on the red, and  $\tau_{\text{abs}}/\tau_d^{\text{qs}} \lesssim 1$  on the blue side of the resonance.

For the cases  $\Delta z/z = 0.01$  and  $0.1$ , we start to see the corrections due to the time-dependence. For  $\Delta z/z = 0.1$  in both wings, we find that  $\tau_{\text{abs}} \lesssim \tau_d^{\text{qs}}$ . This is because the photons were released at  $z \lesssim 1400$ , so that  $\tau_d(z)$  decreases while the photons travel (Chluba & Sunyaev 2009c). This means that the integral over different redshifts  $\tau_d(\nu, z, z') \approx \int_{\nu'}^{\nu} \tau_d(\tilde{z}) \phi_\nu(\tilde{\nu}) \frac{d\tilde{\nu}}{\Delta\nu_D} \lesssim \tau_d(z) \int_{\nu'}^{\nu} \phi_\nu(\tilde{\nu}) \frac{d\tilde{\nu}}{\Delta\nu_D}$  cannot reach the full value for  $\tau_d^{\text{qs}}(z)$ . We note

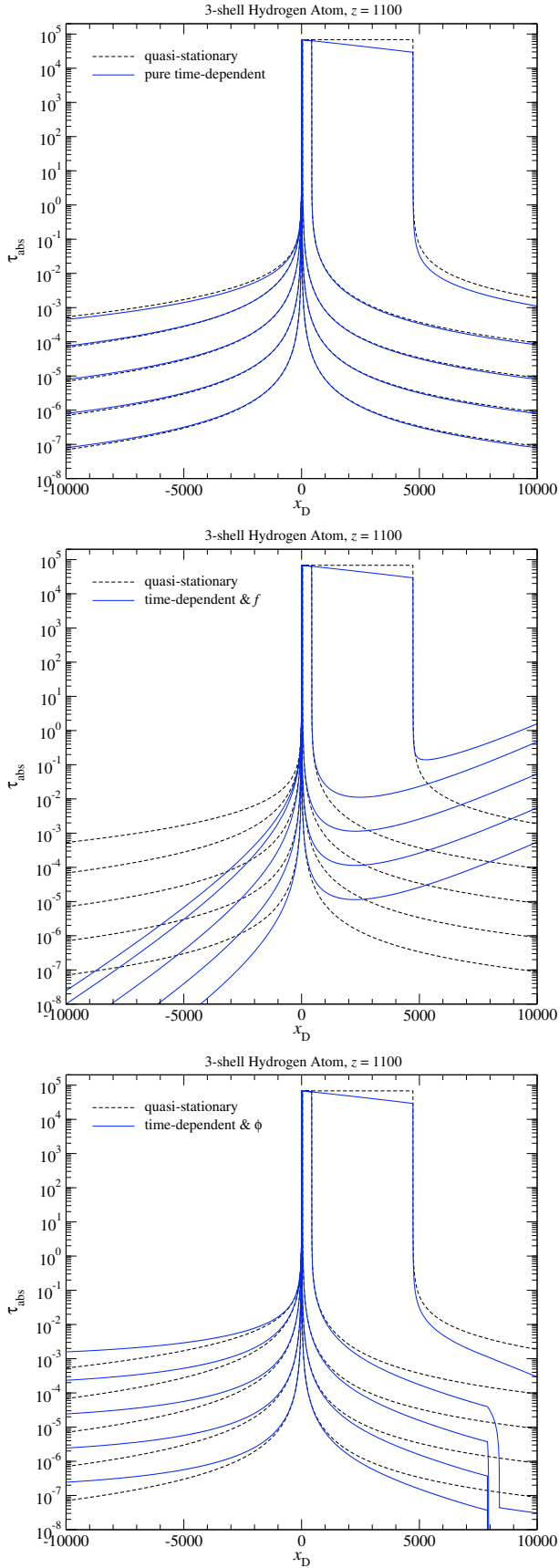


**Fig. 3.** Modifications in the absorption optical depth  $\tau_{\text{abs}}(x_{\text{D}}, z, z - \Delta z)$  for  $z = 1100$ . Here  $x_{\text{D}} = [\nu - \nu_{21}]/\Delta\nu_{\text{D}}$ , where  $\Delta\nu_{\text{D}}$  is the Doppler width of the Lyman  $\alpha$  resonance. In each plot we show a sequence (lower to upper set of curves) of  $\Delta z/z = 10^{-5}, 10^{-4}, 10^{-3}, 10^{-2}$  and 0.1. For detailed explanation see Sect. 3.

that comparing with the value  $\tau_{\text{d}}^{\text{qs}}(z') \lesssim \tau_{\text{d}}^{\text{qs}}(z)$  at the absorption redshift  $z' = z - \Delta z < z$ , one finds that  $\tau_{\text{d}}(\nu, z, z') \gtrsim \tau_{\text{d}}^{\text{qs}}(z')$  following a similar argument. Usually this is the comparison made when talking about the escape probability at redshift  $z$ , so that the role of  $z$  and  $z'$  is simply interchanged.

In the distant wings of the line profile, the difference due to the time-dependence is not very visible for  $\Delta z/z = 0.01$  (the changes should be  $|\Delta\tau/\tau| \sim |\Delta z/z|$ ). However, one can see it in the region  $0 \lesssim x_{\text{D}} \lesssim x_{\text{D}}^{\text{c}} \sim 500$ . There it is clear that the emitted photons will reach the Doppler core over a period that is shorter than the chosen  $\Delta z/z$ . For the case  $\Delta z/z = 0.1$ , this region is  $0 \lesssim x_{\text{D}} \lesssim x_{\text{D}}^{\text{c}} \sim 4800$ . Depending on how far the photon initially was emitted from the Doppler core the time that it will travel before reaching  $x_{\text{D}} \sim 0$  will grow with increasing  $x_{\text{D}}$ . This implies that at a redshift  $z_{\text{c}} < z \lesssim 1400$  of Doppler core crossing, we have  $\tau_{\text{d}}(z_{\text{c}}) \lesssim \tau_{\text{d}}(z)$ , leading to the slope seen in the regions  $0 \lesssim x_{\text{D}} \lesssim x_{\text{D}}^{\text{c}}$ .

In the final result, we note the time-dependent correction to  $\tau_{\text{abs}}$  is not so important, only leading to modifications in the escape probability by  $|\Delta P/P| \sim 1-3\%$ . The time-dependence of  $\Theta^{\text{a}}$  is far more relevant (see Sect. 5 for more details).

### 3.3.2. Effect of thermodynamic correction factor on $\tau_{\text{abs}}$

If we now include the *thermodynamic* correction factor  $f_{\nu}$ , as given by Eq. (2), in the computation of  $\tau_{\text{abs}}$ , then it is clear that for photons appearing at a given time on the *red side* of the Lyman  $\alpha$  resonance, the total absorption optical depth over a fixed redshift interval will be *lower* than in the standard approach, independent of the emission redshift. Since  $h\nu_{21}/kT_{\gamma} \sim 40 \left[ \frac{1+z}{1100} \right]^{-1}$ , one has  $h[\nu - \nu_{21}]/kT_{\gamma} \sim \frac{x_{\text{D}}}{10^3} \left[ \frac{1+z}{1100} \right]^{-1/2}$ . Because of the exponential dependence of  $f_{\nu}$  on the distance to the line center, this implies that at  $x_{\text{D}} \lesssim -10^3 \left[ \frac{1+z}{1100} \right]^{1/2}$  photons even directly escape, without any further reabsorption. This is in stark contrast to the standard approximation ( $f_{\nu} = 1$ ) for which even at distances  $\sim -10^4$ , some small fraction of photons (comparable to  $10^{-3}$  at  $z \sim 1100$ ) still disappears. We illustrate this behavior in the central panel of Fig. 3, where at large distances on the red side of the resonance, the value of  $\tau_{\text{abs}}$  is many orders of magnitude smaller than in the quasi-stationary approximation. As we see below (e.g., Sect. 5.1), the thermodynamic factor leads to the largest correction discussed in this paper, and it is this *red wing suppression of the absorption cross-section* that contributes most.

As mentioned in Sect. 2.1.1, this behavior reflects physically that the photon that enables the 2p-electron to reach the 3s and 3d is drawn from the ambient CMB radiation field. For photons on the red side of the Lyman  $\alpha$  resonance ( $\nu < \nu_{21}$ ), another photon with  $\nu' > \nu_{32}$  is necessary for a 1s electron to reach the third shell. Since during HI recombination the Balmer  $\alpha$  line is already in the Wien tail of the CMB, this means that relative to the Balmer  $\alpha$  line center the amount of photons at  $\nu' > \nu_{32}$  is *exponentially* smaller, depending on how large the detuning is. Denoting the frequency of the second photon (absorbed close to the Balmer  $\alpha$  resonance) with  $\nu' = \nu_{31} - \nu$ , by taking the ratio of the photon occupation numbers, i.e.,  $n'/n_{\text{pl}}(\nu_{32}) \approx n_{\text{pl}}(\nu_{31} - \nu)/n_{\text{pl}}(\nu_{32}) \approx e^{h[\nu - \nu_{21}]/kT_{\gamma}}$ , we again can confirm the exponential behavior of  $f_{\nu}$ . We note that the same factor appears when considering two-photon transitions towards higher levels with  $n > 3$  or the continuum. It is a result of thermodynamic requirements, which should be independent of the

considered process, as long as the second photon is drawn from the CMB blackbody.

On the other hand, for photons released on the *blue side* of the Lyman  $\alpha$  line, the total absorption optical depth is *larger* than in the standard approximation (see Fig. 3 central panel for illustration). Because of the exponential dependence of  $f_\nu$  on frequency, for  $\phi_{\text{abs}}^* = \phi_\nu$  this even leads to an *arbitrarily* large absorption optical depth in the very distant blue wing. Again this behavior can be understood by assuming that the second photon is drawn from the CMB blackbody. However, there are now exponentially more photons available than at the Balmer  $\alpha$  line center.

This very strong increase in the absorption optical depth implies that photons are basically reabsorbed *quasi-instantaneously*, so that at  $\nu \gg \nu_{21}$  the usual quasi-stationary approximation for the computation of  $\tau_{\text{abs}}$  should be possible, as inside the Doppler core. In this case, one therefore has

$$\begin{aligned} \tau_{\text{abs}}^{\text{qs}}(\nu, z_s, z) &\approx \tau_d(z) \int_\nu^{\nu_s} \phi_{\text{abs}}(\nu') \frac{\nu_{21}}{\Delta\nu_D} \frac{d\nu'}{\nu'} \\ &\approx \tau_d(z) f_\nu(z) \int_\nu^{\nu_s} \phi_{\text{abs}}^*(\nu') \frac{d\nu'}{\Delta\nu_D}, \end{aligned} \quad (17)$$

where  $\tau_d(z) = p_d^{1\gamma} \tau_S$ ,  $\tau_S$  is the normal Sobolev optical depth, and  $\nu_s = \nu \frac{1+z_s}{1+z}$ . This approximation for  $\tau_{\text{abs}}$  will also be very accurate close to the line center, but is very crude in the red wing. We note that for  $f_\nu = 1$  and  $\phi_{\text{abs}}^* = \phi_\nu$ ,  $\tau_{\text{abs}}^{\text{qs}}$  recovers the approximation for the normal absorption optical depth in the quasi-stationary approximation, Eq. (16).

For  $z_s \rightarrow \infty$ ,  $\nu \gg \nu_{21}$  and assuming that  $\phi_{\text{abs}}^* = \phi_\nu$ , one has

$$\tau_{\text{abs}}^{\text{blue}}(\nu, z_s, z) \approx \tau_d(z) f_\nu(z) \frac{a}{\pi x_D}. \quad (18)$$

With this equation, it is possible to estimate the position on the blue side of the Lyman  $\alpha$  resonance at which  $\tau_{\text{abs}} \sim 1$ . Above that point,  $F_0 \rightarrow 1$ , although this does not represent the main behavior of  $F_\nu$  for the given assumptions, since the factor  $1/f_\nu$  in  $\Theta^a$  also becomes important, so that  $F_\nu$  instead scales like  $1/f_\nu$  at large  $x_D$  (see Sect. 3.4.2).

### 3.3.3. Effect of line absorption profile on $\tau_{\text{abs}}$

It is clear that the *shape* of the absorption profile also has an effect on the frequency dependence of the absorption optical depth. As we explained in Sect. 3.2, the effective absorption profile,  $\phi_{\text{abs}}^*$  is very close to the two-photon emission profile of the 3d-level (see Fig. 2). For simplicity assuming that  $\phi_{\text{abs}}^* \equiv \phi_{3d \rightarrow 1s}$ , it is clear that at  $\nu \geq \nu_{31}$ , no photons can be absorbed in the Lyman  $\alpha$  transition, since there  $\phi_{3d \rightarrow 1s} = 0$ . This is in stark contrast to the case of a normal Voigt profile, for which in principle some photons can be absorbed at arbitrarily high frequencies. Considering photons that reach the frequency interval  $\nu_{21} \leq \nu \leq \nu_{31}$ , since in that region  $\phi_{3d \rightarrow 1s} \lesssim \phi_\nu$  (see Fig. 2), the contribution to the total absorption optical depth coming from this region is *smaller* than in the standard “1 + 1” photon formulation. Similarly, at  $\nu \leq \nu_{21}$  the contribution to the total absorption optical depth becomes *larger* than in the standard case, because there  $\phi_{3d \rightarrow 1s} \gtrsim \phi_\nu$ .

In Fig. 3, lower panel, we illustrate these effects on  $\tau_{\text{abs}}$  for the 3-shell hydrogen atom. However, here we used the full absorption profile,  $\phi_{\text{abs}}^*$ , which at  $\nu \gtrsim \nu_{31}$  has a small contribution from the Voigt profile used to model the continuum channel

( $1s \leftrightarrow 2p \leftrightarrow c$ ). Therefore, the optical depth does not vanish at  $\nu \gg \nu_{31}$ . The additional differences to the values of the optical depth seen in Fig. 3 confirm the above statements. Comparing with the case for the thermodynamic factor (central panel), it is clear that the correction to  $\tau_{\text{abs}}$  due to the shape of the absorption profile is not as important.

One should also mention that setting  $\Theta^a = 1$  and  $f_\nu = 1$ , we obtain the solution  $F_0^\phi$  as given by Eq. (15). With the comments made above, one therefore expects a sharp decline in the value of  $F_0^\phi$  for  $\nu \rightarrow \nu_{31}$ , since  $\tau_{\text{abs}} \rightarrow 0$ . Numerically, we indeed find this behavior (see Sect. 4).

### 3.4. Time and frequency dependence of the effective emissivity

If we look at the definition of  $\Theta^a$ , i.e., Eq. (8c), and rewrite it as

$$\Theta^a(z, z') = \frac{1}{f_{\nu'}} [\Theta^t + \Theta^\phi] \quad (19a)$$

$$\Theta^t(z, z') = \frac{\tilde{N}_{\text{em}}(z') - \tilde{N}_{x_{21}}^{\text{pl}}}{\tilde{N}_{\text{em}}(z) - \tilde{N}_{x_{21}}^{\text{pl}}} \quad (19b)$$

$$\Theta^\phi(z, z') = \frac{\tilde{N}_{\text{em}}(z')}{\tilde{N}_{\text{em}}(z) - \tilde{N}_{x_{21}}^{\text{pl}}} \times \left[ \frac{\phi_{\text{em}}(\nu', z')}{\phi_{\text{abs}}^*(\nu', z')} - 1 \right], \quad (19c)$$

we can clearly see that there are also three sources for the corrections to the effective emissivity. The first is related to the *purely time-dependent* correction ( $\Theta^a = \Theta^t$ ), the second to the *thermodynamic correction factor* ( $\Theta^a = 1/f_{\nu'}$ ), and the third to the *quantum mechanical asymmetry*<sup>10</sup> between the emission and absorption profile ( $\Theta^a = \Theta^\phi$ ). Below we now briefly discuss the expected consequences of each of these.

#### 3.4.1. Purely time-dependent correction to $\Theta^a$

For  $\Theta^a = \Theta^t$ , we consider the purely time-dependent correction to the emission coefficient. This correction has already been discussed in detail (Chluba & Sunyaev 2009c). For quasi-stationary conditions, one would have  $\Theta^t = 1$ . However, in the cosmological recombination problem  $\Theta^t \neq 1$  most of the time. This leads to significant changes in the shape of the spectral distortion at different redshifts, where at frequencies  $x_D \lesssim 0$  only  $\Theta^t \neq 1$  is able to affect the distortion (Chluba & Sunyaev 2009c).

#### 3.4.2. Effect of thermodynamic correction factor in $\Theta^a$

If we only include the correction due to the thermodynamic factor  $f_\nu$ , then we have  $\Theta^a = 1/f_{\nu'}$ . Since for  $\nu' = \nu \frac{1+z}{1+z'} \neq \nu_{21}$ , one has  $f_{\nu'} \neq 1$ , so that due to  $f_{\nu'}$  one expects a similar effect on the shape of the distortion like from  $\Theta^t$ . However, since  $f_{\nu'} \gg 1$  at large detuning blueward of the line center, this correction can be very large. As mentioned in Sect. 3.3, from Eq. (15), one naively expects  $F_0 \rightarrow 1$ , but when including the factor  $1/f_{\nu'}$  in  $\Theta^a$  instead we find that  $F_\nu \sim 1/f_\nu$  at large  $x_D$ .

To show this, we consider the solution for  $F(\nu, z)$  in this case, assuming that the quasi-stationary approximation ( $\Delta z/z \ll 1$  and  $\Delta\nu/\nu \ll 1$ , between the emission and absorption redshift of the photons) is possible. Introducing the new variable

<sup>10</sup> More clearly, here one should refer to the mixture of quantum mechanical processes important to the emission and absorption profile.

$\chi(\nu) = \int_0^\nu \phi_{\text{abs}}^*(\nu') d\nu'$ , and using  $\tau_{\text{abs}}^{\text{qs}} \approx \tau_{\text{d}}(z) f_{\nu}(z) [\chi' - \chi]$ , where  $\chi' = \chi(\nu')$ , one has

$$F_{\text{f}}^{\text{qs}}(\nu, z) = \int_z^{z_s} \frac{c \sigma_{\text{r}}(z') N_{1\text{s}}(z')}{H(z')(1+z')} \phi_{\text{abs}}^*(\nu', z') e^{-\tau_{\text{abs}}(\nu, z', z)} dz' \quad (20\text{a})$$

$$\approx \tau_{\text{d}}(z) \int_0^{\chi_s} d\chi' e^{-\tau_{\text{d}} f_{\nu} [\chi' - \chi]} = \frac{1 - e^{-\tau_{\text{d}} f_{\nu} [\chi_s - \chi]}}{f_{\nu}(z)}. \quad (20\text{b})$$

Since  $\tau_{\text{d}} f_{\nu} [\chi_s - \chi] \rightarrow \infty$  for  $x_{\text{D}} \gg 1$ , there one has  $F(\nu, z) \rightarrow 1/f_{\nu}(z)$ . In addition, one expects that  $F(\nu, z) \sim 1/f_{\nu}(z)$  for  $x_{\text{D}} \lesssim 1$ . As we show below, for the correction due to the thermodynamic factor the scaling  $F(\nu, z) \sim 1/f_{\nu}(z)$  indeed is correct at  $x_{\text{D}} \gg 1$  and  $x_{\text{D}} \sim 1$ . However, at  $x_{\text{D}} \rightarrow -\infty$  one instead finds  $F(\nu, z) \sim 1$ , implying that the simple quasi-stationary approximation is not possible.

### 3.4.3. Correction related to the quantum-mechanical asymmetry between emission and absorption profile

Since in general the admixture of the different transition channels to the emission and absorption profile is *not* identical, one does expect that  $\phi_{\text{abs}}^* \neq \phi_{\text{em}}$ . We can also consider the difference between  $\phi_{\text{abs}}^*$  and  $\phi_{\text{em}}$ , which will be given by

$$\Delta\phi(\nu) = \phi_{\text{abs}}^* - \phi_{\text{em}} = \sum_i \left[ \frac{R_{2\text{p}}^{i-}}{R_{2\text{p}}^-} - \frac{R_{2\text{p}}^{i+}}{R_{2\text{p}}^+} \right] \phi_i(\nu). \quad (21)$$

Since in full thermodynamic equilibrium  $(R_{2\text{p}}^{i+})^{\text{eq}} \equiv (R_{2\text{p}}^{i-} N_{2\text{p}})^{\text{eq}}$ , it is clear that  $(R_{2\text{p}}^{i-}/R_{2\text{p}}^-)^{\text{eq}} \equiv (R_{2\text{p}}^{i+}/R_{2\text{p}}^+)^{\text{eq}}$ , so that  $\Delta\phi \equiv 0$ . On the other hand, it is known (e.g., see [Chluba et al. 2007](#)) that in the cosmological recombination problem  $R_{2\text{p}}^{i-}$  and  $R_{2\text{p}}^{i+}$  should always be very close to their equilibrium values, so that one expects  $\Delta\phi/\phi \ll 1$ . Only at low redshifts ( $z \lesssim 800$ ) may this condition not be fulfilled. However, as we see below for CMB power spectrum computations, this aspect of the problem is never important (see Sect. 4).

## 4. Changes to the Lyman $\alpha$ spectral distortion

We show the detailed dependence of the resulting Lyman  $\alpha$  spectral distortion on the different corrections that are taken into account. As explained above, three types of corrections are considered here: (i) the time-dependent correction; (ii) the thermodynamic correction factor  $f_{\nu}$ ; and (iii) the dependence on the detailed shape of the effective line emission and absorption profiles. We start our discussion by including these corrections first only in the computation of  $\tau_{\text{abs}}$  but setting  $\Theta^{\text{t}} = 1$  and  $\Theta^{\phi} = 0$  (Sect. 4.1). In Sect. 4.2, we also allow for  $\Theta^{\text{t}} \neq 1$ , but still set  $\Theta^{\phi} = 0$ . Finally, we also include the correction due to  $\Theta^{\phi} \neq 0$  (Sect. 4.3), but this aspect of the problem is not found to be very important. It should be possible to deduce all the other combinations from these cases.

### 4.1. Corrections related to $\tau_{\text{abs}}$ for $\Theta^{\text{t}} = 1$ and $\Theta^{\phi} = 0$

As a first case, we study the effect of different corrections to the absorption optical depth. For this we set  $\Theta^{\text{t}} = 1$  and  $\Theta^{\phi} = 0$ , meaning that in the emission coefficient  $\Theta^{\text{a}}$  we ignore both the purely time-dependent correction and the one related to the shape of the profile. However, depending on the case considered, we do allow for these corrections in the computation of  $\tau_{\text{abs}}$ .

In addition, we also discuss the effect of the thermodynamic correction factor,  $f_{\nu}$ . but here we include it in both  $\tau_{\text{abs}}$  and  $\Theta^{\text{a}}$  at the same time. As explained Sect. 3.4.2, if one were to include only  $f_{\nu}$  for  $\tau_{\text{abs}}$  or  $\Theta^{\text{a}}$  separately, the corresponding spectral distortion would not be physically very meaningful. Therefore, we omit this case here.

#### 4.1.1. Behavior very close to the line center

As an example, in Fig. 4 we show the Lyman  $\alpha$  spectral distortion at  $z = 1100$  in the close vicinity of the line center. We compare the results with the normal quasi-stationary solution (see [Chluba & Sunyaev 2009c](#), for details)

$$F^{\text{qs}}(\nu, z) = 1 - e^{-\tau_{\text{d}}} e^{\tau_{\text{d}} \chi}, \quad (22)$$

with  $\chi = \int_0^\nu \varphi_{\nu}(\nu') d\nu'$ . We show the result obtained for the pure time-dependent correction to  $\tau_{\text{abs}}$  (dashed curve), which was already discussed earlier ([Chluba & Sunyaev 2009c](#)). At  $x_{\text{D}} \lesssim 4$ , the distortion is practically identical to the result for the quasi-stationary case, while at  $x_{\text{D}} \gtrsim 4$  the time-dependent corrections to  $\tau_{\text{abs}}$  begin to be important. One can see that there  $F_{\nu} = 1 - e^{-\tau_{\text{abs}}} \gtrsim F_{\nu}^{\text{qs}}$ , which, as explained in Sect. 3.3.1, is related to including the time-dependent correction, so that at this redshift the value of  $\tau_{\text{abs}}$  is slightly larger than in the quasi-stationary approximation, leading to<sup>11</sup>  $\tau_{\text{abs}}^{\text{t}} \gtrsim \tau_{\text{abs}}^{\text{qs}}$ .

If we also include the correction due to the shape of the absorption profile in the computation of  $\tau_{\text{abs}}$  (dashed-dotted curve), then we see that at  $x_{\text{D}} \lesssim 0$  again the solution is practically identical to the solution in the quasi-stationary case. Although one does expect some corrections to the exact value of  $\tau_{\text{abs}}$  at different frequencies below the line center<sup>12</sup>, since  $\tau_{\text{abs}} \gg 1$  the effect on the shape of  $F_{\nu} \sim 1 - e^{-\tau_{\text{abs}}}$  will be exponentially small. However, looking at  $x_{\text{D}} \gtrsim 4$  we can see that  $F_{\nu} \lesssim F_{\nu}^{\text{qs}}$ , implying that  $\tau_{\text{abs}}^{\text{t},\phi} \lesssim \tau_{\text{abs}}^{\text{qs}}$ . Since blueward of the resonance  $\phi_{\text{abs}}^* \lesssim \phi_{\nu}$  (see right panel of Fig. 2), it is already expected that the curve lies below that for the purely time-dependent correction (i.e.  $\tau_{\text{abs}}^{\text{t},\phi} \lesssim \tau_{\text{abs}}^{\text{t}}$ ). However, it is found that the correction related to the shape of  $\phi_{\text{abs}}^*$  overcompensates the purely time-dependent effect, which alone leads to  $\tau_{\text{abs}}^{\text{t}} \gtrsim \tau_{\text{abs}}^{\text{qs}}$ . This shows that at the considered redshift the correction related to the profile is slightly more important than the time-dependence.

If we now only include the time-dependent correction and the effect of the thermodynamic correction factor (in both  $\tau_{\text{abs}}$  and  $\Theta^{\text{a}}$ ), then we obtain the dotted line. As expected from Eq. (20), very close to the Doppler core ( $|x_{\text{D}}| \lesssim 4$ ) one has  $F_{\nu}(z) \sim 1/f_{\nu}(z)$ . We also found this scaling at other redshifts (marginally visible in Fig. 5), as long as the optical depth across the Doppler core is much larger than unity, implying that the quasi-stationary approximation is valid. However, outside this region the distortion differs significantly from the previous cases. In particular, one finds  $F_{\nu} \gtrsim F_{\nu}^{\text{qs}}$  at  $x_{\text{D}} \lesssim -4$ , which is the result of  $\Theta^{\text{a}} = 1/f_{\nu}$ . If we include the thermodynamic correction factor only in the computation of  $\tau_{\text{abs}}$ , i.e., by setting  $\Theta^{\text{a}} = 1$ , then we instead find  $F_{\nu} \sim 1$ .

It is also found that  $F_{\nu} \lesssim 1/f_{\nu}$  at  $x_{\text{D}} \lesssim -4$ . This is in contrast to the result for  $F_{\text{f}}^{\text{qs}}(\nu, z)$ , given by Eq. (20), for which we assume quasi-stationary conditions. This implies that in the red damping

<sup>11</sup> The upper indices will henceforth indicate the included correction. ‘‘t’’ represents the time-dependent correction, ‘‘f’’ the thermodynamic factor, and ‘‘ $\phi$ ’’ the profile correction. When all corrections are included simultaneously, we use ‘‘a’’.

<sup>12</sup> Since in the red wing  $\phi_{\text{abs}}^* \gtrsim \phi_{\nu}$  (cf. Fig. 2), one expects  $\tau_{\text{abs}}^{\phi} \gtrsim \tau_{\text{abs}}^{\text{qs}}$ .

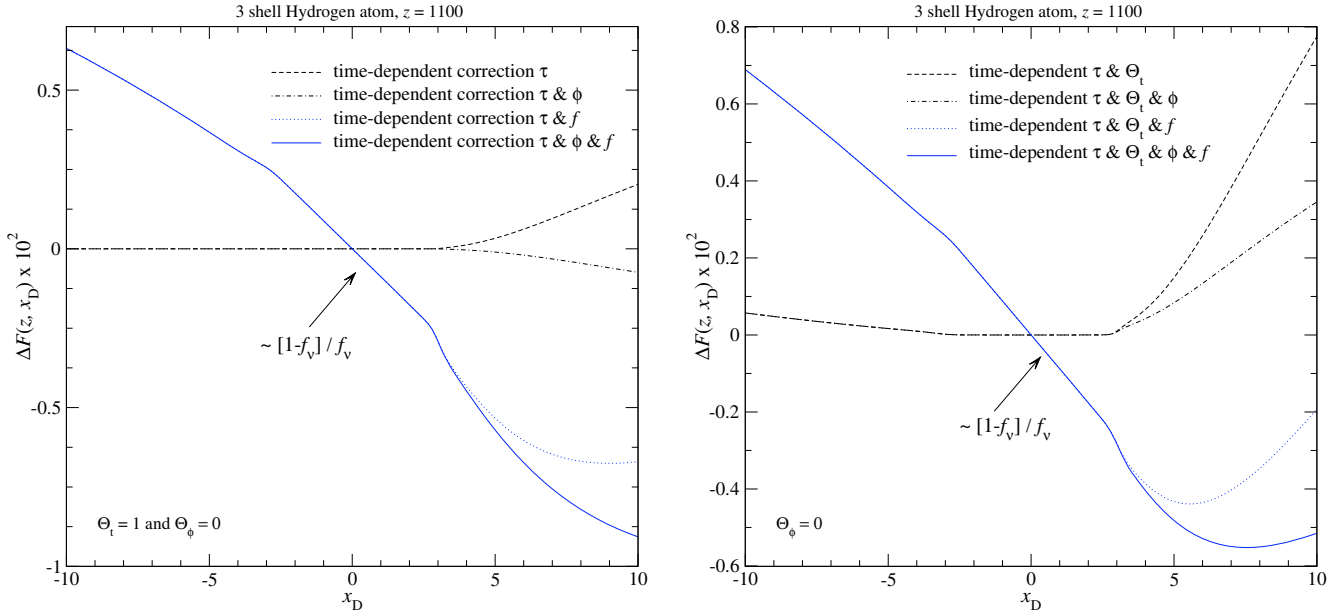


**Fig. 4.** Difference in the Lyman  $\alpha$  spectral distortion with respect to the quasi-stationary solution in the no-redistribution approximation,  $F^{\text{qs}}(\nu, z)$  as given by Eq. (22), at  $z = 1100$  close to the line center. For all computations shown in *the left panel*, we set  $\Theta^t = 1$  and  $\Theta^\phi = 0$ , while in *the right panel* we only set  $\Theta^\phi = 0$ . The cases labeled with  $f$  are computed using  $\Theta^a = 1/f_\nu$  (*left panel*) and  $\Theta^a = \Theta^t/f_\nu$  (*right panel*), while for the others we set  $f_\nu = 1$ . In addition, the quoted correction factors were included in the computation of  $\tau_{\text{abs}}(\nu, z_s, z')$ . We assumed a 3-shell hydrogen atom.

wing deviations from the quasi-stationary assumption become important.

In addition, if we include the correction due to the shape of the absorption profile, then we can see that at  $x_D \lesssim 4$  the curve basically coincides with that from the previous case. This again is expected since the tiny corrections to the value of a very large optical depth will not lead to visible changes in  $F_\nu$ . In addition, at  $x_D \gtrsim 4$  one can see that the differences to the previous case are about the same as for the differences between the first two cases, owing to the corrections being small and hence additive.

#### 4.1.2. Behavior at intermediate and large distances from the line center

We now consider the corrections in a slightly wider range around the line center. In Fig. 5, we show the same cases as above, but now also varying the redshift. As before, one can see that differences due to the shape of the absorption profile are negligible at  $x_D \lesssim 0$ . Furthermore, on the blue side of the resonance the correction due to the shape of the absorption profile is always negative, as also seen in the previous paragraph.

Taking the differences between the curves for  $\Theta^a = 1$  (first two lines), and those for  $\Theta^a = 1/f_\nu$  (last two lines) one can also see that at  $z = 1200$  these are practically the same. However, for  $z = 1000$  and  $z = 800$ , higher order terms already start to become important. For example, at  $x_D = 100$ , the difference in the curves for  $\Theta^a = 1$  is  $\sim 2 \times 10^{-3}$ , while it is about  $8 \times 10^{-4}$  for those with  $\Theta^a = 1/f_\nu$ .

If we consider the distortion for an even wider range of frequencies (Fig. 6), then we can make several important observations. First, as expected from the discussion related to Eq. (20), in the limit  $x_D \rightarrow \infty$  for  $\Theta^a = 1/f_\nu$  one finds that  $F_\nu \sim 1/f_\nu$ , regardless of whether the normal Voigt profile was used or the effective absorption profile, given by Eq. (5a). However, for  $\phi_{\text{abs}}^* = \phi_\nu$  the limit  $F_\nu \sim 1/f_\nu$  is reached closer to the line center than for the effective absorption profile. This is expected, since for the 3-shell atom the effective absorption profile only has a

small admixture of the Voigt profile (because of the description of the route connecting to the continuum). If  $\phi_{\text{abs}}^* = \phi_{3d}$ , then the limit  $F_\nu \sim 1/f_\nu$  would never be reached, simply because at  $\nu \gtrsim \nu_{31}$  the contribution to  $\tau_{\text{abs}}$  would be zero. Reducing the admixture of the pure Voigt profile therefore moves the transition to  $F_\nu \sim 1/f_\nu$  towards higher frequencies.

The second important observation is that in the frequency range  $\nu_{21} \lesssim \nu \lesssim \nu_{31}$  on the blue side of the resonance the correction due to the shape of the absorption profile is far more important than both the pure time-dependent correction to  $\tau_{\text{abs}}$  and the correction due to the  $1/f_\nu$  factor in  $\Theta^a$ . And finally, in the red wing the correction to the spectral distortion is dominated by the  $1/f_\nu$  scaling of  $\Theta^a$ , although the correction is very small, in particular in comparison to that coming from  $\Theta^t$  (see Sect. 4.2).

#### 4.2. Corrections related to both $\tau_{\text{abs}}$ and $\Theta^t$ but for $\Theta^\phi = 0$

We now want to understand the effect of changes to the ionization history and death probability on the effective emission rate. We therefore allow  $\Theta^t \neq 1$ , but still set  $\Theta^\phi = 0$ . We then again discuss different combinations of corrections, as in the previous section. As we see, the corrections related to  $\Theta^t \neq 1$  dominate at large distances on the red side of the resonance, while the shape of the profile is most important to the spectral distortion on the blue side of the resonance (see Fig. 6). In the vicinity of the resonance, basically *all* the correction factors are important.

##### 4.2.1. Behavior very close to the line center

In Fig. 4, we show the Lyman  $\alpha$  spectral distortion at  $z = 1100$  in the very close vicinity of the line center, now also including  $\Theta^t \neq 1$ . If we first look at the curves for  $f_\nu = 1$  (dashed and dashed-dotted), then we can see that very close to the resonance ( $|x_D| \lesssim 4$ ) the solution is unaffected by the inclusion of  $\Theta^t \neq 1$ . Due to the huge optical depth across the Doppler core (corresponding to  $\Delta z/z \sim 10^{-5}$ ), practically any time-dependent variation in the effective emission coefficient is erased. However,

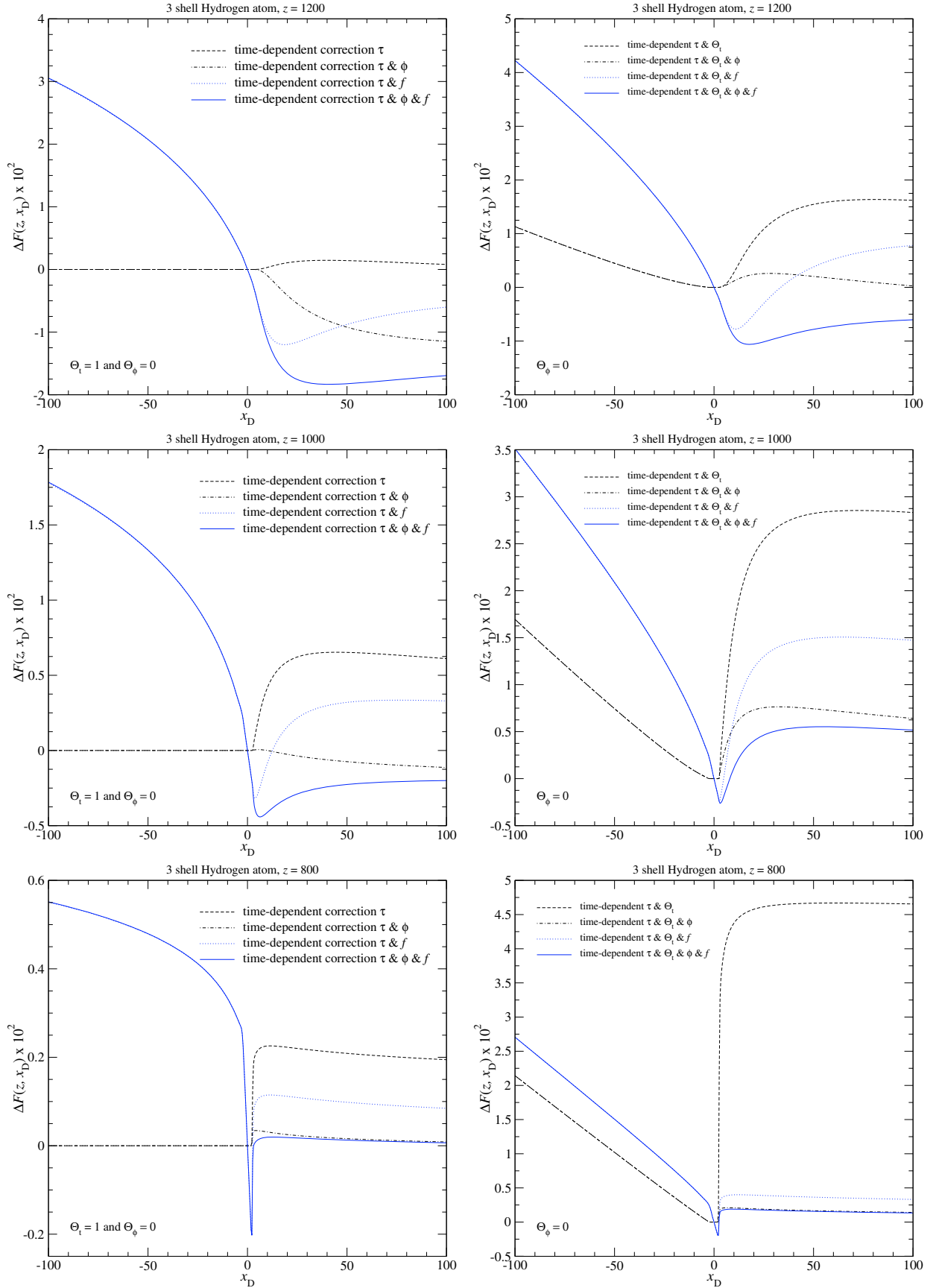


**Fig. 5.** Difference in the Lyman  $\alpha$  spectral distortion with respect to the quasi-stationary solution in the no-redistribution approximation,  $F^{\text{qs}}(\nu, z)$ , as given by Eq. (22), at several redshifts close to the line center. For all computations shown in the left column, we set  $\Theta^i = 1$  and  $\Theta^\phi = 0$ , while in the right we only set  $\Theta^\phi = 0$ . The cases labeled with  $f$  are computed using  $\Theta^a = 1/f_{\nu'}$  (left column) and  $\Theta^a = \Theta^i/f_{\nu'}$  (right column), while for the others we set  $f_\nu = 1$ . In addition, the quoted correction factors were included for  $\tau_{\text{abs}}(\nu, z_s, z')$ . We assumed a 3-shell hydrogen atom.

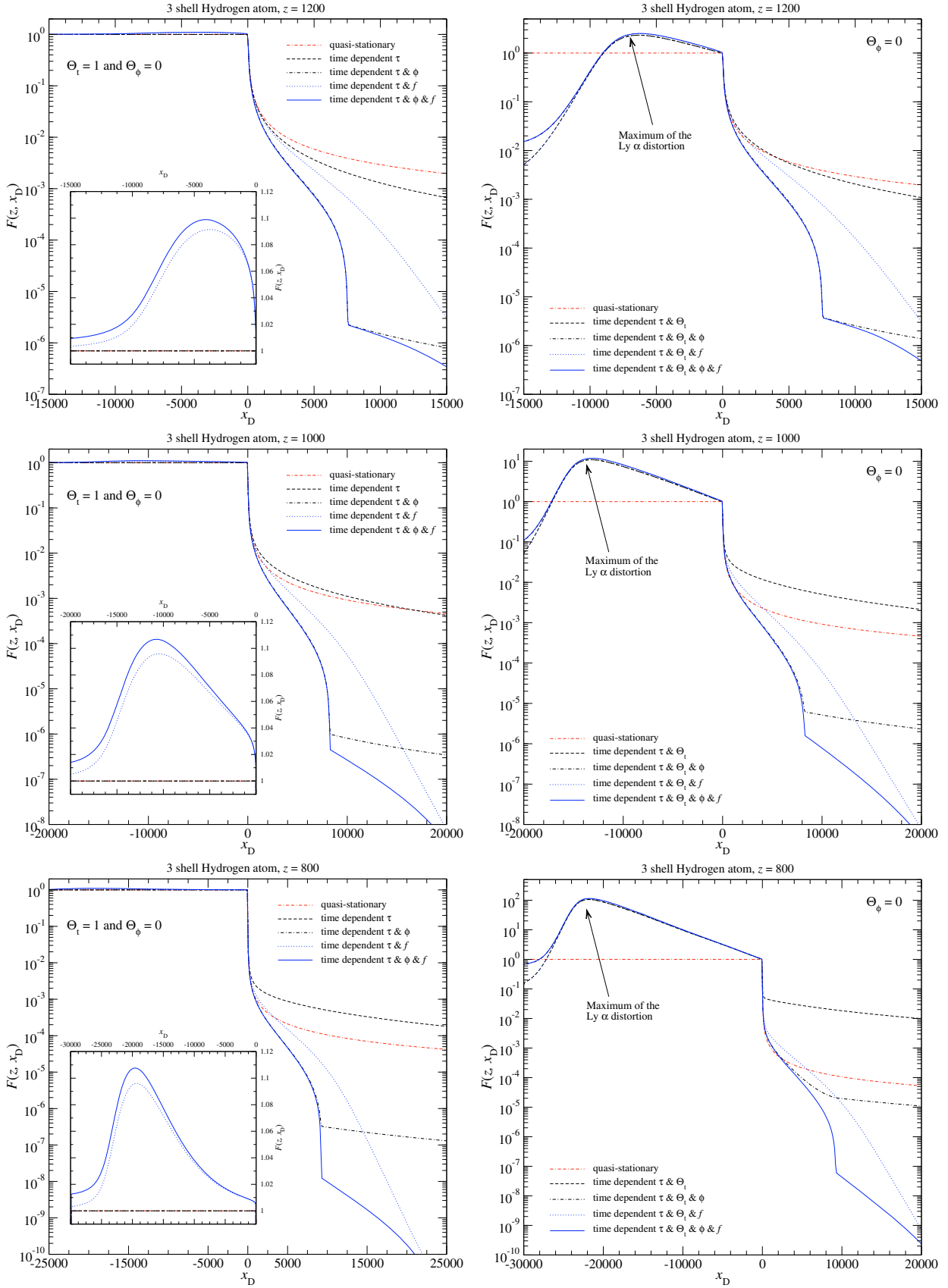


**Fig. 6.** The Lyman  $\alpha$  spectral distortion at different redshifts and in a wide range of frequencies around the line center. For all computations shown in the left column we set  $\Theta^t = 1$  and  $\Theta^\phi = 0$ , while in the right we only set  $\Theta^\phi = 0$ . The cases labeled with  $f$  are computed using  $\Theta^s = 1/f_\nu$  (left column) and  $\Theta^s = \Theta^t/f_\nu$  (right column), while for the others we set  $f_\nu = 1$ . In addition, the quoted correction factors were included for  $\tau_{\text{abs}}(\nu, z_s, z')$ . We assumed a 3-shell hydrogen atom.

moving towards the wings, time-dependent aspects become important and in particular,  $F_\nu \neq F_\nu^{\text{qs}}$  at  $x_D < 0$ .

At the considered redshift, the difference from the case  $\Theta^t = 1$  (see Fig. 4) is very small at  $x_D \lesssim -4$ . Clearly, the correction due to the thermodynamic factor  $f_\nu$  (dotted and solid lines) is dominant. However, at  $x_D \gtrsim 4$  the time-dependent changes in the effective emission coefficient lead to a correction that is as important as that due to  $f_\nu$ . One can also see that all the corrections add roughly linearly. We note that at  $x_D < 4$  the curves are not affected when accounting for corrections to the shape of the line profile.

#### 4.2.2. Behavior at intermediate and large distances from the line center

Looking at the right column of Fig. 5, we can see that at  $x_D \lesssim 0$  the correction due to the inclusion of  $f_\nu$  dominates at high redshift, while at  $z \sim 1000$  the correction due to  $\Theta^t$  is already comparable, and clearly dominates at low redshift. In addition, at  $x_D \gtrsim 0$  one can see that at high redshift all the corrections practically add linearly, while for  $z = 1000$  and  $z = 800$  the correction due to the inclusion of  $\Theta^t$  practically disappears when including the correct shape of the effective absorption profile. When also including the thermodynamic correction factor the large excess of photons seen for the case  $f_\nu = 1$  and  $\phi_{\text{abs}} = \phi_\nu$  practically vanishes. This implies that the *self-feedback* effect at low redshifts reported elsewhere (Chluba & Sunyaev 2007) is expected to disappear. As explained there, this unphysical aspect of the solution in the “1 + 1” photon pictures is caused by the Voigt profile in principle extending up to arbitrarily high frequencies, so that photons emitted at  $z \sim 1400$  in the very distant blue damping wing will still be able to reach the line center at low redshift, strongly enhancing the photon occupation number. However, when including the thermodynamic correction factor, because of the exponential enhancement of the absorption optical depth at large distances blueward of the resonance, these photons disappear much before this. Similarly, when including the shape of the effective emission profile this excess of photons will never be produced in the first place, so that from this region the residual correction due to  $\Theta^t \neq 1$  is much smaller.

Looking at the spectral distortion for a very wide range of frequencies around the line center (Fig. 6), it is clear that at all redshifts the shape of the distortion is dominated by the correction due to  $\Theta^t \neq 1$  for  $x_D \lesssim 0$ . Both the thermodynamic factor and the shape of the absorption and emission profile only lead to small additional modifications. The largest correction is related to the 3d two-photon emission profile being larger than the Voigt profile at  $\nu \rightarrow \nu_{31}/2$ , explaining the small addition of photons in comparison to the case  $\phi_{\text{abs}}^* = \phi_\nu$  seen close to the lowest frequencies shown in the figures. On the other hand, at frequencies above the line center the correction due to the shape of the line profile is clearly most important. In the line center, all sources of correction contribute to changes to the Lyman  $\alpha$  spectral distortion relative to the quasi-stationary solution.

#### 4.3. Corrections related to $\tau_{\text{abs}}$ and $\Theta^t$ including $\Theta^\phi \neq 0$

We also considered cases for  $\Theta^\phi \neq 0$ . However, the correction was always extremely small. Therefore, we decided to omit the corresponding plots for  $F_\nu$ . As mentioned in Sect. 3.2, this is expected since the deviations of  $R_{2p}^{i,-}/R_{2p}^-$  and  $R_{2p}^{i,+}/R_{2p}^+$  from their equilibrium values is always very small in the relevant redshift range, so that  $R_{2p}^{i,+}/R_{2p}^+ \approx R_{2p}^{i,-}/R_{2p}^-$ , and hence

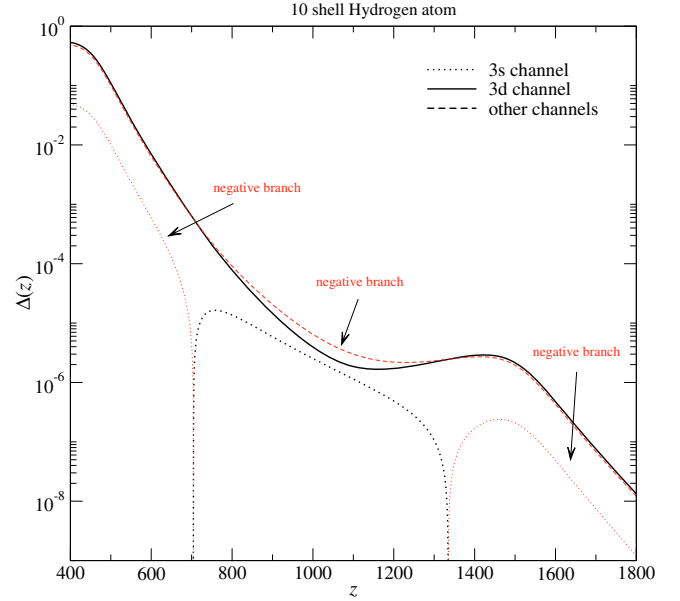


**Fig. 7.** Source of the asymmetry between the absorption and emission profiles,  $\phi_{\text{abs}}^*$  and  $\phi_{\text{em}}$ . We present  $\Delta(z) = R_{2p}^{i,-}/R_{2p}^- - R_{2p}^{i,+}/R_{2p}^+$  for a given level as a function of redshift. For all curves, we used the solution for the 10-shell hydrogen atom.

$\phi_{\text{abs}}^* \approx \phi_{\text{em}}$ . In Fig. 7, we explicitly show this fact. As an example, for the 3d-channel one can see that at  $z \sim 1100$  one has  $R_{2p}^{3d,-}/R_{2p}^- - R_{2p}^{3d,+}/R_{2p}^+ \sim 10^{-6} - 10^{-5}$ . Therefore, one would expect corrections to the effective escape probability at the level of  $\sim 10^{-4} - 10^{-3}\%$ , which is clearly negligible in the context of the CMB anisotropies. We confirmed this statement numerically.

One should also mention that, although at low redshift the expected difference between emission and absorption profile increases, the value of the effective escape probability is dominated by the contribution from the Doppler core, where details of the profiles do not matter. In addition, corrections to the escape probability will not affect the ionization history significantly, so that here we do not discuss this point any further.

## 5. Changes to the effective escape probability

### 5.1. Effect of the thermodynamic correction factor

First we consider the normal Lyman  $\alpha$  transfer equation given in Eq. (1), but including the thermodynamic correction factor  $f_\nu$ , to correct for the small imbalance between the emission and absorption process in the line wings originating from the normal “1 + 1” photon formulation (see Sect. 2.1.1). In this case, one has  $\phi_i(\nu) = \phi_\nu(\nu)$  and hence  $\phi_{\text{em}} \equiv \phi_{\text{abs}}^* \equiv \phi_\nu(\nu)$ , so that from Eq. (8b) one can find

$$F_\nu^t = \int_{z_s}^z \Theta^t(z, z') \partial_{z'} e^{-\tau_{\text{abs}}(\nu, z', z)} dz' \quad (23a)$$

$$\Theta^t(z, z') = \frac{1}{f_\nu(z')} \frac{\tilde{N}_{\text{em}}(z') - \tilde{N}_{x_{21}}^{\text{pl}}}{\tilde{N}_{\text{em}}(z) - \tilde{N}_{x_{21}}^{\text{pl}}} = \frac{\Theta^t(z, z')}{f_\nu(z')}, \quad (23b)$$

where  $\tau_{\text{abs}}$  is given by Eq. (5a) but for  $\phi_{\text{abs}}^*(\nu) \rightarrow \phi_\nu(\nu)$ .

If one drops the factors related to  $f_\nu$  in the definition of  $\Theta^t$  and also  $\tau_{\text{abs}}$ , one obtains the purely time-dependent case,  $F_\nu^t$ , that was addressed earlier (Chluba & Sunyaev 2009c). However, here the term  $\Theta^t$  is naturally given by the line center values of

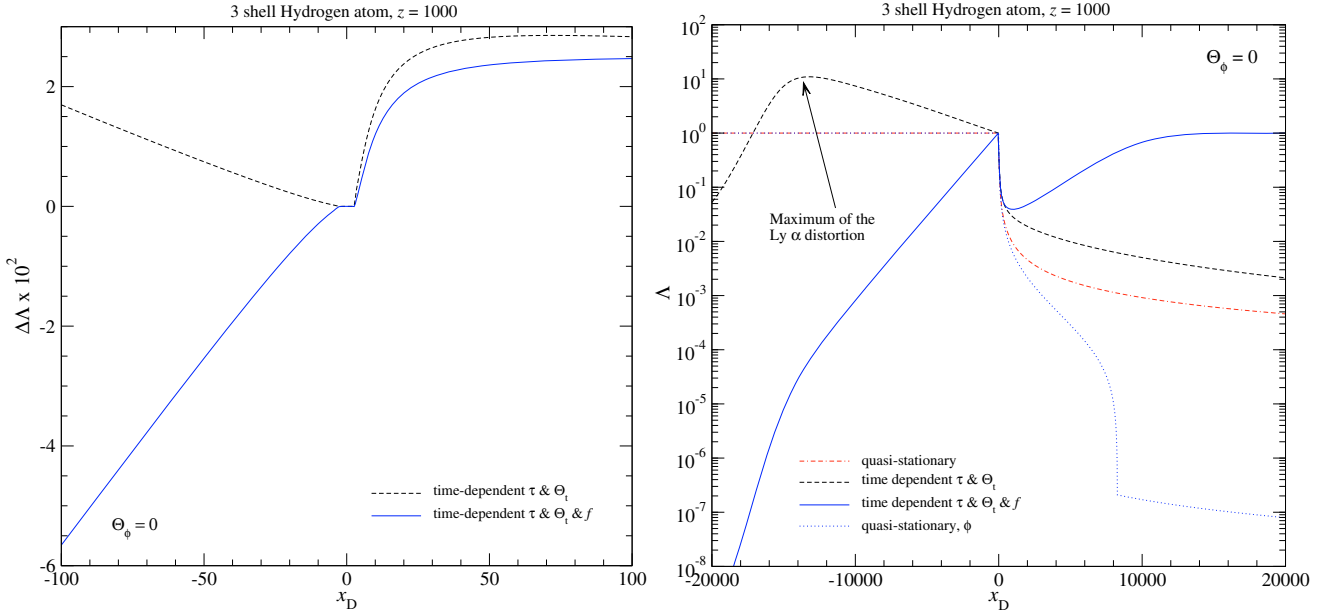


**Fig. 8.** The functions  $\mathcal{F}_\nu^f = f_\nu F_\nu^f$  at redshift  $z = 1000$ . In the left panel, we show the difference  $\Delta\Lambda = \mathcal{F}_\nu^f - F_\nu^{\text{qs}}$ , while in the right we directly show  $\Lambda = \mathcal{F}_\nu$ . The cases labeled with  $f$  are computed using  $\Theta^a = \Theta^i/f_\nu$ , the others with  $\Theta^a = \Theta^i$ . In addition, the quoted correction factors were included in the computation of  $\tau_{\text{abs}}(\nu, z_s, z')$ . For comparison, in the right panel we also directly show the normal quasi-stationary solution  $F_\nu^{\text{qs}}$  (double dash dotted line) and  $F_\nu^{\phi, \text{qs}}$  (dotted line) that includes the correction due to the profile  $\phi_{\text{abs}}^* \neq \phi_\nu$  (see Sect. 5.2.2). We assumed a 3-shell hydrogen atom.

$\tilde{N}_{\text{em}}(z') - \tilde{N}_x^{\text{pl}}$ , which in the previous work had to be enforced for consistency with the standard approximations (see comments in Sect. 3.4.1 of Chluba & Sunyaev 2009c).

To understand the role of  $f_\nu$  in the final correction to  $P_{\text{eff}}$ , in Eq. (12b), we first consider the term  $\Delta P_{\text{ind}}$ , in Eq. (12c). It is clear that for  $\phi_{\text{em}} = \phi_{\text{abs}}^* = \phi_\nu$ , one has  $\Delta P_{\text{ind}} \equiv 0$ , since  $\Delta\varphi_{\text{em}} \equiv \Delta\varphi_{\text{abs}}^* = 0$ . As we show below (Sect. 5.2.1),  $\Delta P_{\text{ind}} \neq 0$  when taking into account the effect of stimulated emission in the blackbody radiation field, although, the contribution to the final correction is found to be negligible.

If we now consider the definition of  $P$ , in Eq. (10b), then for the considered case we can rewrite this as

$$P^f = \int \varphi_\nu(\nu) [1 - \mathcal{F}_\nu^f] d\nu, \quad (24)$$

where we have introduced the function

$$\mathcal{F}_\nu^f = f_\nu(z) F_\nu^f. \quad (25)$$

This representation allows us to see directly the expected differences compared to the standard quasi-stationary case, for which one has ( $\varphi_{\text{em}} = \varphi_{\text{abs}}^* \equiv \varphi_\nu$  and  $f_\nu \equiv 1$ )

$$\mathcal{F}_\nu^{\text{qs}} \equiv F_\nu^{\text{qs}} = 1 - e^{-\tau_d} e^{\tau_d \chi}. \quad (26)$$

If instead of  $\mathcal{F}_\nu^f$  we insert this into Eq. (24), we directly obtain  $P_d = \frac{1 - e^{-\tau_d}}{\tau_d}$ . Therefore, we can write the correction with respect to the quasi-stationary solution as

$$\Delta P_d^f = P^f - P_d = - \int \phi_\nu(\nu) [\mathcal{F}_\nu^f - \mathcal{F}_\nu^{\text{qs}}] d\nu. \quad (27)$$

This expression shows that for the correction to the effective escape probability, it is not important how  $F_\nu^f$  behaves, but how  $\mathcal{F}_\nu^f$  looks. Since  $f_\nu$  is a very strong function of frequency, this makes a large difference to the conclusions, as we explain below. Furthermore, any difference to the value of  $\mathcal{F}_\nu^{\text{qs}}$  will lead to

a contribution to  $\Delta P_d^f$  of opposite sign. It is also possible to compute the *partial contributions* to the total correction in the escape probability by only integrating  $\Delta P_d^f$  as defined by Eq. (27) over a given range of frequencies.

### 5.1.1. Behavior of $\mathcal{F}_\nu^f$ and the expected corrections to $P_{\text{eff}}$

In Fig. 8, as an example we show  $\mathcal{F}_\nu^f$  at redshift  $z = 1000$  (dotted lines). For comparison, we also show the purely time-dependent solution (dashed curves) for which  $\mathcal{F}_\nu^f \equiv F_\nu^f$ . We note that we include the correction terms in both  $\tau_{\text{abs}}$  and  $\Theta^a$ .

If we focus on the behavior at  $-100 \leq x_D \lesssim -4$ , then we can see that although in the considered cases  $F_\nu^f > F_\nu^t > F_\nu^{\text{qs}}$  (compare with Fig. 5, right column, case  $z = 1000$ ), for  $\mathcal{F}_\nu^f$  one has  $\mathcal{F}_\nu^t > \mathcal{F}_\nu^{\text{qs}} > \mathcal{F}_\nu^f$ . This change in the sequence is related only to the factor  $f_\nu < 1$  in the definition of  $\mathcal{F}_\nu^f$ , which appears because  $\phi_{\text{abs}} = f_\nu \phi_{\text{abs}}^*$  in the escape integral, Eq. (10b). Instead of an additional *negative* contribution to the escape probability ( $\Delta P^f < \Delta P^t < 0$ ), as would follow from the differences seen in  $F_\nu$ , when including the thermodynamic correction factor  $f_\nu$  one therefore expects a *positive* contribution from the considered spectral region. This effect becomes even more apparent when looking at the very distant red wing, where clearly  $\mathcal{F}_\nu^t > \mathcal{F}_\nu^{\text{qs}} \gg \mathcal{F}_\nu^f$ , owing to the exponential cutoff introduced by  $f_\nu$ . The behavior shows that in the very distant red wing the excess Lyman  $\alpha$  photons no longer supports the flow of electrons toward higher levels and the continuum. These photons only undergo line-scattering events, with tiny shifts in the frequency caused by the Doppler motion of the atom, but do not disappear anymore, and therefore effectively escape. As we demonstrate below (Sects. 5.1.4 and 5.1.5), the main correction related to  $f_\nu$  is from the change in the absorption cross-section in the red wing of the line profile. The true modifications to the spectral distortion due to  $f_\nu$  are not so important.

If we now look at the behavior in the range  $4 \leq x_D \lesssim 100$ , we can see that the sequence  $F_\nu^t > F_\nu^f > F_\nu^{\text{qs}}$  does not change

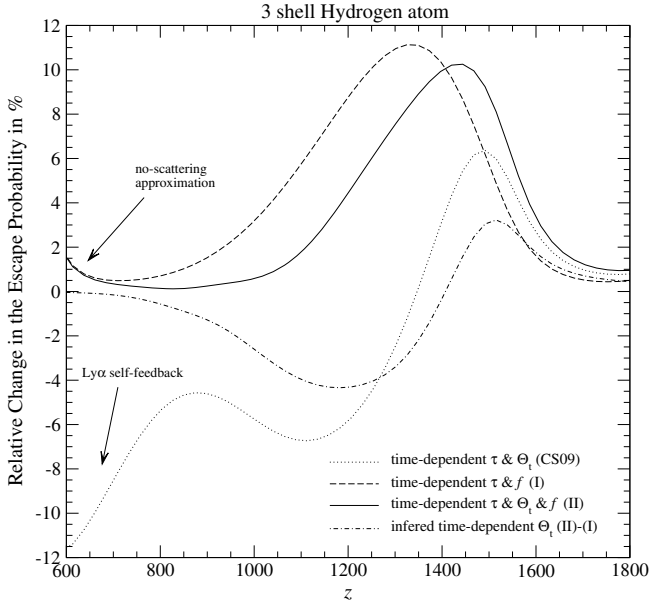


**Fig. 9.** Relative difference in the effective escape probability with respect to the Sobolev escape probability: effect of the thermodynamic correction factor.

when considering  $\mathcal{F}_v^t > \mathcal{F}_v^f > \mathcal{F}_v^{qs}$ , but  $\mathcal{F}_v^f$  becomes more similar to  $\mathcal{F}_v^t$ . From the behavior at  $-100 \lesssim x_D \lesssim -4$  and the strength of the changes there, one might have expected that at  $4 \leq x_D \leq 100$  also  $\mathcal{F}_v^t \geq \mathcal{F}_v^f$ , since  $|\Delta f_v/f_v|$  is similar in both regions. However, at  $4 \leq x_D \leq 100$  the spectral distortion  $F_v$  is very steep, so that small changes  $\Delta f_v/f_v$  cannot affect the shape of  $\mathcal{F}_v^f$  so much in comparison to  $F_v^t$ . Only at much larger distances on the blue side of the resonance, where  $f_v$  again behaves exponentially, can one see that  $\mathcal{F}_v^f \gg \mathcal{F}_v^t > \mathcal{F}_v^{qs}$ , although there  $F_v^t \gg F_v^f$  (compare with Fig. 6, right column, case  $z = 1000$ ). In comparison to the purely time-dependent correction for the range  $4 \leq x_D \leq 100$ , one therefore expects a slightly smaller (negative) correction to the total value of  $P$ , while the contributions from very large distances in the blue wing should be significantly larger than in the purely time-dependent case. However, here it is important to mention that these very distant wing contributions will always be very minor, since the Voigt profile decreases like  $\propto 1/x_D^2$  (see Sect. 5.1.3).

Finally, in the central region  $-4 \lesssim x_D \lesssim 4$ , we can see that  $\mathcal{F}_v^t \approx \mathcal{F}_v^f \approx \mathcal{F}_v^{qs}$ . This is because  $F_v^t \approx 1/f_v$  in these regions (see Sect. 4.1.1), so that  $\mathcal{F}_v^f \approx 1$  to very high accuracy. Although the Lyman  $\alpha$  spectral distortions in the case  $F_v^f$  and  $F_v^{qs}$  look rather different, this implies that a the correction factor  $f_v$  does not lead to any real correction in the escape probability from inside the Doppler core. Everything is well described by the quasi-stationary assumption, for which the entire Doppler core reaches thermodynamic equilibrium with the ambient radiation field, but now also including the small additional variation in the photon distribution over  $\nu$ .

### 5.1.2. Correction to the escape probability

In Fig. 9, we show the result for the effective escape probability and the effect of  $f_v$ . For comparison, we also show the result for the purely time-dependent correction (dotted line), which was already discussed elsewhere (Chluba & Sunyaev 2009c). At low redshifts, we indicate the increase in the amplitude of the correction, which was attributed to the late self feedback of Lyman  $\alpha$

photons for this case. For the other cases, we also point towards the difference caused by the no-scattering approximation. It is related to differences in  $P_d$  and  $P_s$ , which close to the maximum of the Thomson visibility function at  $z \sim 1100$  are negligible, but become significant both at very low and very high redshifts (Chluba & Sunyaev 2009c). However, the changes have no important effect on the free electron fraction.

When now including the thermodynamic correction factor in the computation of the absorption optical depth and the effective emission rate  $\Theta^a$ , but setting  $\Theta^t = 1$  (dashed line), one can see that the correction to the escape probability becomes positive at all redshifts, with a maximum of  $\Delta P/P \sim 11\%$  at  $z \sim 1350$ . As we see in Sects. 5.1.4 and 5.1.5, the bulk of this total correction originates from changes to the absorption process on the red side of the resonance, where in this case  $F_v \approx F_v^{qs} \approx 1$  (cf. Figs. 5 and 6, left column).

When also including the variation in  $\Theta^t \neq 1$  over time (solid line), the result changes significantly, shifting the maximum of the correction  $\Delta P/P \sim 10\%$  to  $z \sim 1450$ , but still leading to  $\Delta P/P > 0$  everywhere. However, especially the low redshift part is strongly modified, reducing the total correction by a factor of  $\sim 2$  at  $z \sim 1100$ . We also show the inferred correction related to  $\Theta^t$  alone, which was obtained by taking the difference between the curves labeled (I) and (II). The result shows that the final correction close to the maximum of the Thomson visibility function has important contributions from both  $f_v \neq 1$  and the time-dependence of the problem.

### 5.1.3. Effect at large distances blueward of the line center and the Lyman $\alpha$ self-feedback

The thermodynamic factor clearly strongly changes the behavior of the correction to the effective escape probability. The purely time-dependent correction is no longer dominant, and in particular the thermodynamic factor removes the *self feedback* problem of Lyman  $\alpha$  at low redshifts, which was already realized to be an artifact of the standard “1 + 1” photon formulation (Chluba & Sunyaev 2009c). This is because when taking  $f_v$  into account, exponentially fewer photons remain in the photon distribution at large distances on the blue side of the resonance (cf. Fig. 6 where  $F_v \sim 1/f_v$  at large  $x_D$ ). As explained in Sect. 3, every photon emitted at  $x_D \gg 1$  will be reabsorbed quasi-instantaneously. This is because of the exponentially larger amount of CMB photons redward of the Balmer  $\alpha$  line compared to close to the line center, so that line absorption is more effective. The main process for the death here is the  $1s \rightarrow 2p \rightarrow 3d$ , where the last step is considered to lead to a complete redistribution, so that the absorbed Lyman  $\alpha$  photon ( $1s \rightarrow 2p$ ) will most likely reappear close to the line center. We note that in this section we still do not include the two-photon corrections to the shape of the absorption profile, but already now the two-photon character of the process leads to this conclusion.

However, one has to mention that basically all the photons present at these large distances contribute to the escape integral. This is because  $\mathcal{F}_v^t \sim 1$  while  $\mathcal{F}_v^{qs} \ll 1$ , so that  $\mathcal{F}_v^t - \mathcal{F}_v^{qs} \sim 1$  (see Sect. 5.1.1 and Fig. 8). Therefore, in this case the very distant blue wing contribution to the value of  $\Delta P_{bw}^f$  behaves like

$$\frac{\Delta P_{bw}^f}{P_d} \approx - \int_{\nu_{bw}}^{\infty} \phi_\nu d\nu \approx - \frac{a}{\pi} \frac{\tau_d}{x_D^{bw}}, \quad (28)$$

at  $z \sim 1100$  implying an additional  $\leq 0.1\%$  correction from  $x_D^{bw} \geq 10^4$ , showing that the absolute contribution becomes negligible far beyond that point. In numerical computations, we therefore

typically integrated the profile up to  $x_D \sim 1.5 \times 10^4$ , introducing a very small error for cases with  $f_\nu \neq 1$  and practically no error when also including the correct shape of the emission profile, since then naturally very few photons appear at larger distances blueward of the resonance (e.g., see Fig. 8, solid line).

#### 5.1.4. Contributions from the blue and red wing

Returning to the correction at higher redshifts ( $z \gtrsim 800\text{--}900$ ), it was shown earlier, that there the Lyman  $\alpha$  self feedback is not important (Chluba & Sunyaev 2009c). From Fig. 9, it is clear that both considered cases for the effect of  $f_\nu$  imply that at a given redshift, effectively fewer photons support the flow of electrons towards higher levels and the continuum than in the quasi-stationary case, albeit that more photons are produced. The latter statement can also be confirmed by looking at Fig. 6 and the amplitude of the Lyman  $\alpha$  distortion in the distant red wing around its maximum. We note that these photons were already emitted at  $z \sim 1400$ .

However, from which part of the photon distribution do the main correction to the escape probability at these redshifts come from? Looking at Fig. 8, we can see that at  $0 \lesssim x_D \lesssim 100$ , the function  $\mathcal{F}_\nu^f$  is very similar to  $\mathcal{F}_\nu^t$ , which results in the purely time-dependent correction. Also at slightly larger distances ( $100 \lesssim x_D \lesssim 10^3$ ) one still has  $\mathcal{F}_\nu^f \sim \mathcal{F}_\nu^t$ . Therefore, one does not expect very dramatic changes to the contribution to the effective escape from this part of the Lyman  $\alpha$  distortion compared to the purely time-dependent case.

On the other hand, in the red wing one finds that  $\mathcal{F}_\nu^f \lesssim \mathcal{F}_\nu^t$ , and at very large distances one even has  $\mathcal{F}_\nu^f \ll \mathcal{F}_\nu^t$ . Physically, this reflects that due to  $f_\nu$ , the reabsorption process in the distant red wing is exponentially suppressed, so that photons can escape more directly than in the normal “1 + 1” photon formulation. This is now related to the exponentially smaller amount of CMB photons blueward of the Balmer  $\alpha$  line, so that the main absorption channel  $1s \rightarrow 2p \rightarrow 3d$  becomes practically inactive at  $x_D \lesssim -10^3$ . Therefore, it is the modifications to the red wing absorption process from which one expects the largest effect in connection with  $f_\nu$  at high redshifts, before the appearance of the self feedback problem.

Numerically, we studied this statement by simply assuming that at  $x_D \leq 0$ , the solution is given by the quasi-stationary result (implying  $\mathcal{F}_\nu^f \equiv \mathcal{F}_\nu^{qs} \approx 1$ ), while at  $0 \leq x_D$  we used the real solution for  $\mathcal{F}_\nu$  in the considered case. In this way, it is possible to separate the “blue wing” contribution to the total correction in the effective escape probability, and similarly one can obtain the “red wing” contribution. In Fig. 10, we show the comparison of these computations for the cases  $\Theta^t = 1$  and  $\Theta^\phi = 0$  (upper panel); only the corrections to  $\tau$  are included and  $\Theta^a = 1/f_\nu$ , and  $\Theta^t \neq 1$  and  $\Theta^\phi = 0$  (lower panel;  $\Theta^a = \Theta^t/f_\nu$ ). For comparison, we also show the results obtained for the purely time-dependent correction in the considered cases (cf. Chluba & Sunyaev 2009c).

In the first case (upper panel), one can clearly see that the blue wing contribution from  $\mathcal{F}_\nu^f$  is very close to the purely time-dependent result (dotted curve), which itself has no significant contribution from the red wing in the first place (diamonds). This shows that for this case the effect of  $f_\nu$  is not important at  $x_D \geq 0$ . One can see that the main correction due to the effect of  $f_\nu$  arises from the red wing, and that this correction is significantly larger than the time-dependent case alone.

If we look at the comparison in the fully time-dependent case (lower panel), one can see that when including the correction factor  $f_\nu$ , at high redshifts the blue wing contribution (dashed

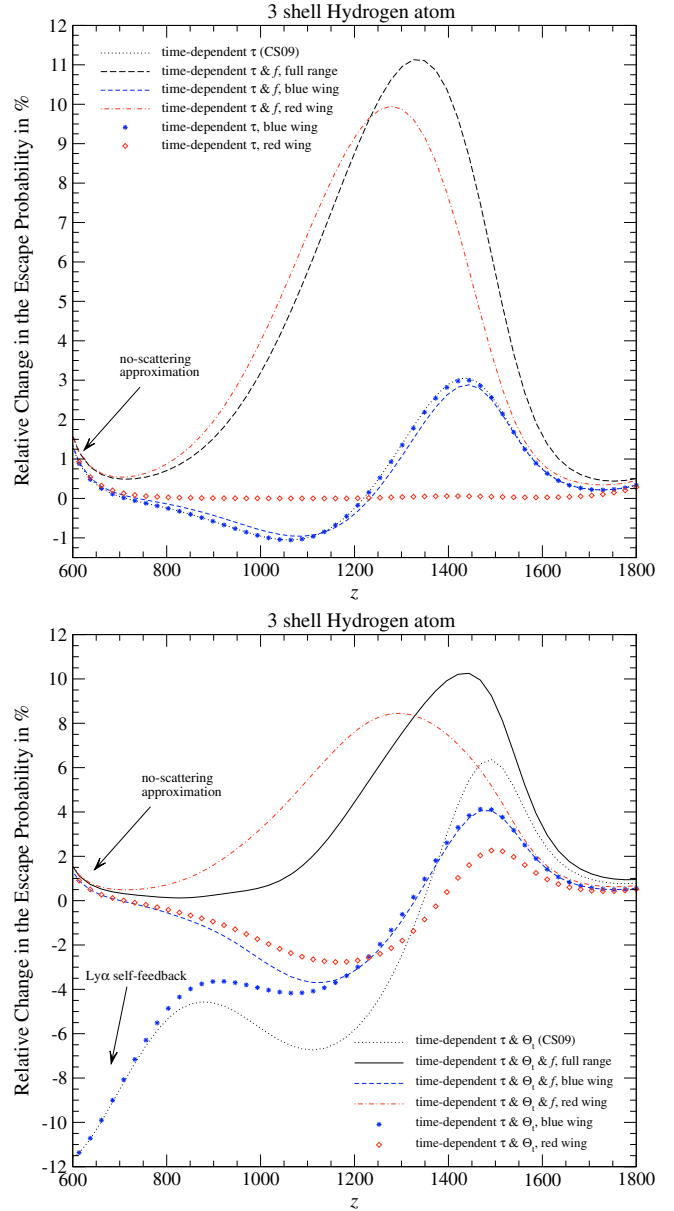


**Fig. 10.** Difference between the effective escape probability and the Sobolev escape probability: the effect of the thermodynamic correction factor in the blue and red wing of the resonance. For the upper panel, we set  $\Theta^t = 1$  and  $\Theta^\phi = 0$ . The lower panel was computed by also including  $\Theta^t \neq 1$ .

curve) is about 50% of the total result presented in Chluba & Sunyaev (2009c). At high redshifts, the blue-wing contribution in the purely time-dependent case (stars) practically coincides with the one that includes  $f_\nu$ , implying again that the blue wing contribution is not affected much by the thermodynamic correction factor. However, one can see that at low redshifts,  $f_\nu$  is very important for avoiding the self feedback problem, as explained in Sect. 5.1.3. We note that, in contrast to the curve quoted “ $\Delta P^t$  (only blue)” in Fig. 8 of Chluba & Sunyaev (2009c), the blue wing contribution here takes into account the time-dependent correction to  $\tau$  and  $\Theta^t$  simultaneously.

Looking at the red wing contributions for this case, one can see that for  $f_\nu = 1$  (diamonds) the contribution is now non-zero. This was also already seen earlier (Chluba & Sunyaev 2009c) and is because  $F_\nu^t \neq 1$ . However, the contribution from the red wing is much larger when including  $f_\nu \neq 1$ , and in particular

it is only positive because  $\mathcal{F}_\nu^f \lesssim 1$  at all frequencies, so that  $\Delta P > 0$ . The conclusion clearly is that the dominant correction related to the inclusion of  $f_\nu$  originates in the red wing of the Lyman  $\alpha$  resonance.

### 5.1.5. Simple estimate for the red wing correction

We can also perform another rough estimate of the expected correction, by assuming that in the red wing  $\mathcal{F}_\nu^f \sim f_\nu$ , as suggested by Fig. 8. This overestimates the result, since with the inclusion of  $f_\nu$  alone one already obtains  $\mathcal{F}_\nu^f \gtrsim f_\nu$ . In comparison with the quasi-stationary case ( $\mathcal{F}_\nu^{\text{qs}} \approx 1$ ), we then have that

$$\frac{\Delta P_{\text{rw}}^f}{P_d} \approx -\tau_d \int_0^{\nu_{\text{core}}} [f_\nu - 1] \phi_\nu d\nu \approx \tau_d \frac{a}{\pi} \int_{-\infty}^{-4} \frac{1 - e^{\frac{h\nu_D}{kT_\gamma} x_D}}{x_D^2} dx_D. \quad (29)$$

Since  $\frac{h\nu_D}{kT_\gamma} \sim 10^{-3} \left[ \frac{1+z}{1100} \right]^{-1/2} \ll 1$ , one can show that

$$\frac{\Delta P_{\text{rw}}^f}{P_d} \approx 1.6 \times 10^{-6} \tau_d \left[ \frac{1+z}{1100} \right]^{-1}. \quad (30)$$

At redshift  $z \sim 1100$ , one has  $\tau_d \sim 6.8 \times 10^4$ , so that only from the red wing correction one expects  $\frac{\Delta P_{\text{rw}}^f}{P_d} \sim 11\%$ , while at redshift  $z \sim 1350$  one finds  $\frac{\Delta P_{\text{rw}}^f}{P_d} \sim 16\%$ . The upper panel of Fig. 10 shows that this is the right order of magnitude, although the final correction is about 1.5 times smaller than given by this simple estimate.

### 5.1.6. Dependence on the distance to the line center

We finally consider the dependence of the correction on the distance to the line center. For this, we computed the results including the deviation for the quasi-stationary case in a given range around the line center. The results of these computations are shown in Fig. 11. Clearly a large fraction of the total correction originates in large distances ( $10 \lesssim |x_D| \lesssim 100-1000$ ) from the line center, while the contributions from within the Doppler core ( $|x_D| \lesssim 4$ ) are very small. The latter result again reflects that  $f_\nu$  does not deviate strongly from unity, nor does any time-dependent effect become important. The Doppler core can be considered to be quasi-stationary (for a more complete explanation see Chluba & Sunyaev 2009c) and in full equilibrium with the line center value.

## 5.2. Dependence on the shape of the absorption profile

As an additional step, we wish to understand how the two-photon corrections to the shape of the effective line profile affect the escape probability. For this we completed computations only taking into account that  $\phi_{\text{abs}}^* \neq \phi_\nu$ , but neglecting for the moment the corrections related to  $f_\nu$  and also assuming that  $\phi_{\text{abs}}^* = \phi_{\text{em}}$  inside  $\Theta^{\text{a}}$ . As explained in Sect. 4.3, the latter correction for our purpose is negligible during cosmological recombination, but the inclusion of  $f_\nu \neq 1$  is still expected to be very important, as we discuss in Sect. 5.3 for the combined effect.

### 5.2.1. Correction due to $\Delta P_{\text{ind}}$

Looking at Eq. (12c), it is clear that the contribution  $\Delta P_{\text{ind}}$  to  $P_{\text{eff}}$  is purely due to induced effects, since inside a vacuum one would find  $\Delta \bar{\varphi}_{\text{em}} \equiv \Delta \bar{\varphi}_{\text{abs}}^* = 0$ , and hence  $\Delta P_{\text{ind}} \equiv 0$ . In Fig. 12, we present the deviation in the normalization of the emission and

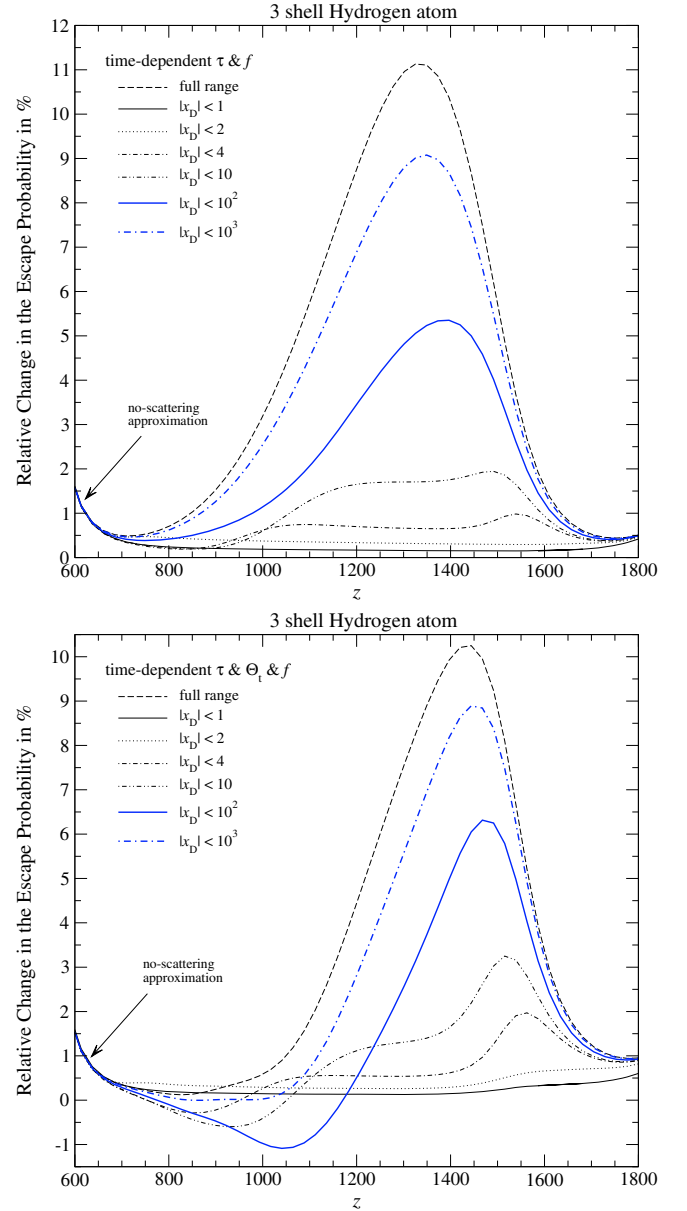


**Fig. 11.** Relative difference in the effective escape probability with respect to the Sobolev escape probability: effect of the thermodynamic correction factor at different distances to the line center. For the upper panel we set  $\Theta^t = 1$  and  $\Theta^\phi = 0$ . The lower panel was computed also including  $\Theta^t \neq 1$ .

absorption profile from unity, which have been computed using Eqs. (6) and (5a). First, one can see that at basically all redshifts of interest in the recombination problem,  $\Delta \bar{\varphi}_{\text{em}} \approx \Delta \bar{\varphi}_{\text{abs}}^*$ , implying that  $\Delta P_{\text{ind}} \approx \Delta \bar{\varphi}_{\text{em}}$ . Since  $\Delta \bar{\varphi}_{\text{em}} \lesssim 6 \times 10^{-9}$  at all shown redshifts, comparing  $\Delta P_{\text{ind}}$  with  $P_d$  implies that the associated correction  $\Delta P_S$  should never exceed the level of 0.1%. In a more detailed computation, we find a maximal correction of  $\Delta P_S/P_S \sim 0.06\%$  at  $z \sim 1300$ . In addition, this correction is practically canceled by another contribution,  $\Delta P_{\text{ind, norm}} = -\Delta \bar{\varphi}_{\text{abs}}^*$ , which appears as a result of stimulated emission on the overall normalization of the effective absorption profile (see Sect. 5.2.2). We can therefore neglect this term in the following.

We mention that the main contribution to  $\bar{\varphi}_{\text{em}} \neq 1$  originates in the region  $\nu \sim \nu_{31}$ . This can be seen in Fig. 2, where only in that region the effective two-photon emission profile

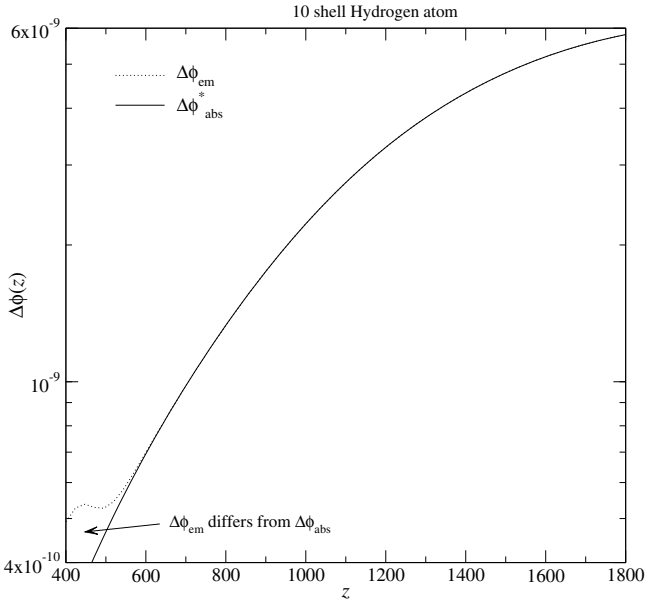


**Fig. 12.** Deviation of the normalization of the different line-profiles from unity. The effect of stimulated emission in the ambient CMB blackbody radiation field was included.

differs significantly from the vacuum profile,  $\varphi_{\text{em,vac}}^*$ . At this large distance from the line center, the overall profile already dropped by a factor of  $10^{11}$ – $10^{12}$  relative to the line center (the value there is  $\sim 1/\sqrt{\pi} \sim 0.56$ ). From Fig. 2, one can see that  $\varphi_{\text{em}}^* - \varphi_{\text{em,vac}}^* \sim 10^{-12}$  over a region  $\Delta x_D \sim 10^3$ , so that one expects that  $\Delta P_{\text{ind}} \sim 10^{-9}$  at  $z \sim 1300$ , which is in good agreement with the full numerical result.

### 5.2.2. Expression for $P_{\text{eff}}$ and its connection to $F_\nu$ .

To understand the corrections to the effective escape probability and its relation to the differences in the spectral distortion, we again look at the definition of  $P$ , Eq. (10b), with  $f_\nu \equiv 1$  and rewrite it as

$$P^{l,\phi} = \int [\varphi_\nu - \varphi_{\text{abs}}^*] d\nu + \int \varphi_{\text{abs}}^* [1 - F_\nu^{l,\phi}] d\nu. \quad (31)$$

The first integral is given by

$$\begin{aligned} \Delta P_{\text{ind, norm}} &= \int [\varphi_\nu - \varphi_{\text{abs,vac}}^*] d\nu + \int [\varphi_{\text{abs,vac}}^* - \varphi_{\text{abs}}^*] d\nu \\ &= -\Delta \bar{\varphi}_{\text{abs}}^*. \end{aligned} \quad (32)$$

We note that  $\int [\varphi_\nu - \varphi_{\text{abs,vac}}^*] d\nu \equiv 0$ , even though the partial contributions from the red and blue wing are non-zero. As mentioned in Sect. 5.2.1,  $\Delta P_{\text{ind, norm}}$  cancels with the correction related to  $\Delta P_{\text{ind}}$ , so that we finally have

$$P_{\text{eff}}^{l,\phi} \approx \int \varphi_{\text{abs}}^* [1 - F_\nu^{l,\phi}] d\nu. \quad (33)$$

This expression now allows us to compute the correction to the escape probability.

To determine how the shape of the profile enters into the problem, it is illustrative to look at the result for  $P_{\text{eff}}^{l,\phi}$  when assuming quasi-stationary conditions, but including the correction

due to the profile. In this case, one has  $\tau_{\text{abs}}^{\phi, \text{qs}} = \tau_d(z) \int_\nu^\infty \varphi_{\text{abs}}^* d\nu'$  and with  $F_\nu^{\phi, \text{qs}}(\nu) \equiv 1 - e^{-\tau_{\text{abs}}^{\phi, \text{qs}}}$ , resulting from Eq. (15), one finds

$$P_{\text{eff}}^{\phi, \text{qs}} = \int \varphi_{\text{abs}}^* e^{-\tau_{\text{abs}}^{\phi, \text{qs}}} d\nu = \int_0^{\chi_{\text{a},\infty}^*} e^{-\tau_d[\chi_{\text{a},\infty}^* - \chi_{\text{a}}^*]} d\chi_{\text{a}}^* \approx P_d. \quad (34)$$

Here we have introduced the variable  $\chi_{\text{a}}^*(\nu) = \int_0^\nu \varphi_{\text{abs}}^* d\nu'$  and  $\chi_{\text{a},\infty}^* = \chi_{\text{a}}^*(\infty)$ . This expression shows that in the quasi-stationary case, the shape of the profile does not matter. The result will still be extremely close to  $P_d$ . This also implies that the shape of the profile only enters as correction to correction, i.e., combination of time-dependence and profile. Therefore, the changes due to the exact shape of the profile are expected to be smaller than the corrections due to  $f_\nu$  and the time-dependence alone. As we see below, they are still not negligible, in particular when taking all corrections into account simultaneously (Sect. 5.3).

For the correction to the effective escape probability, we can therefore finally write

$$\Delta P_d^{l,\phi} = P_{\text{eff}}^{l,\phi} - P_d \approx - \int \varphi_{\text{abs}}^* [F_\nu^{l,\phi} - F_\nu^{\phi, \text{qs}}] d\nu. \quad (35)$$

It is now clear that for the contributions of the total correction, it is important how  $F_\nu^{l,\phi}$  deviates from  $F_\nu^{\phi, \text{qs}}$ . For  $F_\nu^{l,\phi} < F_\nu^{\phi, \text{qs}}$ , one will have a *positive* contribution and for  $F_\nu^{l,\phi} > F_\nu^{\phi, \text{qs}}$  a *negative*. In addition, because of the appearance of  $\phi_{\text{abs}}^*$  in the outer integral, the red wing contribution ( $\phi_{\text{abs}}^* \gtrsim \phi_\nu$ ) will be slightly *overweighted*, while the blue wing ( $\phi_{\text{abs}}^* \lesssim \phi_\nu$ ) will be *underweighted*.

We note that  $F_\nu^{\phi, \text{qs}}(\nu)$  behaves very similarly to  $F_\nu^{\text{qs}}(\nu)$ . In particular, at frequencies  $x_D \lesssim 4$  it also becomes very close to unity, so that  $F_\nu^{\phi, \text{qs}}(\nu) \approx F_\nu^{\text{qs}}(\nu)$ . The main difference appears in the blue wing of the line, where  $F_\nu^{\phi, \text{qs}}(\nu)$  depends strongly on the differences between  $\phi_{\text{abs}}^*$  and  $\phi_\nu$ . Both aspects can be seen in the right panel of Fig. 8.

### 5.2.3. Total corrections and the blue and red wing contributions

In Fig. 13, we show the results for the total correction to the effective escape probability when including the modifications to the shape of the absorption profile. We used the expression Eq. (33) to compute the different curves. Again for comparison, we also provide the results for the time-dependent corrections only. As one can see the main effect of the profile is the removal of the self feedback at low redshift. Other than that in the considered cases, the modifications, compared to those for the time-dependent result, are rather small (less than  $\sim 10\%$  of  $\Delta P/P$  for the cases with  $\Theta^l = 1$ , and less than  $\sim 1\%$  of  $\Delta P/P$  for those with  $\Theta^l \neq 1$ ).

This shows that there is a cancellation between the corrections from the red and the blue wing, since it is clear already that the modulation of these partial contributions due to the presence of  $\phi_{\text{abs}}^*$  in the outer integral of Eq. (33) should have some effect, even if it is of higher order in the correction. To understand the results, we therefore look at the differential contribution from the red and blue wing separately. For Fig. 14, we ran computations including the corrections to the quasi-stationary result either on the red or blue side of the resonance. We compare the total and partial corrections in both the purely time-dependent case and when also including the shape of the absorption profile.

<sup>13</sup> There is a tiny difference because  $\chi_{\text{a},\infty}^* \gtrsim \chi_\infty$ .

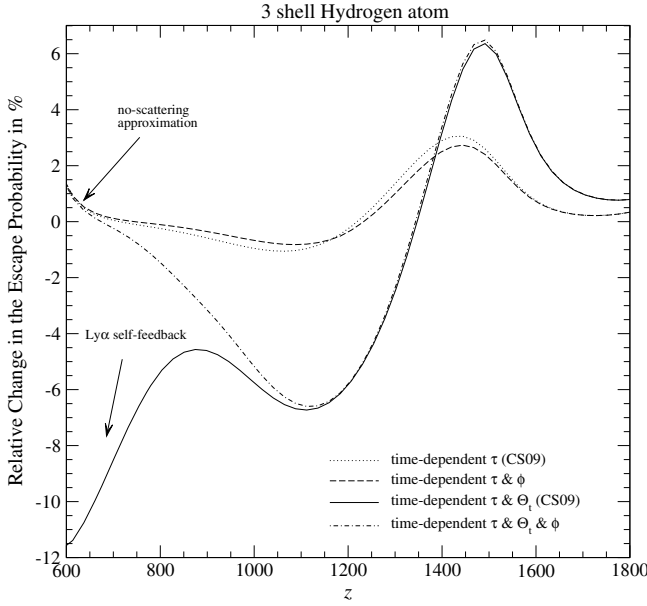


**Fig. 13.** Relative difference in the effective escape probability with respect to the Sobolev escape probability: effect of the line profile. For the curves labeled with “CS09” (Chluba & Sunyaev 2009c) we used the standard Voigt profile, while for the others we included the two-photon corrections for the 3s and 3d channels.

#### Corrections in the case of $\Theta^t = 1$

When only including the profile corrections to  $\tau_{\text{abs}}$  (upper panel,  $\Theta^t = 1$  and  $\Theta^\phi = 0$ ), we can see that the effect of  $\phi_{\text{abs}}^*$  does not lead to any important correction from the red wing. Looking at Figs. 5 and 6 (left column), it is clear that in there  $F_v^{t,\phi} \approx F_v^{\text{qs}} \approx 1$ . Since also  $F_v^{\text{qs}} \approx F_v^{\phi,\text{qs}}$  (see Sect. 5.2.2), one has  $F_v^{t,\phi} - F_v^{\phi,\text{qs}} \approx 0$  and hence with Eq. (35) one expects a partial contribution of  $\Delta P_d^{t,\phi} \approx 0$ , confirming the above behavior. The small positive bump seen at  $z \sim 1400$  is caused mainly by us starting our computation of the spectral distortion at some particular time in the past ( $z_s = 2000$ ), so that in the considered case the numerical solution for the spectral distortion, as computed using Eq. (8b), drops towards zero below some distance  $x_D \lesssim -10^4$  instead of staying close to unity. Therefore, we have  $F_v^{t,\phi} - F_v^{\phi,\text{qs}} \approx -1$  and hence  $\Delta P_d^\phi(x_D < -10^4) \approx \int \phi_{\text{abs}}^* dx_D \sim \text{few} \times 10^{-3}$  from that region, explaining this small excess with respect to  $P_d$ . We also checked this statement numerically by increasing  $z_s$  as expected finding that the bump became smaller. When also including the time-dependence of the emission coefficient ( $\Theta^t \neq 1$ ), this small inconsistency in our computation is no longer important, since the spectral distortion by itself drops very rapidly toward zero (cf. Figs. 5 and 6, right column).

Again looking at the upper panel in Fig. 14, we can also see that the largest contribution to the total correction originates in the blue wing, and that the difference to the time-dependent case is rather small, with  $\Delta P_d^{t,\phi}$  being slightly smaller. This can be understood when writing  $\tau_{\text{abs}}^{t,\phi} = \tau_{\text{abs}}^{\phi,\text{qs}} + \Delta\tau^{t,\phi}$ , where

$$\begin{aligned} \Delta\tau^{t,\phi} &\approx \int_v^\infty \Delta\tau_d(z') \varphi_{\text{abs}}^*(v', z') dv' \\ &= \int_v^\infty \Delta\tau_d(z') \varphi_V(v', z) dv' + \int_v^\infty \Delta\tau_d(z') \Delta\varphi_{\text{abs}}^*(v', z') dv', \end{aligned} \quad (36)$$

with the abbreviations  $1 + z' = \frac{v'}{v}(1 + z)$ ,  $\Delta\tau_d(z') = \tau_d(z') - \tau_d(z)$ , and  $\Delta\varphi_{\text{abs}}^*(v', z') = \varphi_{\text{abs}}^*(v', z') - \varphi_V(v', z)$ . This approximation

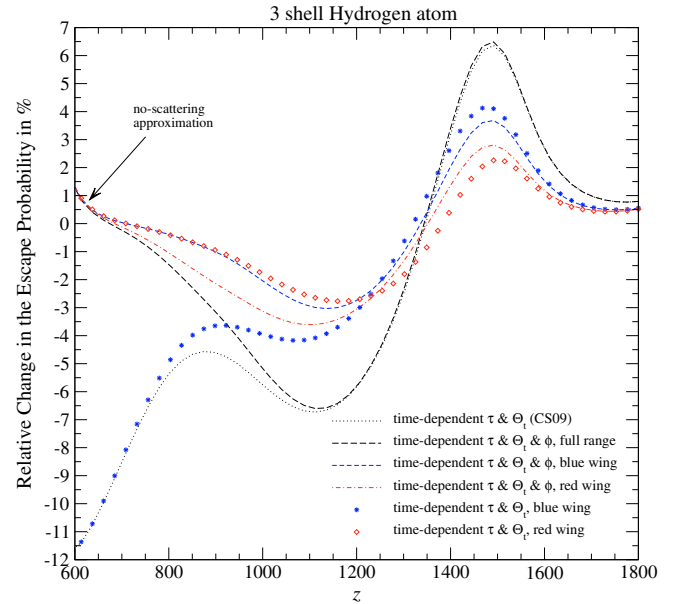
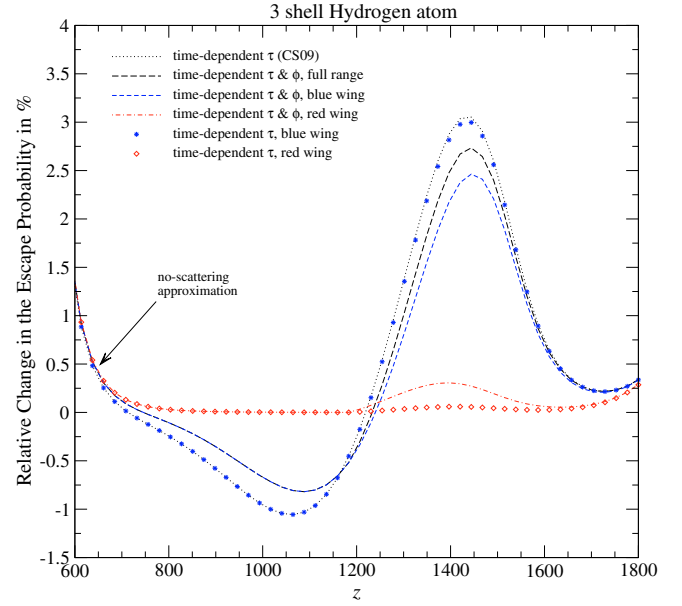


**Fig. 14.** Relative difference in the effective escape probability with respect to the Sobolev escape probability: correction due to the shape of the absorption profile in the blue and red wing of the resonance. For the upper panel we set  $\Theta^t = 1$  and  $\Theta^\phi = 0$ . The lower panel was computed also including  $\Theta^t \neq 1$ . In all cases we used  $f_i = 1$ . Those curves labeled with  $\phi$  were computed including the 3s and 3d two-photon corrections.

shows that one has  $\Delta\tau^{t,\phi} \approx \int_v^\infty \Delta\tau_d(z') \varphi_V(v', z) dv' \equiv \Delta\tau^t$ , since the profile correction with respect to  $\tau_{\text{abs}}^{\phi,\text{qs}}$  is already of higher order. For  $\Theta^a = 1$ , one therefore expects

$$\begin{aligned} \Delta P_d^{t,\phi} &\approx \int \varphi_{\text{abs}}^* e^{-\tau_{\text{abs}}^{\phi,\text{qs}}} [e^{-\Delta\tau^{t,\phi}} - 1] dv \\ &\approx \int \varphi_V e^{-\tau_d^{\text{qs}}} [e^{-\Delta\tau^t} - 1] dv = \Delta P_d^t, \end{aligned} \quad (37)$$

confirming the result seen in Fig. 14 to lowest order.

The remaining difference is due mainly to the second order term in Eq. (36)  $\Delta\tau^{t,\phi} - \Delta\tau^t = \int_v^\infty \Delta\tau_d(z') \Delta\varphi_{\text{abs}}^*(v', z') dv'$ , which we neglected in Eq. (37). The factor  $\varphi_{\text{abs}}^* e^{-\tau_{\text{abs}}^{\phi,\text{qs}}}$  plays a minor role, since the function  $e^{-\Delta\tau^{t,\phi}} - 1$  varies far more rapidly. We

confirmed these statements numerically, finding that for the considered case the modulation of the blue wing correction due to  $\phi_{\text{abs}}^*$  in the outer integral can be neglected.

### Corrections in the case of $\Theta^t \neq 1$

To understand the result when also including the change to the effective emission coefficient  $\Theta^t \neq 1$ , we again look at the red and blue wing contribution separately. Since in the red wing  $F_{\nu}^{\phi, \text{qs}} \approx 1$  and because we already saw in Sect. 4.2 that the solution for the spectral distortion is dominated by the correction due to  $\Theta^t \neq 1$  only (cf. Figs. 5 and 6 right column), we expect that the partial contribution from the red wing will be very close to

$$\Delta P_{\text{rw}}^{\phi} \approx \int \phi_{\text{abs}}^* [1 - F_{\nu}^t] d\nu, \quad (38)$$

where  $F_{\nu}^t$  is the spectral distortion for the purely time-dependent case. Therefore to lowest order again one will have  $\Delta P_{\text{rw}}^{\phi} \approx \Delta P_{\text{rw}}^t$ , but in next order this correction will in addition be slightly larger in amplitude because for  $x_{\text{D}} \leq 0$  one has  $\phi_{\text{abs}}^* \gtrsim \phi_{\nu}$ . We can see that this is true by comparing the diamonds with the dash-dotted curve in the lower panel of Fig. 14.

For the blue wing, one can argue in a very similar way as above. We know that for  $\Theta^t = 1$  the correction to the escape probability is basically given by the time-dependent correction to the value of  $\tau_{\text{abs}}$ , but only to higher order because  $\phi_{\text{abs}}^* \neq \phi_{\nu}$ . If now including  $\Theta^t \neq 1$ , the lowest order correction will still be given by the purely time-dependent case. The additional modulation of the resulting spectral distortion by  $\phi_{\text{abs}}^* \lesssim \phi_{\nu}$  will in addition lead to a small decrease in the total amplitude of the contribution to the correction. This can again be seen in Fig. 14 when comparing the stars with the short-dashed curve. Only at low redshifts does the shape of the profile determine the amplitude of the correction, removing the self-feedback problem. This is because unlike in the case of  $\phi_{\nu}$ , photons are only emitted in a limited range of frequencies. This avoids photons released at  $z \sim 1400$  and  $x_{\text{D}} \gg 10^4$  being redshifted into the Lyman  $\alpha$  line at  $z \lesssim 1000$ , as seen in the normal “1 + 1” formulation of the problem (Chluba & Sunyaev 2009c).

Furthermore, it is clear that the sum of both the red and blue wing contribution should again be close to the purely time-dependent case, since the modulation of the contributions from the red (enhancement) and blue wing (suppression) in lowest order will cancel, due to the symmetry around the line center.

### 5.3. Combined effect of $f_{\nu}$ and $\phi_{\text{abs}}^* \neq \phi_{\nu}$

With the derivations in the previous sections, it is now straightforward to understand the results for the combined effect of all corrections. Following the same line of thoughts we obtain

$$\Delta P_{\text{d}}^a = - \int \phi_{\text{abs}}^* [f_{\nu} F_{\nu}^a - F_{\nu}^{\phi, \text{qs}}] d\nu. \quad (39)$$

where in  $F_{\nu}^a$  we include all the corrections simultaneously.

As in the previous section, it is now clear that on the red side of the resonance the profile will enter the computation mainly because of its presence in the outer integral. For  $F_{\nu}^a$  and  $x_{\text{D}} \leq 0$ , it only leads to a very small correction (cf. Figs. 5 and 6 right column). However, on the blue side of the resonance the profile correction can again be neglected in the outer integral, but should be taken into account when computing the difference  $\Delta_{\nu} = f_{\nu} F_{\nu}^a - F_{\nu}^{\phi, \text{qs}}$ . One can also conclude that the shape of

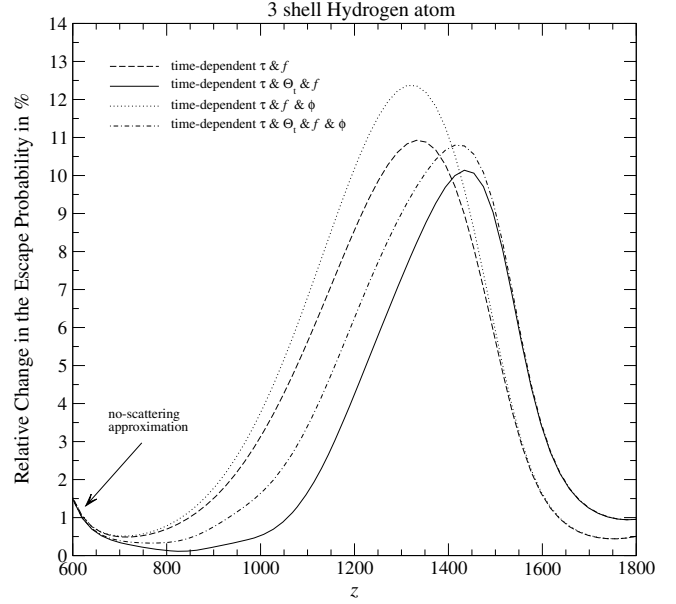


**Fig. 15.** Relative difference in the effective escape probability with respect to the Sobolev escape probability: combined effect of the thermodynamic correction factor and the shape of the line profile.

the profile plays a key role in removing the low redshift self-feedback problem. The latter statement can be confirmed when looking at the shape of the Lyman  $\alpha$  distortion at intermediate to high frequencies blueward of the resonance (cf. Figs. 5 and 6 right column), which is clearly dominated by the profile rather than  $f_{\nu}$ .

Therefore, to lowest order one expects the total correction to be the superposition of the time-dependent correction and the one from the thermodynamic correction factor, where on the red side of the resonance each of them is also modulated by the profile shape in the outer integral of Eq. (39), while on the blue side the contribution is slightly suppressed because of the profile corrections to  $\Delta_{\nu}$ . Here it is important that because  $f_{\nu}$  strongly changes the symmetry of the problem (the main correction originates in the red wing as shown in Sect. 5.1), it is clear that the main effect of  $\phi_{\text{abs}}^* \neq \phi_{\nu}$  will be an enhancement of the final correction.

In Fig. 15, we present the results from our numerical calculation for different cases. We find that when including the shape of the profile the corresponding correction is slightly increased as explained above.

#### 5.3.1. Dependence on the included number of shells

For the purely time-dependent correction, it has been shown that at low redshifts in particular the result depends strongly on the total number of shells that are included in the computation. Since the correction is strongly dominated by the self-feedback of Lyman  $\alpha$  photons, we do expect this dependence on the number of shells to be more mild.

In Fig. 16, we show the results of our computations for 3, 5, and 10 shells. The changes between the 3 and 5-shell cases is still rather significant, but the difference between the 5 and 10-shell case is already very minor. This shows that in our description the total correction has already converged when including  $\sim 5$  shells into the computation.

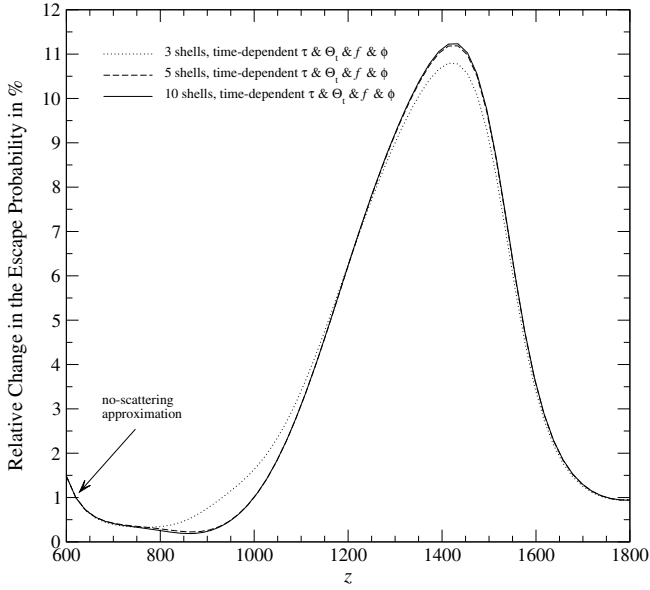


**Fig. 16.** Total relative difference in the effective escape probability with respect to the Sobolev escape probability: dependence on the total number of shells. Note that the curves for the 5-shell and 10-shell cases practically coincide.

## 6. Effect on the ionization history and the CMB power spectra

We now determine the expected correction to the ionization history when including the processes discussed in this paper. For this, we modified the RECFAST code (Seager et al. 1999), so that we can load the precomputed change to the Sobolev escape probability studied here.

In Fig. 17, we present the final curves for  $\Delta P/P$  as obtained for the different processes discussed in this paper. In Fig. 18, we show the corresponding correction to the free electron fraction computed with the modified version of RECFAST. One can clearly see that the dominant correction is due to the thermodynamic factor, resulting in  $\Delta P/P \sim +10\%$  at  $z \sim 1280$  and  $\Delta N_e/N_e \sim -1.9\%$  at  $z \sim 1120$ . The next largest correction is related to the time-dependent aspects of the problem, leading to  $\Delta P/P \sim -5.6\%$  at  $z \sim 1120$  and  $\Delta P/P \sim +5.9\%$  at  $z \sim 1490$ . The associated correction to the free electron fraction has a maximum of  $\Delta N_e/N_e \sim +1.2\%$  at  $z \sim 1020$ . The smallest correction is due to the exact shape of the effective line profile, resulting in  $\Delta P/P \sim +2.0\%$  at  $z \sim 1200$  and  $\Delta N_e/N_e \sim -0.4\%$  at  $z \sim 1080$ . The total correction then is  $\Delta P/P \sim +11\%$  at  $z \sim 1420$  and  $\Delta N_e/N_e \sim -1.6\%$  at  $z \sim 1190$ . This represents an important acceleration of hydrogen recombination, although at  $z \sim 1100$ , a large part of the correction due to  $f_\nu$  alone is canceled by the time-dependent correction. At the maximum of the Thomson visibility function at  $z \sim 1100$ , we find that  $\Delta N_e/N_e \sim -1.3\%$ , where about  $\Delta N_e/N_e \sim -0.4\%$  is coming from the shape of the profile alone.

For completeness, we also show the correction due to the two-photon formulation alone, i.e., after subtracting the time-dependent contribution from the total correction. It leads to  $\Delta N_e/N_e \sim -2.4\%$  at  $z \sim 1110$ .

In Fig. 19, we finally show the changes in the CMB temperature and polarization power spectra coming from the total correction  $\Delta N_e/N_e$  as given by the solid line in Fig. 18. In particular the changes in the EE power spectrum are impressive, with a peak-to-peak amplitude of  $\sim 2-3\%$  at  $l \gtrsim 1500$ . One can also see

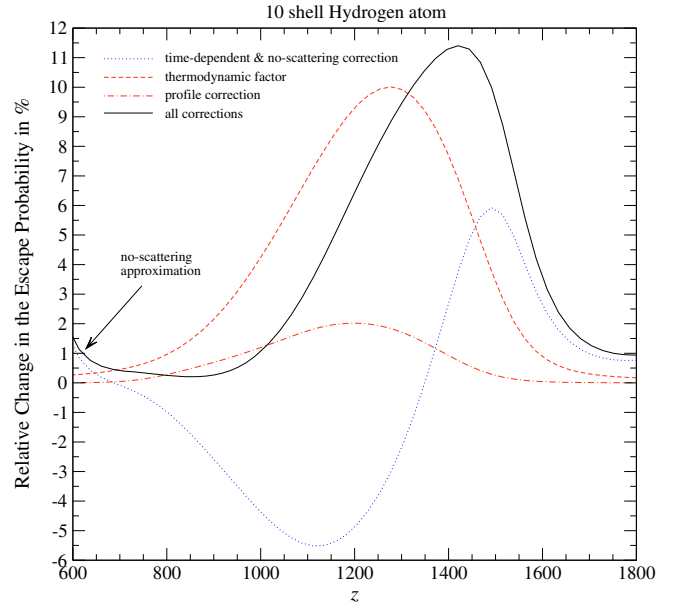


**Fig. 17.** Relative difference in the effective escape probability with respect to the Sobolev escape probability: separate contributions due to the time-dependent correction, the thermodynamic factor and the shape of the profile.

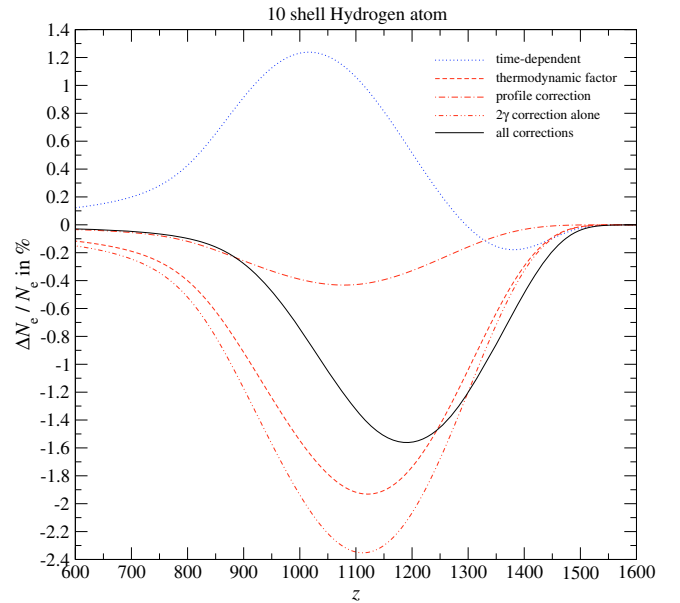


**Fig. 18.** Changes in the free electron fraction: separate contributions due to the time-dependent correction, the thermodynamic factor and the shape of the profile.

that the modifications to the  $C_l$ 's correspond more to a shift in the positions of the peaks rather than changes in the absolute amplitude. This is because the correction in the free electron fraction leads to a small shift in the maximum of the Thomson visibility, but does not affect the Silk damping length (Silk 1968) as much. It will be very important to take these changes into account in the analysis of future CMB data.

## 7. Discussion and conclusions

We have presented a formulation of the Lyman  $\alpha$  transfer equation, which allows us to include the two-photon corrections for

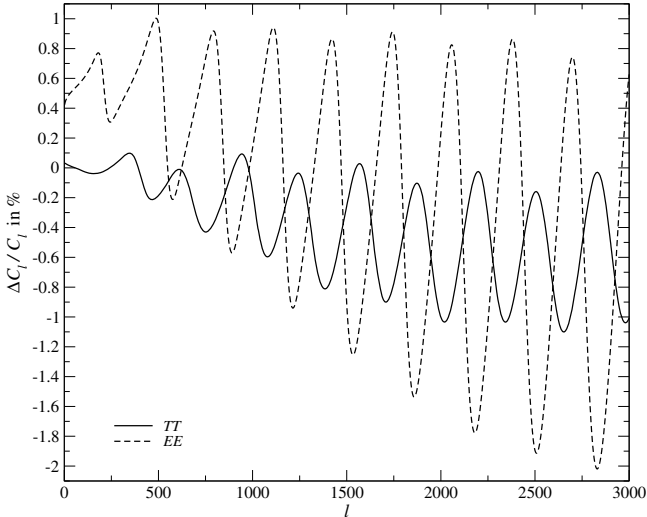


**Fig. 19.** Changes in the CMB temperature and polarization power spectra. We included effect of the time-dependent correction, the thermodynamic correction factor and the profile correction, simultaneously. We used the result for the 10-shell hydrogen atom.

the 3s-1s and 3d-1s channels. We then solved this transfer equation and presented the results for the Lyman  $\alpha$  distortion at different redshifts (Sect. 4). From this we computed the effective Lyman  $\alpha$  escape probability and derived the corresponding corrections to the Sobolev escape probability (Sect. 5). We used these results to compute the corrections to the free electron fraction during hydrogen recombination, and the associated changes to the CMB power spectra (Sect. 6). Below we briefly summarize the results of each section and also provide a short discussion of future work and improvements.

### 7.1. The resulting Lyman $\alpha$ spectral distortion

In Sect. 4, we discussed the influence of the different processes on the Lyman  $\alpha$  distortion at different redshifts. Including all the corrections considered here simultaneously, one can conclude that at  $x_D \lesssim 0$  the shape of the distortion is determined mainly by the time-dependence of the effective emission rate (cf. Figs. 5 and 6, right column). In the close vicinity of the resonance, *all* sources of corrections under discussion here are important to the exact shape of the Lyman  $\alpha$  spectral distortion at different redshifts (cf. Fig. 4). In particular, inside the Doppler core the spectral distortion will be very close to the value at the line center multiplied by  $1/f_\nu$ . On the blue wing, the distortion is mainly determined by the shape of the line profile.

With the method given here, we can in principle also compute the Lyman  $\alpha$  distortion, as it would be observable today. Since all the processes discussed here affect the precise shape of this distortion, one could in principle probe our understanding of the recombination dynamics by observing it. As mentioned earlier (Chluba & Sunyaev 2009c), one similarly expects additional changes to the detailed shape of the Lyman  $\alpha$  distortion because of partial frequency redistribution and electron scattering. All of these processes therefore not only affect the dynamics of cosmological hydrogen recombination, but in principle should leave observable traces in cosmological recombination spectrum (e.g., see Sunyaev & Chluba 2007, and references therein) until today. Measuring the exact shape of the Lyman  $\alpha$  distortion and the other recombinational lines would in principle allow us to reveal these differences, and therefore

directly probe our understanding of the recombination problem. Also if something non-standard happens (e.g., due to early energy release by decaying or annihilating dark matter), this will affect the exact shape of the cosmological recombination radiation (Chluba & Sunyaev 2009b). Therefore, by observing the recombinational radiation one in principle can directly uncover potential unknowns in the cosmological recombination problem, a task that may not be otherwise completed.

### 7.2. Corrections to the escape probability

We have discussed the corrections to the effective Lyman  $\alpha$  escape probability, showing that the largest contribution is from the thermodynamic factor  $f_\nu$  (see Fig. 17). The next largest correction is related to time-dependent aspects of the recombination problem, where in the formulation given here the self-feedback problem (Chluba & Sunyaev 2009c) appearing at low redshifts, disappears when using the “1 + 1” photon picture (cf. Fig. 17). Furthermore the time-dependent correction partially cancels the correction to the thermodynamic factor at low redshift ( $z \lesssim 1300$ –1400), leaving a significantly smaller change in the escape probability at  $z \sim 1100$ . As we explained here, these two corrections can also be obtained in the normal “1 + 1” photon picture, but for the thermodynamic correction factor a natural interpretation can only be given within the two-photon picture (see Sect. 2.1.1). Here the crucial ingredient is that the spectrum in the vicinity of the second, low frequency photon  $\gamma'$  is given by the CMB blackbody photon field, which then allows us to write the radiative transfer equation for the Lyman  $\alpha$  photon as an equation for one photon only. A very similar formulation should be applicable to expanding envelopes of planetary nebulae and stars, where the photon field in the vicinity of  $\gamma'$  will be given by a weakly diluted blackbody spectrum. However, when the photon distribution in the vicinity of *both* photons involved in the absorption process are far from their equilibrium values the derived formulation does not work.

We also showed that the correction coming from the exact shape of the line profile in the vicinity of the Lyman  $\alpha$  resonance leads to the smallest separate correction under discussion here. Only this part of the correction is really related to quantum mechanical modifications of the transfer problem. However, the final contribution related to this modification is significant at the required level of accuracy (cf. Fig. 17).

### 7.3. Implications for the ionization history and the CMB power spectra and critical remarks

The results for the changes in the free electron fraction and CMB power spectra are shown in Figs. 18 and 19, respectively. The main effect on  $N_e$  due to the processes discussed here is a net acceleration of hydrogen recombination by  $\Delta N_e/N_e \sim -1.3\%$  at  $z \sim 1100$ . About  $\Delta N_e/N_e \sim -0.4\%$  of this correction is from the shape of the line profile alone, while the rest is due to the thermodynamic factor and the time-dependent aspects of the recombination problem. Here we emphasize again, that the latter two corrections can also be obtained in the standard “1 + 1” photon picture, when introducing the thermodynamic correction factor using the detailed balance principle.

We also mention that our results for the changes in the free electron fraction seem to be rather similar to those of Hirata (2008) for the contributions from high level two-photon decays alone. However, we have obtained these results with a completely independent method. For the future, it will be very

important to perform a more detailed comparison once all relevant additions are identified.

Regarding the CMB power spectra, in particular the associated changes in the EE power spectrum are impressive, reaching peak-to-peak amplitude  $\sim 2\text{--}3\%$  at  $l \gtrsim 1500$  (see Fig. 19). It will be important to take these corrections into account for the analysis of future CMB data.

However, it is also clear that several steps still have to be taken: one still has to (i) study more processes; and (ii) develop a sufficiently fast method to simultaneously incorporate all the corrections discussed in the literature into the computations of the CMB power spectra, in preparation for true parameter estimations using the CMB data.

Regarding the first point, for example, the correction related to Raman processes (as explained in Hirata 2008, mostly due to 2s-1s Raman scattering) leads to an additional delay of recombination at low redshifts with a maximum of  $\Delta N_e/N_e \sim +0.94\%$  at  $z \sim 920$ . We did not include this process here, but it certainly is very important to accurate predictions of the CMB power spectra and should be cross-validated in the future. It is clear that one should also include the effect of higher level two-photon decays (e.g., from the 4d-level), since they are expected to also speed up hydrogen recombination, likely affecting the result obtained here by another  $\sim 10\text{--}20\%$  (i.e.,  $\Delta N_e/N_e \sim 0.1\text{--}0.3\%$ ). Finally, the effects of partial frequency redistribution, line recoil, and electron scattering should also be studied. In particular, the effect of line recoil will be important, leading to a systematic drift of photons towards lower frequencies again accelerating hydrogen recombination by  $\Delta N_e/N_e \sim -1.2\%$  at  $z \sim 900$  (Grachev & Dubrovich 2008; Chluba & Sunyaev 2009a).

Regarding the second point, Fendt et al. (2009) proposed a new approach called RICO<sup>14</sup>, which uses multi-dimensional polynomial regression to accurately represent the dependence of the free electron fraction on redshift and the cosmological parameters. Instead of running the full (slow) recombination code, one trains RICO with a set of models, so that the interpolation between them will be afterwards very fast. This approach should allow us to propagate all the corrections in the ionization history that are included in the full recombination code to the CMB power spectra, without using any fudging like in RECFAST (Seager et al. 1999; Wong et al. 2008). In the future, we plan to provide an updated training set for RICO, including the corrections discussed here. This should also make it easier for other groups to cross-validate our results and will allow us to focus our efforts on the physics rather than our approximations of it.

## Appendix A: Different channels for the emission and death of Lyman $\alpha$ photon involving a sequence of two transitions

If we restrict ourselves to the main channels that can lead to the emission or absorption of photons in the vicinity of the Lyman  $\alpha$  resonance and involve two photons then we are left with: (i)  $ns \rightarrow 1s$  two-photon decay and absorption; (ii)  $nd \rightarrow 1s$  two-photon decay and absorption; (iii)  $c \rightarrow 1s$  two-photon recombination and photoionization.

The problem is now to compute the emission and absorption profiles connected with these processes and describe their relative contributions or probabilities at a given frequency. This in principle can be done for all possible routes. However, here we focus on formulating the problem for the  $3s \rightarrow 1s$  and  $3d \rightarrow 1s$

two-photon channels, not altering all other channels. This is a reasonable first approximation, since as we show here it is already clear from the “1 + 1” photon picture that the main contribution to the death of photons is from the 3d channel (see Fig. 1). We only also add the 3s channel, since it is conceptually very similar.

### A.1. The 3s-1s two-photon channel

We derive the rate equation that describes the evolution of the population,  $N_{3s}$ , in the 3s level, but where we take into account the two-photon aspect of the 3s-1s transition. In the normal “1 + 1” photon picture, this transition is described by the sequence  $3s \rightarrow 2p \rightarrow 1s$  and its inverse process  $1s \rightarrow 2p \rightarrow 3s$ . For the 3s rate equation, it is therefore clear that the two-photon correction due to the 3s-1s channel should affect part of the  $3s \rightarrow 2p$  and  $2p \rightarrow 3s$  rate. Once this part is known, one can in principle replace it in the rate equations using a more complete two-photon description.

Here we provide the formulation of this problem, also because it allows to understand the most important aspects of the two-photon picture. However, to compute the corrections to the escape probability we directly use the (precomputed) solution for the populations given in the standard approach, and only solve for the presumably small correction to the evolution of the photon field around the Lyman  $\alpha$  resonance. Solving the complete set of modified rate equations simultaneously will be the final goal, for which one will need the results of the derivation presented here. We leave this problem to future work.

#### A.1.1. Isolating the different “1 + 1” photon routes

To isolate the contribution from the 3s-1s two-photon channel, we start by writing down the 3s rate equation in the “1 + 1” photon picture, including all possible ways for electrons in and out of the 3s-level

$$\frac{dN_{3s}}{dt} = \left. \frac{dN_{3s}}{dt} \right|_{3s2p} + R_{3s}^+ - R_{3s}^- N_{3s}. \quad (\text{A.1})$$

Here we directly separated the part due to the Balmer  $\alpha$  transition

$$\begin{aligned} \left. \frac{dN_{3s}}{dt} \right|_{3s2p} &= R_{2p3s} - R_{3s2p} N_{3s} \\ &\equiv N_{2p} A_{3s2p} \frac{g_{3s}}{g_{2p}} n_{\text{pl}}(\nu_{32}) - N_{3s} A_{3s2p} [1 + n_{\text{pl}}(\nu_{32})], \end{aligned} \quad (\text{A.2})$$

which we discuss below in more detail. Here  $N_i$  and  $g_i$  denote the population and statistical weight of level  $i$ ,  $n_{\text{pl}}(\nu)$  is the CMB blackbody occupation number, and  $A_{ij}$  and  $\nu_{ij}$  are the transition rate and frequency between level  $i$  and  $j$ . All the other possible channels in and out of the 3s-level lead to the terms

$$R_{3s}^- = R_{3sc} + \sum_{i>3s} \frac{g_i}{g_{3s}} A_{i3s} n_{\text{pl}}(\nu_{i3s}) \quad (\text{A.3})$$

$$R_{3s}^+ = N_e N_p R_{c3s} + \sum_{i>3s} N_i A_{i3s} [1 + n_{\text{pl}}(\nu_{i3s})], \quad (\text{A.4})$$

where  $N_e$  and  $N_p$  are the free electron and proton number densities, and  $R_{ci}$  and  $R_{ic}$  are the recombination and photoionization rates to the level  $i$ . We note that, since at frequencies below the Lyman  $\alpha$  line the spectral distortions during recombination are small (e.g., cf. Chluba & Sunyaev 2006a), above we have replaced  $n(\nu) \rightarrow n_{\text{pl}}(\nu)$  everywhere.

<sup>14</sup> <http://cosmos.astro.uiuc.edu/rico/>

Now we are interested in refining the term connected with the Balmer  $\alpha$  channel. Since any two-photon or multi-photon process only leads to tiny corrections in the total decay rates, it is possible to use the one-photon rates to compute the relative contributions of different transition sequences. It is clear that the term  $N_{3s} A_{3s2p}^* \equiv N_{3s} A_{3s2p} [1 + n_{\text{pl}}(\nu_{32})]$  describes the total flow of electrons in the direction of the 2p-state. Once the electron has reached there, it can return to the 3s level with the probability

$$p_{2p3s} = \frac{A_{3s2p} \frac{g_{3s}}{g_{2p}} n_{\text{pl}}(\nu_{32})}{A_{2p1s}^* + R_{2p}^-}. \quad (\text{A.5})$$

Here  $A_{2p1s}^* = A_{2p1s} [1 + n_{\text{pl}}(\nu_{21})]$  is the stimulated Lyman  $\alpha$  emission rate in the ambient CMB blackbody field, and  $R_{2p}^-$  is the total rate at which electrons can leave the 2p-level, but excluding the Lyman  $\alpha$  line. It is given by

$$R_{2p}^- = R_{2pc} + \sum_{i>2p} \frac{g_i}{g_{2p}} A_{i2p} n_{\text{pl}}(\nu_{i2p}). \quad (\text{A.6})$$

Similarly, the electron can take the route  $2p \rightarrow 1s$  with the probability

$$p_{2p1s} = \frac{A_{2p1s}^*}{A_{2p1s}^* + R_{2p}^-} \equiv p_{\text{em}}^{1\gamma}, \quad (\text{A.7})$$

or any of the other channels ( $2p \rightarrow ns$  ( $n > 2$ ),  $2p \rightarrow nd$  or  $2p \rightarrow c$ ) with probability  $\bar{p}_{2p1s} = 1 - p_{2p1s}$ . We note that here we have neglected deviations from a blackbody in the stimulated Lyman  $\alpha$  emission rate, which in any case is tiny. We just wish to maintain the structure of the equations.

It is then clear that the term  $N_{3s} A_{3s2p}^*$  can be interpreted as

$$N_{3s} A_{3s2p}^* \equiv N_{3s} A_{3s2p} \times [p_{2p1s} + \bar{p}_{2p1s}], \quad (\text{A.8})$$

because the total flow of electrons should be divided into those electrons that go to the 1s-level (probability  $p_{2p1s}$ ) and those that do not (probability  $\bar{p}_{2p1s}$ ).

From the physical point of view, it is now clear that the *partial* flow connected with  $p_{2p1s} N_{3s} A_{3s2p}^*$  should be interpreted as 3s-1s two-photon emission in the “1 + 1”-photon picture, which we later replace with the more proper two-photon formulae. The rest ( $\bar{p}_{2p1s} N_{3s} A_{3s2p}^*$ ) describes the contributions of all the other possible channels, e.g., also including the Balmer  $\alpha$  scattering transition  $3s \rightarrow 2p \rightarrow 3s$ . We continue to describe all these in the “1 + 1” photon picture.

To understand the term connected to the total flow of electrons from the 2p-level towards the 3s-state, given by  $N_{2p} A_{3s2p} \frac{g_{3s}}{g_{2p}} n_{\text{pl}}(\nu_{32})$ , we must consider an electron that is added to the 2p-state. It will take the route  $2p \rightarrow 3s$  with probability  $p_{2p3s}$  as given by Eq. (A.5). If we consider all possible routes into the 2p-state, and write the corresponding total rate as  $R_{2p}^{+,i} = R_{2p}^+ + N_{1s} \frac{g_{2p}}{g_{1s}} A_{2p1s} n(\nu_{21})$ , then one has the identity

$$N_{2p} A_{3s2p} \frac{g_{3s}}{g_{2p}} n_{\text{pl}}(\nu_{32}) \equiv p_{2p3s} [R_{2p}^+ + N_{1s} \frac{g_{2p}}{g_{1s}} A_{2p1s} n(\nu_{21})] \quad (\text{A.9a})$$

where

$$R_{2p}^+ = N_e N_p R_{c2p} + \sum_{i>2p} N_i A_{i2p} [1 + n_{\text{pl}}(\nu_{i2p})]. \quad (\text{A.9b})$$

One can now write

$$\frac{dN_{3s}}{dt} \Big|_{3s2p} = p_{2p3s} R_{2p}^+ - \bar{p}_{2p1s} N_{3s} A_{3s2p}^* + \frac{dN_{3s}}{dt} \Big|_{3s2p1s}^{1+1}, \quad (\text{A.10a})$$

where

$$\frac{dN_{3s}}{dt} \Big|_{3s2p1s}^{1+1} = p_{2p3s} N_{1s} \frac{g_{2p}}{g_{1s}} A_{2p1s} n(\nu_{21}) - p_{2p1s} N_{3s} A_{3s2p}^*. \quad (\text{A.10b})$$

The first two terms in Eq. (A.10a) describe the partial flow of electrons towards the 3s-state, but only where it is certain that the electron did not pass through the Lyman  $\alpha$  line before. The last term is the fractional contribution of the  $3s \leftrightarrow 2p \leftrightarrow 1s$ -channel in the 3s rate equation, but described by the “1 + 1” photon picture. This is the term that we wish to replace with the two-photon formulae.

If we now identify

$$A_{3s1s}^{2\gamma} = \frac{A_{3s2p} A_{2p1s}}{A_{2p1s}^* + R_{2p}^-}, \quad (\text{A.11})$$

then we can finally rewrite Eq. (A.10b) as

$$\frac{dN_{3s}}{dt} \Big|_{3s2p1s}^{1+1} = A_{3s1s}^{2\gamma} N_{1s} \frac{g_{3s}}{g_{1s}} n(\nu_{21}) n_{\text{pl}}(\nu_{32}) - A_{3s1s}^{2\gamma} N_{3s} [1 + n_{\text{pl}}(\nu_{21})][1 + n_{\text{pl}}(\nu_{32})]. \quad (\text{A.12})$$

We note that in a vacuum, one would have  $A_{3s1s}^{2\gamma} \equiv A_{3s2p}$ , as it should be, since the electron will only have one way to leave the 2p-state. However, within an intense CMB background field, the other channels will also become active (e.g.,  $3s \leftrightarrow 2p \leftrightarrow c$ ), so that part of the  $3s \leftrightarrow 2p$  flow will go through them. This reduces the effective decay rate  $A_{3s1s}^{2\gamma}$ .

### A.1.2. Replacing the 3s-1s channel in the “1 + 1” photon formulation with the two-photon expression

We now wish to replace the part due to  $\frac{dN_{3s}}{dt} \Big|_{3s2p1s}^{1+1}$  with the more proper two-photon terms. For this we have to consider the detailed form of the 3s-1s two-photon term. If one considers an electron that is initially in the 3s-state, then one can use the vacuum 3s-1s two-photon decay profile to derive the emission profile needed to describe the injection of Lyman  $\alpha$  photons in the escape problem. Simple formulae for the necessary vacuum two-photon decay profiles can be found in the literature (Chluba & Sunyaev 2008). We shall normalize these profiles like  $\int_0^\infty \frac{\phi_i^{2\gamma}(\nu)}{4\pi \Delta\nu_D} d\nu d\Omega \equiv 1$ , where  $\phi_i^{2\gamma}(\nu)$  already includes the motion of the atoms in the same way as for the normal Lorentzian lines, usually leading to the Voigt profiles (e.g., see Mihalas 1978). For convenience, we chose the Lyman  $\alpha$  Doppler-width,  $\Delta\nu_D$ , in the normalization.

With this, the net change in the number density of electrons in the 3s level by means of the 3s-1s two-photon channel is given by

$$\begin{aligned} \frac{dN_{3s}}{dt} \Big|_{3s1s}^{2\gamma} &= A_{3s1s}^{2\gamma} N_{1s} \int \varphi_{3s}^{2\gamma}(\nu) n(\nu) n(\nu_{31} - \nu) d\nu \\ &\quad - A_{3s1s}^{2\gamma} N_{3s} \int \varphi_{3s}^{2\gamma}(\nu) [1 + n(\nu)][1 + n(\nu_{31} - \nu)] d\nu \quad (\text{A.13a}) \end{aligned}$$

$$\begin{aligned} &\approx A_{3s1s}^{2\gamma} N_{1s} n(\nu_{21}) n_{\text{pl}}(\nu_{32}) \\ &\quad - A_{3s1s}^{2\gamma} N_{3s} [1 + n_{\text{pl}}(\nu_{21})][1 + n_{\text{pl}}(\nu_{32})], \quad (\text{A.13b}) \end{aligned}$$

where  $A_{3s1s}^{2\gamma}$  is the effective 3s-1s two-photon decay rate, which in a vacuum is<sup>15</sup>  $A_{3s1s}^{2\gamma} \approx A_{3s2p}$ , but within an ambient blackbody radiation field should take the value given by Eq. (A.11). Furthermore,  $\varphi_{3s}^{2\gamma} = \phi_{3s}^{2\gamma}(\nu)/\Delta\nu_D$  denotes the 3s-1s two-photon decay profile, and  $\nu_{31}$  is the 3s-1s transition frequency. We note that here we have neglected the factor  $g_{3s}/g_{1s} = 1$  in our notation. However, for the case of the 3d-1s two-photon decay channel it must be included.

For the approximation Eq. (A.13b), three comments should be made: first we have assumed that the main contributions to the integrals over the two-photon line profiles come from the poles close to  $\nu \sim \nu_{21}$  and  $\nu \sim \nu_{32}$ . Second, we have assumed that the CMB spectral distortion around the Balmer  $\alpha$  line are tiny. The stimulated term in the vicinity of the Lyman  $\alpha$  resonance also is completely negligible, so that we can use  $1 + n(\nu_{21}) \approx 1 + n_{\text{pl}}(\nu_{21})$  instead, without changing anything. And finally, we assumed that only for the 1s-3s two-photon absorption rate do the deviations of the CMB spectrum from a blackbody in the vicinity of the Lyman  $\alpha$  resonance matter.

The result presented in Eq. (A.13b) is identical to the term given by the “1+1” photon picture, Eq. (A.12). This is unsurprising, since with the above approximations we have simply turned from the two-photon to the “1+1” photon picture. In order to include the effect of two-photon transitions in to the rate equation of the 3s-level, we should therefore replace  $\frac{dN_{3s}}{dt}|_{3s2p1s}^{1+1}$  with the full integral given by Eq. (A.13a).

### A.1.3. Term in the Lyman $\alpha$ radiative transfer equation

To use the integral (A.13a) in the computations of the ionization history, we also have to consider the solution to the CMB spectral distortion in the vicinity of the Lyman  $\alpha$  resonance. We therefore have to explicitly write the 3s-1s two-photon emission and absorption terms for the evolution of the photon field and solve the corresponding transfer equation. In particular, we wish to bring the transfer equation into the form Eq. (4).

From Eq. (A.13a), it follows directly that

$$\begin{aligned} \frac{1}{c} \frac{\partial N_\nu}{\partial t} \Big|_{3s1s}^{2\gamma} &= \frac{2A_{3s1s}^{2\gamma}}{4\pi} N_{3s} \varphi_{3s}^{2\gamma}(\nu) [1 + n(\nu)] [1 + n(\nu_{31} - \nu)] \\ &\quad - \frac{2A_{3s1s}^{2\gamma}}{4\pi} N_{1s} \varphi_{3s}^{2\gamma}(\nu) n(\nu) n(\nu_{31} - \nu). \end{aligned} \quad (\text{A.14})$$

Here the factor of 2 is because per electron two photons are involved, and the factor of  $4\pi$  converts to per steradian, bearing in mind that the medium is isotropic. Furthermore in this form it is assumed that every two-photon interaction in the 3s-1s channel leads to a *complete redistribution* of the photons over the entire two-photon profile. This also means that we have not distinguished two-photon emission and absorption from two-photon scattering events. However, this should be a very good approximation, since the scattering event involves two photons. This means that the total energy of the incoming photons will be divided such that in most cases the scattered photons will have energy  $\nu \sim \nu_{21}$  and  $\nu' \sim \nu_{32}$ . We note that this does not imply that we use a complete redistribution approximation for the Lyman  $\alpha$  resonance scattering itself, since only about

$\sim 10^{-4} - 10^{-3}$  of all interactions will lead to the 3s- and 3d-state via two-photon interactions (Chluba & Sunyaev 2009c).

Neglecting the deviations from the blackbody spectrum in the emission term and comparing with Eq. (4), we can identify that

$$\phi_{3s\leftrightarrow 1s}(\nu) = 2 \phi_{3s}^{2\gamma}(\nu) \frac{1 + n_{\text{pl}}(\nu)}{1 + n_{\text{pl}}(\nu_{21})} \frac{1 + n_{\text{pl}}(\nu_{31} - \nu)}{1 + n_{\text{pl}}(\nu_{32})} \quad (\text{A.15a})$$

$$\begin{aligned} &\stackrel{\nu \geq \nu_{31}/2}{\downarrow} \approx 2 \phi_{3s}^{2\gamma}(\nu) \frac{1 + n_{\text{pl}}(\nu_{31} - \nu)}{1 + n_{\text{pl}}(\nu_{32})} \end{aligned} \quad (\text{A.15b})$$

$$p_{\text{em}}^{1\gamma} = \frac{A_{2p1s}^*}{A_{2p1s}^* + R_{2p}^-} \quad (\text{A.15c})$$

$$R_{2p}^{3s,+} = A_{3s2p}^* N_{3s}. \quad (\text{A.15d})$$

This result shows that the effective profile of the process as expected is given by the two-photon profile for the 3s-1s channel, including the induced terms relative to the values at the Lyman and Balmer  $\alpha$  resonance. The emission probability is also exactly the Lyman  $\alpha$  emission probability including the induced emission for the central frequency of the Lyman  $\alpha$  line. And the last term simply represents the number density of 3s-electrons that reach the 2p-state per second in the “1+1” photon picture, where again the stimulated emission due to CMB photons close to the Balmer  $\alpha$  frequency is included.

We note that  $\phi_{3s\leftrightarrow 1s}(\nu)$  is no longer normalized to unity.

In a vacuum, one would find that  $\int_0^\infty \frac{\phi_{3s\leftrightarrow 1s}^{2\gamma}(\nu)}{4\pi \Delta\nu_D} d\nu d\Omega \equiv 2$ , while within the CMB blackbody field  $\int_0^\infty \frac{\phi_{3s\leftrightarrow 1s}^{2\gamma}(\nu)}{4\pi \Delta\nu_D} d\nu d\Omega \gtrsim 2$ . However the relative correction to the overall normalization of the profile due to stimulated emission is of the order of  $\sim 10^{-9} - 10^{-8}$  (see Sect. 5.2.1). One should also mention that because of the symmetry in the profile around  $\nu = \nu_{31}/2$ , by restricting the range of integration to  $\nu_{31}/2 \leq \nu \leq \nu_{31}$  one can avoid counting both the Lyman  $\alpha$  and Balmer  $\alpha$  photons. We use this to simplify the numerical integration (see Sect. 2.3.1).

If we now look at the absorption term in Eq. (A.14), using the definitions in Eq. (A.15) we can directly write

$$\begin{aligned} \frac{1}{c} \frac{\partial N_\nu}{\partial t} \Big|_{3s1s,\text{abs}}^{2\gamma} &= \frac{\phi_{3s\leftrightarrow 1s}(\nu)}{4\pi \Delta\nu_D} A_{3s1s}^{2\gamma} N_{1s} n(\nu) n_{\text{pl}}(\nu_{31} - \nu) \\ &\quad \times \frac{1 + n_{\text{pl}}(\nu_{21})}{1 + n_{\text{pl}}(\nu)} \frac{1 + n_{\text{pl}}(\nu_{32})}{1 + n_{\text{pl}}(\nu_{31} - \nu)}. \end{aligned} \quad (\text{A.16})$$

Here we have already assumed that for our problem the important part is the region  $\nu \geq \nu_{31}/2$ . This implies that  $\nu_{31} - \nu \leq \nu_{31}/2$ , so that the deviations from the CMB blackbody can be neglected leading to  $n(\nu) n_{\text{pl}}(\nu_{31} - \nu)$  instead of  $n(\nu) n(\nu_{31} - \nu)$ . Since according to Eqs. (A.5) and (A.11),  $A_{3s1s}^{2\gamma} \equiv p_{2p3s} \frac{g_{2p} A_{2p1s}}{g_{3s} n_{\text{pl}}(\nu_{32})}$ , and because  $[1 + n_{\text{pl}}(\nu)]/n_{\text{pl}}(\nu) = e^{h\nu/kT_\gamma}$ , we finally find that

$$\begin{aligned} \frac{1}{c} \frac{\partial N_\nu}{\partial t} \Big|_{3s1s,\text{abs}}^{2\gamma} &= \frac{\phi_{3s\leftrightarrow 1s}(\nu)}{4\pi \Delta\nu_D} \frac{A_{2p1s}}{g_{3s}} \frac{p_{2p3s}}{g_{2p}} e^{\frac{h[\nu - \nu_{21}]}{kT_\gamma}} \\ &\quad \times \frac{1 + n_{\text{pl}}(\nu_{21})}{1 + n_{\text{pl}}(\nu)} n(\nu) N_{1s} \end{aligned} \quad (\text{A.17a})$$

$$\begin{aligned} &\stackrel{\nu \geq \nu_{31}/2}{\downarrow} \approx \frac{\phi_{3s\leftrightarrow 1s}(\nu)}{4\pi \Delta\nu_D} \frac{g_{2p}}{g_{1s}} A_{2p1s} p_{2p3s} e^{\frac{h[\nu - \nu_{21}]}{kT_\gamma}} n(\nu) N_{1s}. \end{aligned} \quad (\text{A.17b})$$

Note that  $g_{3s}/g_{2p} \equiv g_{1s}/g_{2p}$ .

<sup>15</sup> Here the approximate sign is due to the fact that the rate coefficient in the two-photon formulation should contain some small ( $\sim 10^{-6} - 10^{-5}$ ) quantum mechanical correction to the one photon rate. This will not lead to any significant correction in the escape probability.

With the Einstein relations, it is then easy to show that  $\frac{g_{2p}}{g_{1s}} A_{2p1s} n(\nu) = h\nu_{21} B_{12} \frac{\nu_{21}^2}{\nu^2} N_\nu$ , so that we directly verify the thermodynamic correction factor<sup>16</sup>  $f_\nu = \frac{\nu_{21}^2}{\nu^2} e^{h[\nu-\nu_{21}]/kT_\gamma}$  and find that  $p_d^{1s3s} \equiv p_{2p3s}$ . We therefore have confirmed the completeness of the form of Eq. (4) for the 3s-1s two-photon channel.

### A.2. The 3d-1s two-photon channel

After going through the argument for the 3s-1s channel, it is easy to do the same for the 3d-1s channel. For the rate equation analog to Eqs. (A.1), (A.3), and (A.10), one has

$$\frac{dN_{3d}}{dt} = \left. \frac{dN_{3d}}{dt} \right|_{3d2p} + R_{3d}^+ - R_{3d}^- N_{3d} \quad (\text{A.18a})$$

$$R_{3d}^- = R_{3dc} + \sum_{i>3d} \frac{g_i}{g_{3d}} A_{i3d} n_{\text{pl}}(\nu_{i3d}) \quad (\text{A.18b})$$

$$R_{3d}^+ = N_e N_p R_{c3d} + \sum_{i>3d} N_i A_{i3s} [1 + n_{\text{pl}}(\nu_{i3d})], \quad (\text{A.18c})$$

where the Balmer  $\alpha$  channel is defined by

$$\left. \frac{dN_{3d}}{dt} \right|_{3d2p} = p_{2p3d} R_{2p}^+ - \bar{p}_{2p1s} N_{3d} A_{3d2p}^* + \left. \frac{dN_{3d}}{dt} \right|_{3d2p1s}^{1+1} \quad (\text{A.18d})$$

$$p_{2p3d} = \frac{A_{3d2p} \frac{g_{3d}}{g_{2p}} n_{\text{pl}}(\nu_{32})}{A_{2p1s}^* + R_{2p}^-} \quad (\text{A.18e})$$

$$\begin{aligned} \left. \frac{dN_{3d}}{dt} \right|_{3d2p1s}^{1+1} &= A_{3d1s}^{2\gamma} N_{1s} \frac{g_{3d}}{g_{1s}} n(\nu_{21}) n_{\text{pl}}(\nu_{32}) \\ &\quad - A_{3d1s}^{2\gamma} N_{3d} [1 + n_{\text{pl}}(\nu_{21})][1 + n_{\text{pl}}(\nu_{32})]. \end{aligned} \quad (\text{A.18f})$$

As before, one should now replace Eq. (A.18f) with

$$\begin{aligned} \left. \frac{dN_{3d}}{dt} \right|_{3d1s}^{2\gamma} &= A_{3d1s}^{2\gamma} \frac{g_{3d}}{g_{1s}} N_{1s} \int \varphi_{3d}^{2\gamma}(\nu) n(\nu) n(\nu_{31} - \nu) d\nu \\ &\quad - A_{3d1s}^{2\gamma} N_{3d} \int \varphi_{3d}^{2\gamma}(\nu) [1 + n(\nu)][1 + n(\nu_{31} - \nu)] d\nu \end{aligned} \quad (\text{A.19a})$$

$$A_{3d1s}^{2\gamma} = \frac{A_{3d2p} A_{2p1s}}{A_{2p1s}^* + R_{2p}^-}, \quad (\text{A.19b})$$

if one is interested in the 3d-1s two-photon correction to the 3d-rate equation. We note that here the ratio of the statistical weights is not unity as for the 3s-1s channel.

The terms for the transfer equation can also be cast in the form of Eq. (4) where the important coefficients are given by

$$\phi_{3d \leftrightarrow 1s}(\nu) = 2 \phi_{3d}^{2\gamma}(\nu) \frac{1 + n_{\text{pl}}(\nu)}{1 + n_{\text{pl}}(\nu_{21})} \frac{1 + n_{\text{pl}}(\nu_{31} - \nu)}{1 + n_{\text{pl}}(\nu_{32})} \quad (\text{A.20a})$$

$$\approx 2 \phi_{3d}^{2\gamma}(\nu) \frac{1 + n_{\text{pl}}(\nu_{31} - \nu)}{1 + n_{\text{pl}}(\nu_{32})} \quad (\text{A.20b})$$

$$R_{2p}^{3s,+} = A_{3d2p}^* N_{3d} \quad (\text{A.20c})$$

$$p_d^{1s3d} = p_{2p3d}. \quad (\text{A.20d})$$

<sup>16</sup> From Eq. (A.17a) by comparing with Eq. (4), we can see that for our choice of coefficients and variables we can more rigorously infer  $f_\nu = \frac{\nu_{21}^2}{\nu^2} e^{\frac{h[\nu-\nu_{21}]}{kT_\gamma}} \frac{1+n_{\text{pl}}(\nu_{21})}{1+n_{\text{pl}}(\nu)} \equiv \frac{\nu_{21}^2}{\nu^2} \frac{n_{\text{pl}}(\nu_{21})}{n_{\text{pl}}(\nu)} \approx \frac{\nu_{21}^2}{\nu^2} e^{h[\nu-\nu_{21}]/kT_\gamma}$  for  $h\nu \gg kT_\gamma$ , a condition that is fulfilled during cosmological recombination in the vicinity ( $\nu \gtrsim \nu_{31}/2$ ) of the Lyman  $\alpha$  resonance.

### A.3. The other channels

For the other channels in and out of the 2p-state, we can also derive the corresponding partial rates in a similar way as for the 3s and 3d state. However, since the main correction is expected to come from the 3s and 3d two-photon channels for these we simply use the “1 + 1” photon picture. This means that we will not replace the corresponding  $i \leftrightarrow 2p$  rates with the two-photon description. For all the  $ns$  and  $nd$ -states with  $n > 3$ , the rate equations will therefore be similar to Eq. (A.18), and for electrons in the continuum one will have

$$\frac{dN_e}{dt} = \left. \frac{dN_e}{dt} \right|_{c2p} + \sum_{i>2} [R_{ic} N_i - N_e N_p R_{ci}], \quad (\text{A.21a})$$

where

$$\left. \frac{dN_e}{dt} \right|_{c2p} = p_{2pc} R_{2p}^+ - \bar{p}_{2p1s} N_e N_p R_{c2p} + \left. \frac{dN_e}{dt} \right|_{c2p1s}^{1+1} \quad (\text{A.21b})$$

$$p_{2pc} = \frac{R_{2pc}}{A_{2p1s}^* + R_{2p}^-} \quad (\text{A.21c})$$

$$\left. \frac{dN_e}{dt} \right|_{c2p1s}^{1+1} = N_{1s} \frac{g_{2p}}{g_{1s}} A_{2p1s} n(\nu_{21}) p_{2pc} - p_{2p1s} N_e N_p R_{c2p}. \quad (\text{A.21d})$$

There remains a small difference to the normal rate equations. In the formulation given above, the population of the 2p-state has vanished from *all* the rate equations, and in particular from those for the 3s and 3d-state. For the 3s and 3d-state, this is physically expected, since in the two-photon picture on the way to the 1s-level the electron does not really pass through the 2p-state. In the full two-photon picture, the electron reaches the 1s level via *all* intermediate p-states, including those in the continuum. For the other levels, the above formulation would have also been obtained by simply replacing the solution of the 2p-state with the quasi-stationary value in the “1 + 1” photon approach. In this way, one again has a closed system of rate equations, which avoids the difficulty of attaching a population to the 2p-state.

## Appendix B: Derivation of the thermodynamic factor using the “1 + 1” photon picture

As mentioned in the introduction and also earlier (Chluba & Sunyaev 2009c), in the normal “1 + 1” photon approximation the term describing the emission and absorption of Lyman  $\alpha$  photons in full thermodynamic equilibrium does *not* exactly conserve a blackbody spectrum at all frequencies. This can be directly seen from Eq. (1), since in full thermodynamic equilibrium one should have  $(p_{\text{em}}^{1\gamma} R_{2p}^+)^{\text{eq}} \equiv (p_d^{1\gamma} h\nu_{21} B_{12} N_{1s} N_\nu)^{\text{eq}}$ . Using the definitions of the previous section, in equilibrium one expects  $(R_{2p}^+)^{\text{eq}} \equiv (R_{2p}^- N_{2p})^{\text{eq}}$ ,  $N_{2p}^{\text{eq}} \equiv \frac{g_{2p}}{g_{1s}} N_{1s}^{\text{eq}} e^{-\frac{h\nu_{21}}{kT_\gamma}}$ ,  $h\nu_{21} B_{12} \equiv \frac{g_{2p}}{g_{1s}} \frac{c^2 A_{21}}{2\nu_{21}^2}$ , and  $p_{\text{em}}^{1\gamma} \equiv A_{21} [1 + n_{\text{pl}}(\nu_{21})] p_d^{1\gamma} / R_{2p}^-$ , so that one finds

$$\left( \frac{p_d^{1\gamma} h\nu_{21} B_{12} N_{1s} N_\nu}{p_{\text{em}}^{1\gamma} R_{2p}^+} \right)^{\text{eq}} \equiv \frac{c^2}{2\nu_{21}^2} \frac{N_\nu^{\text{pl}}}{1 + n_{\text{pl}}(\nu_{21})} e^{\frac{h\nu_{21}}{kT_\gamma}}. \quad (\text{B.1})$$

Here  $N_\nu^{\text{pl}} = \frac{2\nu^2}{c^2} n_{\text{pl}}(\nu)$  defines the blackbody spectrum. With the identity  $[1 + n_{\text{pl}}(\nu)]/n_{\text{pl}}(\nu) \equiv e^{h\nu/kT_\gamma}$ , one therefore has

$$\left( \frac{p_d^{1\gamma} h\nu_{21} B_{12} N_{1s} N_\nu}{p_{\text{em}}^{1\gamma} R_{2p}^+} \right)^{\text{eq}} \equiv \frac{\nu^2}{\nu_{21}^2} \frac{1 + n_{\text{pl}}(\nu)}{1 + n_{\text{pl}}(\nu_{21})} e^{\frac{h[\nu_{21}-\nu]}{kT_\gamma}} \approx 1/f_\nu \quad (\text{B.2})$$

In the last step, we assumed that  $h\nu \gg kT_\gamma$  and  $h\nu_{21} \gg kT_\gamma$ , so that the factors  $[1 + n]$  could be neglected, an approximation that is certainly possible during cosmological recombination. However, it is only due to the used definition of  $p_{\text{em}}^{1\gamma}$ , in which we evaluated the stimulated emission factors at the Lyman  $\alpha$  line center only and in addition directly assumed a blackbody spectrum. More consistently, one should have used  $p_{\text{em}}^{1\gamma} = p_{\text{em}}^{1\gamma,*} [1 + n_\nu]$ , where we have

$$p_{\text{em}}^{1\gamma,*} = \frac{A_{2p1s}}{A_{2p1s}[1 + \langle n_\nu \rangle_{\text{em}}] + R_{2p}^-}. \quad (\text{B.3})$$

Here  $\langle n_\nu \rangle_{\text{em}}$  denotes the average of the photon occupation number across the Lyman  $\alpha$  emission profile. With this definition in Eq. (B.2), one would have obtained the factor  $1/f_\nu$  directly, without any additional comment.

We mention another way to obtain the thermodynamic factor in the absorption process, which just uses the term in the Lyman  $\alpha$  rate equation. In the standard textbooks (e.g., [Mihalas 1978](#)), one finds that

$$\left. \frac{dN_{2p}}{dt} \right|_{2p1s}^{1+1} = N_{1s} \frac{g_{2p}}{g_{1s}} A_{2p1s} n(\nu_{21}) - N_{2p} A_{2p1s} [1 + n(\nu_{21})]. \quad (\text{B.4})$$

Here two comments should be made: (i) more rigorously one should replace  $n(\nu_{21})$  with the average occupation number over the line profile, i.e.,  $n(\nu_{21}) \rightarrow \langle n_\nu \rangle$  and (ii) in addition one should distinguish between the emission and absorption process, implying that  $[1 + n(\nu_{21})] \rightarrow [1 + \langle n_\nu \rangle_{\text{em}}]$ , while in the first term one has  $n(\nu_{21}) \rightarrow \langle n_\nu \rangle_{\text{abs}}$ . In full equilibrium, one should then find that  $(N_{1s} \frac{g_{2p}}{g_{1s}} A_{2p1s} \langle n_\nu \rangle_{\text{abs}})^{\text{eq}} = (N_{2p} A_{2p1s} [1 + \langle n_\nu \rangle_{\text{em}}])^{\text{eq}}$ , so that

$$\left( \frac{N_{1s} \frac{g_{2p}}{g_{1s}} A_{2p1s} \langle n_\nu \rangle_{\text{abs}}}{N_{2p} A_{2p1s} [1 + \langle n_\nu \rangle_{\text{em}}]} \right)^{\text{eq}} = \frac{\langle n_\nu^{\text{pl}} \rangle_{\text{abs}} e^{h\nu_{21}/kT_\gamma}}{1 + \langle n_\nu^{\text{pl}} \rangle_{\text{em}}} \equiv 1. \quad (\text{B.5})$$

It is now easy to show that

$$\begin{aligned} \langle n_\nu^{\text{pl}} \rangle_{\text{abs}} e^{h\nu_{21}/kT_\gamma} &\equiv \left\langle \frac{n_\nu^{\text{pl}}}{1 + n_\nu^{\text{pl}}} [1 + n_\nu^{\text{pl}}] \right\rangle_{\text{abs}} e^{h\nu_{21}/kT_\gamma} \\ &\equiv \left\langle e^{h[\nu_{21}-\nu]/kT_\gamma} [1 + n_\nu^{\text{pl}}] \right\rangle_{\text{abs}}. \end{aligned} \quad (\text{B.6})$$

Since according to Eq. (B.5)  $\langle n_\nu^{\text{pl}} \rangle_{\text{abs}} e^{h\nu_{21}/kT_\gamma} \equiv \langle 1 + n_\nu^{\text{pl}} \rangle_{\text{em}}$ , one should conclude that  $\langle n_\nu \rangle_{\text{abs}} \equiv \langle e^{h[\nu-\nu_{21}]/kT_\gamma} n_\nu \rangle_{\text{em}}$ , where  $n_\nu$  is now an arbitrary photon occupation number. In terms of  $N_\nu = \frac{h\nu^2}{c^2} n_\nu$ , one therefore has  $\langle N_\nu \rangle_{\text{abs}} \equiv \frac{2\nu^2}{c^2} \langle n_\nu \rangle_{\text{abs}} \equiv \langle f_\nu N_\nu \rangle_{\text{em}}$ . With this we obtained the thermodynamic correction factor  $f_\nu$  in the absorption profile for  $N_\nu = \frac{h\nu^2}{c^2} n_\nu$ , since  $\langle N_\nu \rangle_{\text{abs}} \equiv \langle f_\nu N_\nu \rangle_{\text{em}}$  automatically implies that  $\phi_{\text{abs}} \equiv f_\nu \phi_{\text{em}}$ .

### Appendix C: Computation of two-photon profiles

We compute the two-photon decay profiles according to the work of [Chluba & Sunyaev \(2009c\)](#). There in particular the infinite sum over intermediate states was divided into two sets of states with principal quantum numbers  $n > n_i$  and  $n \leq n_i$ , where  $n_i$  is the initial state principal quantum number. This makes the sum over the resonances (in the case of 3s and 3d, only one) finite and allows us to give fitting formulae for the remaining contribution to the total matrix element from the infinite sum. This procedure is very convenient for numerical evaluations.

Here we would like to mention that the two-photon decay profiles behave like  $\phi \propto \nu(\nu_{i1s} - \nu)$  in the limits  $\nu \rightarrow 0$  or  $\nu \rightarrow \nu_{i1s}$ . This is because in this limit the main term in the infinite sum originates in the matrix element  $n_i s/d \rightarrow n_i p$ , which in the non-relativistic formulation has zero transition frequency. This implies that for  $\nu \rightarrow 0$  or  $\nu \rightarrow \nu_{i1s}$

$$\begin{aligned} \phi_{n_i s/d \rightarrow 1s}^{2\gamma} &\approx G_{n_i i} y (1 - y) \left| \langle R_{1s} | r | R_{n_i p} \rangle \langle R_{n_i p} | r | R_{n_i i} \rangle \right|^2 \\ &\approx G_{n_i i} y (1 - y) 2^6 3^2 n_i^9 \frac{(n_i - 1)^{2n_i - 5}}{(n_i + 1)^{2n_i + 5}} (n_i^2 - 1) 4. \end{aligned} \quad (\text{C.1})$$

Here  $1|4$  means 1 for the s-states or 4 for the d-states. Inserting numbers (for definitions see [Chluba & Sunyaev 2008](#)), one finds

$$\phi_{n_i s \rightarrow 1s}^{2\gamma} \approx 1.0598 \times 10^4 y (1 - y) \frac{(n_i - 1)^{2n_i}}{(n_i + 1)^{2n_i}} \frac{n_i^2 - 1}{n_i} s^{-1} \quad (\text{C.2a})$$

$$\phi_{n_i d \rightarrow 1s}^{2\gamma} \approx 4.2393 \times 10^3 y (1 - y) \frac{(n_i - 1)^{2n_i}}{(n_i + 1)^{2n_i}} \frac{n_i^2 - 4}{n_i} s^{-1}. \quad (\text{C.2b})$$

For the 3s and 3d profiles, one therefore has

$$\phi_{3s \rightarrow 1s}^{2\gamma}(y) \approx 441.6 y (1 - y) s^{-1} \quad (\text{C.3a})$$

$$\phi_{3d \rightarrow 1s}^{2\gamma}(y) \approx 110.4 y (1 - y) s^{-1}. \quad (\text{C.3b})$$

We use these simple formulae to compute the two-photon spectra at  $0 \leq y \leq 0.001$  and  $0.999 \leq y \leq 1$ .

The most important consequence of this limiting behavior with frequency is that because of stimulated emission in the ambient CMB blackbody radiation field the two-photon profiles no longer vanish at  $y \sim 0$  and  $y \sim 1$ , since  $n_{\text{pl}}(\nu) \sim 1/y$  for  $\nu \sim 0$ . For the 2s-1s two-photon process, this behavior was also seen earlier ([Chluba & Sunyaev 2006b](#)). In the case of 3s and 3d two-photon decays, this enhances the emission of photons close to the Lyman  $\beta$  resonance (cf. Fig. 2). However, we find that the corrections due to stimulated two-photon emission are not important for the cosmological recombination problem.

### Appendix D: Small corrections due to the motion of the atom

To account for the motion of the atoms in the computations of the emission profile, one has to compute the following integral (see Sect. 9.2 in [Mihalas 1978](#))

$$\phi_{\text{m}}(\nu) = \int_{-\infty}^{\infty} \phi_{\text{r}}(\nu'(t)) e^{-t^2} dt, \quad (\text{D.1})$$

over the rest-frame emission profile,  $\phi_{\text{r}}(\nu)$ , which for a given frequency  $\nu$  due to the Doppler effect has to be evaluated at  $\nu'(t) = \nu[1 - \frac{\xi_0}{c} t]$ , where  $\xi_0 = c \sqrt{2kT/m_{\text{H}} c^2}$ . The exponential factor arises from the Maxwell-Boltzmann velocity distribution for the neutral hydrogen atoms.

For the Voigt profile, one normally uses the approximation  $\nu'(t) \approx \nu - \nu_{21} \frac{\xi_0}{c} t$ , so that the emission profile can be written in terms of the Voigt function

$$H(x_{\text{D}}, a) = \frac{a}{\pi} \int_{-\infty}^{\infty} \frac{e^{-t^2} dt}{(x_{\text{D}} - t)^2 + a^2}, \quad (\text{D.2})$$

for which simple approximation in terms of the Dawson-integral exist (see Sect. 9.2 in [Mihalas 1978](#)). Here  $a$  is the normal Voigt parameter, and  $x_{\text{D}}$  is the frequency distance from the line center in Doppler units of the Lyman  $\alpha$  resonance.

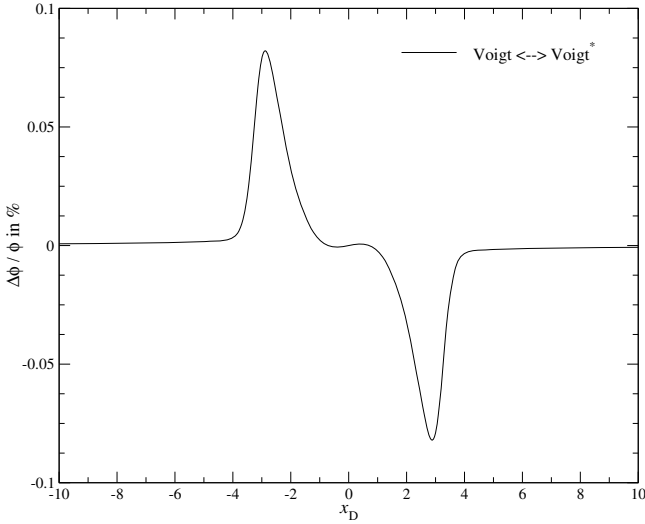


**Fig. D.1.** Small correction to the normal Voigt profile. We show the relative difference of the standard Voigt profile  $\phi \propto H(x_D, a)$  in comparison with the modified expression based on  $\tilde{H}(x_D, a)$  at  $z = 1100$ .

However, because of the steepness of the Lorentzian close to the line center this approximation leads to a small inaccuracy ( $\Delta\phi/\phi \sim 10^{-4} - 10^{-3}$ ), which is not necessary. To avoid this, one should simply replace  $x_D$  and  $a$  in the Voigt integral with  $\tilde{x}_D = x_D/[1 + x_D \frac{\Delta\nu_D}{\nu_{21}}]$  and  $\tilde{a} = a/[1 + x_D \frac{\Delta\nu_D}{\nu_{21}}]$ , and in addition multiply  $H$  with  $1/[1 + x_D \frac{\Delta\nu_D}{\nu_{21}}]$ , yielding

$$\tilde{H}(x_D, a) = \frac{H(\tilde{x}_D, \tilde{a})}{[1 + x_D \frac{\Delta\nu_D}{\nu_{21}}]} \quad (\text{D.3})$$

As one can see, the Voigt profile,  $\phi_V = \tilde{H}(x_D, a)/\sqrt{\pi}$ , then effectively behaves as

$$\begin{aligned} \phi_V(x_D) &\approx \frac{1}{\sqrt{\pi}} \frac{e^{-\tilde{x}_D^2}}{[1 + x_D \frac{\Delta\nu_D}{\nu_{21}}]} \\ &\approx \frac{1}{\sqrt{\pi}} e^{-x_D^2} \left[ 1 - x_D \frac{\Delta\nu_D}{\nu_{21}} (1 + 2x_D^2) \right] \end{aligned} \quad (\text{D.4})$$

close to the line center. At  $x_D \sim \pm 1$ , this implies a relative correction of  $\Delta\phi/\phi \sim \mp 3 \frac{\Delta\nu_D}{\nu_{21}} \approx \mp 6 \times 10^{-5}$  at  $z \sim 1100$ . However, at  $x_D \sim 3$  this correction is expected to reach the 0.1% level. In Fig. D.1, the frequency dependence of this correction is shown in more detail, confirming these statements. Note that as expected the behavior in distant wings ( $|x_D| \gg 1$ ) is not changed.

#### D.1. Two-photon profiles for moving atoms

As mentioned above, to include the motion of the atoms in the computation of the two-photon profiles one can in principle directly use the expression in Eq. (D.1). However, the computation of this integral is rather time-consuming, and in the very distant wings is also unnecessary<sup>17</sup>. Therefore, we use a different approach in which we utilize that the relative difference,  $\Delta\phi_{r,i}^{2\gamma}(\nu)/\phi_\Lambda(\nu)$ , between the rest frame two-photon profile,  $\phi_{r,i}^{2\gamma}(\nu)$ , and the normal Lorentzian,  $\phi_\Lambda(\nu)$ , varies very slowly

<sup>17</sup> There the motion of the atoms can be neglected since the two-photon profiles normally vary very slowly with frequency. Although this is not entirely true for the  $ns$  two-photon profiles close to the frequencies where  $\phi^{2\gamma}$  vanishes, one expects a negligible additional correction due to this approximation.

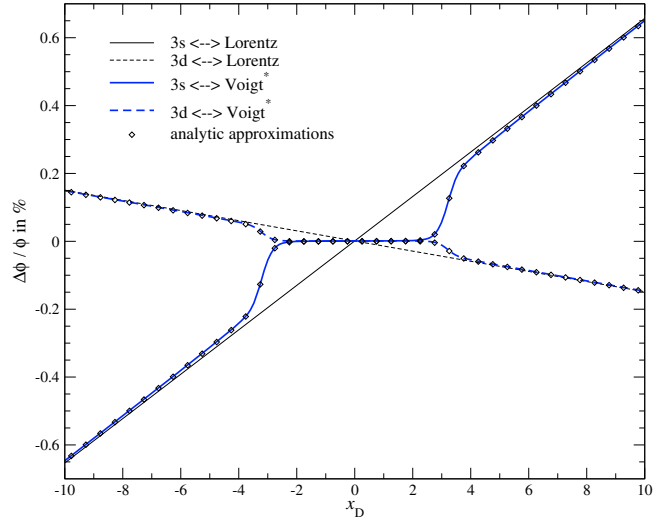


**Fig. D.2.** Relative difference of the 3s and 3d two-photon profiles with respect to the Lorentzian (thin line) and the Voigt profile (thick lines). In the first case the motion of the atoms was neglected, while for the comparison with the Voigt profile it was included. The boxes show the analytic approximation for the correction including the motion.

**Table D.1.** Parameters for the 3s and 3d two photon profiles around the line center. These were determined in the range  $-10 \lesssim x_D \lesssim 10$ . For explanation, see Appendix D.

	$\alpha_i$	$\beta_i$
3s	$3.73335 \times 10^{-6}$	$+6.5325 \times 10^{-4}$
3d	$7.45559 \times 10^{-7}$	$-1.5129 \times 10^{-4}$

with frequency, compared to  $\phi_\Lambda(\nu)$ . Therefore, to lowest order for moving atoms the two-photon profile will be given by  $\phi_{m,i}^{2\gamma}(x_D, a) \approx \phi_V(x_D, a) [1 + \Delta\phi_{r,i}^{2\gamma}(\nu)/\phi_\Lambda(\nu)]$ .

However, close to the line center this approximation due to the steepness of the Lorentzian again becomes inaccurate at the percent level. The lowest order correction can be computed approximating the rest-frame two-photon profiles close to the Lyman  $\alpha$  line center by

$$\phi_{r,i}^{2\gamma}(\nu) \approx \phi_\Lambda(\nu)[1 + \alpha_i + \beta_i x_D]. \quad (\text{D.5})$$

Here the coefficients  $\alpha_i$  and  $\beta_i$  for the 3s and 3d level are given in Table D.1.

Using the same method as described in Sect. 9.2 of Mihalas (1978), it can then be shown that for  $|x_D| \leq 1000$

$$\phi_{m,i}^{2\gamma}(x_D, a) \approx \phi_V(x_D, a) \left[ 1 + \frac{\Delta\phi_{r,i}^{2\gamma}(\nu)}{\phi_\Lambda(\nu)} + \frac{\beta_i}{2} \frac{\partial_{\tilde{x}_D} H(\tilde{x}_D, \tilde{a})}{\tilde{H}(\tilde{x}_D, \tilde{a})} \right]. \quad (\text{D.6})$$

Close to the line center, we use this expression for the two-photon profiles. However, far away from the Lyman  $\alpha$  resonance, we neglect the effect of the motion of the atoms, and simply use the rest-frame two-photon profiles.

However, we find that the correction in connection with the motion of the atom are unimportant to the cosmological recombination problem.

## References

- Chluba, J., & Sunyaev, R. A. 2006a, A&A, 458, L29  
 Chluba, J., & Sunyaev, R. A. 2006b, A&A, 446, 39  
 Chluba, J., & Sunyaev, R. A. 2007, A&A, 475, 109

- Chluba, J., & Sunyaev, R. A. 2008, *A&A*, 480, 629  
 Chluba, J., & Sunyaev, R. A. 2009a, *A&A*, 503, 345  
 Chluba, J., & Sunyaev, R. A. 2009b, *A&A*, 501, 29  
 Chluba, J., & Sunyaev, R. A. 2009c, *A&A*, 496, 619  
 Chluba, J., Rubiño-Martín, J. A., & Sunyaev, R. A. 2007, *MNRAS*, 374, 1310  
 Cresser, J. D., Tang, A. Z., Salamo, G. J., & Chan, F. T. 1986, *Phys. Rev. A*, 33, 1677  
 de Bernardis, F., Bean, R., Galli, S., et al. 2009, *Phys. Rev. D*, 79, 043503  
 Dubrovich, V. K., & Grachev, S. I. 2005, *Astron. Lett.*, 31, 359  
 Eisenstein, D. J. 2005, *New Astron. Rev.*, 49, 360  
 Eisenstein, D. J., Zehavi, I., Hogg, D. W., et al. 2005, *ApJ*, 633, 560  
 Fendt, W. A., Chluba, J., Rubiño-Martín, J. A., & Wandelt, B. D. 2009, *ApJS*, 181, 627  
 Göppert-Mayer 1931, *Annalen der Physik*, 9, 273  
 Grachev, S. I., & Dubrovich, V. K. 2008, *Astron. Lett.*, 34, 439  
 Hirata, C. M. 2008, *Phys. Rev. D*, 78, 023001  
 Hu, W., Scott, D., Sugiyama, N., & White, M. 1995, *Phys. Rev. D*, 52, 5498  
 Hütsi, G. 2006, *A&A*, 449, 891  
 Jentschura, U. D. 2009, *Phys. Rev. A*, 79, 022510  
 Jones, B. J. T., & Wyse, R. F. G. 1985, *A&A*, 149, 144  
 Karshenboim, S. G., & Ivanov, V. G. 2008, *Astron. Lett.*, 34, 289  
 Kholupenko, E. E., & Ivanchik, A. V. 2006, *Astron. Lett.*, 32, 795  
 Labzowsky, L., Solovveyev, D., & Plunien, G. 2009, *Phys. Rev. A*, 80, 062514  
 Mihalas, D. 1978, *Stellar atmospheres/2nd edn.* (San Francisco: W. H. Freeman and Co.), 650  
 Peebles, P. J. E. 1968, *ApJ*, 153, 1  
 Peebles, P. J. E., Seager, S., & Hu, W. 2000, *ApJ*, 539, L1  
 Rubiño-Martín, J. A., Chluba, J., & Sunyaev, R. A. 2006, *MNRAS*, 371, 1939  
 Rubiño-Martín, J. A., Chluba, J., & Sunyaev, R. A. 2008, *A&A*, 485, 377  
 Seager, S., Sasselov, D. D., & Scott, D. 1999, *ApJ*, 523, L1  
 Seager, S., Sasselov, D. D., & Scott, D. 2000, *ApJS*, 128, 407  
 Seljak, U., Sugiyama, N., White, M., & Zaldarriaga, M. 2003, *Phys. Rev. D*, 68, 083507  
 Silk, J. 1968, *ApJ*, 151, 459  
 Sunyaev, R. A., & Chluba, J. 2007, *Nuovo Cimento B Serie*, 122, 919  
 Sunyaev, R. A., & Chluba, J. 2008, in *Frontiers of Astrophysics: A Celebration of NRAO's 50th Anniversary*, ed. A. H. Bridle, J. J. Condon, & G. C. Hunt, ASP Conf. Ser., 395, 35  
 Sunyaev, R. A., & Zeldovich, Y. B. 1970, *Ap&SS*, 7, 3  
 Switzer, E. R., & Hirata, C. M. 2008, *Phys. Rev. D*, 77, 083006  
 Wong, W. Y., & Scott, D. 2007, *MNRAS*, 375, 1441  
 Wong, W. Y., Moss, A., & Scott, D. 2008, *MNRAS*, 386, 1023  
 Zeldovich, Y. B., Kurt, V. G., & Syunyaev, R. A. 1968, *Zhurnal Eksperimentalnoi i Teoreticheskoi Fiziki*, 55, 278